University of California

Los Angeles

The Search for Dark Matter in Xenon100 using a Two-Dimensional Profile Likelihood Analysis

A dissertation submitted in partial satisfaction

of the requirements for the degree

Doctor of Philosophy in Physics

by

Kevin Joseph Lung

2013

ABSTRACT OF THE DISSERTATION

The Search for Dark Matter in XENON100 using a Two-Dimensional Profile Likelihood Analysis

by

Kevin Joseph Lung

Doctor of Philosophy in Physics

University of California, Los Angeles, 2013

Professor Katsushi Arisaka, Chair

Direct dark matter detectors are currently probing the favored supersymmetric theoretical phase space for weakly interacting massive particles (WIMPs) as part of a larger electroweak sector particle search. The XENON100 detector has recently improved upon their world-best upper limits on WIMP-nucleon scattering cross sections from 2011 with new results presented in 2012, which have further ruled out much of the predicted regions for dark matter. In the low mass regime, the results shown so far have been conservative in addressing the claims of a WIMP detection by CoGeNT, DAMA and CRESSTII.

This thesis discusses a different approach to analyzing the XENON100 data with a profile likelihood statistical method using the ionization channel to improve both energy reconstruction and energy resolution and probe the low WIMP mass region. A Monte Carlo simulation using a combination of detector geometry and underlying statistical features of signal production has been developed to determine the ionization yield, which has only a few direct measurements, and to model WIMP interactions as input to the statistical technique. The resulting profile likelihood analysis, which includes systematic uncertainties in the energy scales and background and signal models, has been able to improve the current upper limits by a factor of 10 in the low mass region (6-10 GeV/c^2) and about a factor of 2 up to 50 GeV/c^2. The discovery potential of the dataset is also studied, which has produced a 2.3σ significance for a 7.5 GeV/c^2 particle at a cross section of $\sigma_{\chi-N} = 1.8 \times 10^{-43}$ cm^2 with a 95% confidence interval of $[1.74 \times 10^{-44}, 7.76 \times 10^{-43}]$ cm^2.

The dissertation of Kevin Joseph Lung is approved.

Matthew A. Malkan
David Saltzberg
M. C. Frank Chang
Katsushi Arisaka, Committee Chair

University of California, Los Angeles
2013

To my parents

Table of Contents

List of Figures

List of Tables

Acknowledgments

I would like to express my deepest gratitude to all those who made this work possible. I would like to first thank my advisor Professor Katsushi Arisaka, whose enthusiasm and expertise have guided me over the past four years. His love of science and thirst for the unknown have had a profound impact throughout my graduate student career. I would also like to thank Dr. Hanguo Wang for his presence as a stabilizing figure providing me with valuable perspective on both science and the real world. And to my committee, professors M. C. Frank Chang, David Saltzberg, and Matthew Malkan, my thanks go to you for taking the time to read this document.

The Xenon100 collaboration has provided an engaging environment for dark matter research and I am thankful for all their support. From my fellow grad students to the PIs, all have been great collaborators and friends in such an intense field at the frontiers of science. I would especially like to thank Professor Elena Aprile for this opportunity as a member of the leading experiment in the dark matter field.

I would like to give sincere thanks to everyone that has been associated with the UCLA dark matter group in the past few years. Paolo Beltrame, Ethan Brown, Alden Fan, Chamkaur Ghag, Alexey Lyashenko, Yixiong Meng, Emilija Pantic, Paul Scovell, Artin Teymourian have all provided day to day relief and helpful advice when I needed it the most.

Finally I would like to thank my family and friends who have been there with me throughout my time in graduate school. I never get to say this enough, but I love you all. Your words and thoughts have given me the confidence and inspiration necessary to complete such a daunting task. I am glad you are all still

in my life. And to Miss Melody Chen, I'm sure that whatever happens, it will be great.

Vita

2008	B.S. (Engineering Physics), University of California, Berkeley.
2008–2009	Teaching Assistant Physics and Astronomy Department, UCLA.
2008–present	Research Assistant Physics and Astronomy Department, UCLA.

Publications

Xenon100 Collaboration (E. Aprile, *et al.*) *Limits on spin-dependent WIMP-nucleon cross sections from 225 live days of XENON100 data.* (2013), arXiv:1301.6620.

E. Aprile, *et al.* *The distributed Slow Control System of the XENON100 Experiment.* Journal of Instrumentation 7 (2012) T12001.

K. Arisaka, *et al.* *Expected Sensitivity to Galactic/Solar Axions and Bosonic Super-WIMPs based on the Axio-electric Effect in Liquid Xenon Dark Matter Detectors.* (2012), arXiv:1209.3810.

K. Arisaka, *et al.* *A New Analysis Method for WIMP searches with Dual-Phase Liquid Xe TPCs.* Astroparticle Physics 37 (2012) 1-88.

XENON100 Collaboration (E. Aprile, *et al.*) *Dark Matter Results from 225 Live Days of XENON100 Data.* Physical Review Letters 109 (2012) 181301.

XENON100 Collaboration (E. Aprile, *et al.*) *Analysis of the XENON100 Dark Matter Search Data.* (2012), arXiv:1207.3458.

DarkSide Collaboration (D. Akimov, *et al.*) *Light Yield in DarkSide-10: a Prototype Two-phase Liquid Argon TPC for Dark Matter Searches.* Fermilab Publications 12-619-E (2012).

K. Lung, *et al.* *Characterization of the Hamamatsu R11410-10 3-Inch Photomultiplier Tube for Liquid Xenon Dark Matter Direct Detection Experiments.* Nuclear Instruments and Methods A696 (2012) 32-39.

K. Arisaka, *et al.* *Studies of a three-stage dark matter and neutrino observatory based on multi-ton combinations of liquid xenon and liquid argon detectors.* Astroparticle Physics 36 (2012) 93-122.

XENON100 Collaboration (E. Aprile, *et al.*) *Implications on Inelastic Dark Matter from 100 Live Days of XENON100 Data.* (2011), Physical Review D85 (2011) 061101.

XENON100 Collaboration (E. Aprile, *et al.*) *Dark Matter Results from 100 Live Days of XENON100 Data.* Physical Review Letters 107 (2011) 131302.

A. Teymourian, *et al.* *Characterization of the QUartz Photon Intensifying De-*

tector (QUPID) for Noble Liquid Detectors. Nuclear Instruments and Methods A654 (2011) 184-195.

XENON100 Collaboration (E. Aprile, *et al.*) *Study of the electromagnetic background in the XENON100 experiment.* Physical Review D83 (2011) 082001, Erratum-ibid. D85 (2012) 029904.

K. Arisaka, *et al. XAX: a multi-ton, multi-target detection system for dark matter, double beta decay, and pp solar neutrinos.* Astroparticle Physics 31 (2009) 63-74.

CHAPTER 1

Dark Matter

The exact nature of the composition of the current universe is mostly unknown. Cosmological observations over the past century have suggested that the visible matter we traditionally observe accounts for only about 4.8% of the universe's total energy density while the rest is thought to be comprised of two so-far undetected components. The first is a dark matter component that interacts only ultra-weakly or gravitationally with normal matter and the second, of which we know far less, is a uniform energy density associated with the vacuum called dark energy, which is responsible for the accelerating expansion of the universe. In the Standard Model of Big Bang Cosmology (ΛCDM - cosmological constant and cold dark matter [1]), the dark matter is understood to be a non-relativistic weakly interacting particle or sets of particles responsible for the accelerated transition of the universe from radiation dominated to matter dominated allowing for earlier structure formation of galaxies and galaxy clusters [2]. This theory in conjunction with cosmological observations have demonstrated that dark matter, as opposed to traditional luminous baryonic matter, makes up over 80% of the total matter content of the universe and roughly 26% of its total energy density [3] with the remaining 69% contained in dark energy.

The evolution of the universe is well modeled by standard cosmological theory, which incorporates geometry, symmetries, and matter and energy density. The observed isotropy and homogeneity of the universe [4] is described by a metric of space-time

$$ds^2 = -c^2 \mathrm{d}t^2 + a(t)^2 \left(\frac{\mathrm{d}r^2}{1-kr^2} + r^2 \mathrm{d}\Omega^2 \right) \tag{1.1}$$

where the curvature constant k defines the spatial geometry (where k can take on the values -1, 0, and +1) and the scaling factor $a(t)$ that relates proper distances in terms of comoving coordinates. The equations of motion for the universe can then be derived from Einstein's field equation

$$R_{\mu\nu} - \frac{1}{2} g_{\mu\nu} R = -\frac{8\pi G_N}{c^4} T_{\mu\nu} + \Lambda g_{\mu\nu} \, . \tag{1.2}$$

where G_N is Newton's gravitational constant and $g_{\mu\nu}$ is the spacetime metric (an example is given by equation 1.1). The logic behind this equation is illuminating: the geometrical nature of the universe (the Ricci tensor, $R_{\mu\nu}$, and scalar, R on the left hand side) is governed by the energy content, the energy-momentum tensor $T_{\mu\nu}$, and the cosmological constant Λ, a vacuum energy associated with space-time itself. One of the solutions to these equations, using the aforementioned metric, is the Friedmann Equation,

$$\left(\frac{\dot{a}}{a} \right) + \frac{k}{a^2} = \frac{8\pi G_N}{3} \rho_{tot} \tag{1.3}$$

where ρ_{tot} is the total average energy density of the universe and G_N is Newton's gravitational constant. This equation can be rewritten in terms of total normalized energy density, $\Omega_{tot} = \sum \Omega_i = \sum \rho_i / \rho_c$ for different components of the universe (matter, radiation, or vacuum energy), where $\rho_c \equiv 3H^2/8\pi G_N$, a critical density (density of a flat universe) and the Hubble parameter $H(t) = \dot{a(t)}/a(t)$ characterizing the expansion rate of the universe.

$$\Omega_{tot} - 1 = \frac{k}{H^2 a^2} \tag{1.4}$$

From this form of the Friedmann equation, it is seen that if $\Omega_{tot} < 1$, $k = -1$ resulting in an open universe, if $\Omega_{tot} = 1$, $k = 0$, which represents a flat universe, and finally if $\Omega_{tot} > 1$, $k = 1$, a closed universe [5].

The content of the universe is then represented by the Ω_i, which is divided between major contributions from normal baryonic matter (Ω_b), dark matter (Ω_c), and dark energy (Ω_Λ). The evolution of each of the components has been mapped out based on its redshift dependence and theoretical equation of state following from a derivation in Bergstrom [6]. The latest results from the PLANCK satellite [3] with baryon acoustic oscillation observations and Hubble constant calculations have found that the current composition of the universe is most likely $\Omega_\Lambda = 0.692 \pm 0.010$, $\Omega_c = 0.258 \pm 0.004$, and $\Omega_b = 0.04816 \pm 0.0005$ representing a flat universe with accelerating expansion.

The focus of this work is on the search for dark matter, Ω_c, of the universe which is well founded in cosmology. Additionally, dark matter may be directly linked to a well-motivated particle candidate in physics beyond the Standard Model, where the stable lightest neutralino from supersymmetry arises naturally out of the theory and may be detected through weak scattering off Standard Model particles. This connection between cosmology and particle physics makes dark matter particularly fascinating.

1.1 Cosmological Observations

The first evidence for dark matter follows from inconsistencies between the predicted and observed motion of celestial objects dating back to observations in the early 1930's with Fritz Zwicky and Jan Oort. Their measurements of galaxy and galaxy cluster velocities point to the presence of a nonluminous weakly interacting matter responsible for large scale structure formation. More than 70 years of observation later, from small scale galaxies to cosmic microwave radiation, the composition of this matter is still unknown.

1.1.1 Galactic Observations

Almost forty years after Oort found an unexpected distribution of stars in the Milky Way galaxy [7], some of the most compelling evidence for the existence of dark matter was observed from the velocity rotation curves of disk galaxies. Vera Rubin's measurements in the late 1960's through the 1970's revealed a discrepancy between the velocity expected from the luminous disk compared to the velocity observed [8]. This led to the conclusion that galaxies must have considerable mass beyond the optically-visible matter disk. Figure 1.1 shows a typical rotation curve with the flat observed velocity trend to higher radii. This trend can be attributed to the sum of a disk component from luminous matter and a halo component of dark matter [9].

From Newton's law of gravitation, galactic velocities are expected to follow from

$$v(r) = \sqrt{\frac{G_N M(r)}{r}} \tag{1.5}$$

where $M(r) \equiv 4\pi \int \rho(r) r^2 \mathrm{d}r$ denotes the mass distribution with the radial dependent density $\rho(r)$. For only a luminous disc, the velocity is projected to fall such that $v(r) \propto 1/\sqrt{r}$ beyond its bounds. However, the observation of a flat curve requires $\rho(r) \propto 1/r^2$ suggesting the presence of an unseen dark matter halo.

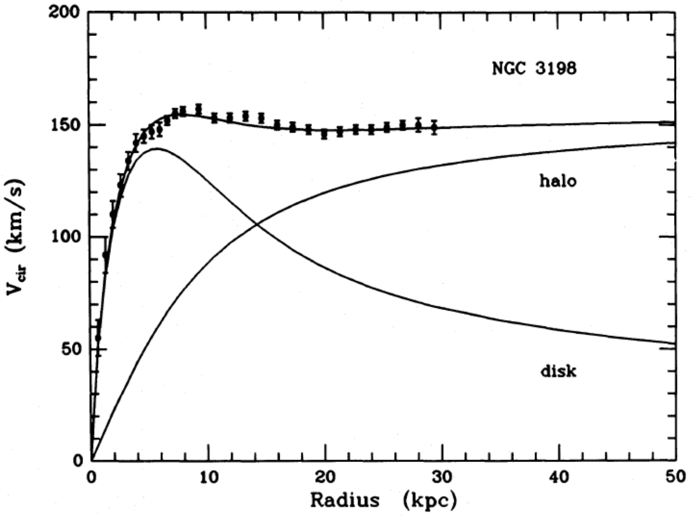

Figure 1.1: The galactic rotation curve of NGC 3198. The curve is fit by the disk-halo model with the largest possible mass for the disk and a hollow core for the halo. Data is only taken up to 30 kpc, but the model is extrapolated out to further radii as there are no hints of decreasing velocity. Taken from [9].

The assumption of the density distribution of a spherical halo with an isothermal sphere [10]

$$\rho_{halo}(r) = \rho_0 \left[1 + \left(\frac{r}{r_c} \right)^2 \right]^{-1} \tag{1.6}$$

where r_c is the radius of the halo core, results in a flat rotation curve. These observations infer the existence of unseen matter, but the lack of precision in measuring the mass contained in the halo using these techniques has led some theorists to favor other explanations, such as a modified theory of gravity (section 1.2).

1.1.2 Galaxy Cluster Observations

The other of the very earliest mentions of the consequences of dark matter came from Fritz Zwicky, whose inference of the mass-to-luminosity ratio of the Coma cluster was more than two orders of magnitude larger than expected [11, 12]. From examining the velocities of galaxies within the cluster, Zwicky was able to determine that the amount of mass present in the cluster far exceeded the amount visible.

To measure the mass of the cluster, Zwicky employed the virial theorem to relate the gravitational potential to the kinetic energy contained

$$-\overline{E_p} = 2\overline{K_T} \tag{1.7}$$

where the bar indicates time-averaging, $E_p = -\sum\limits_{\sigma,\nu}^{\sigma<\nu} \frac{\Gamma M_\sigma M_\nu}{r_{\sigma\nu}}$, and $2K_T = \sum\limits_{\sigma} M_\sigma \overline{v_\sigma^2}$, with v_σ the velocity of the mass M_σ and Γ, the gravitational constant (G_N).

Under the assumption of a uniform distribution of galaxies in a sphere of radius R, the potential energy may be rewritten as

$$E_p = \frac{-3\Gamma\mathcal{M}^2}{5R} \tag{1.8}$$

with the total mass, $\mathcal{M}$. The total kinetic energy can also be written in the form

$$K_T = \sum_\sigma M_\sigma \overline{v_\sigma^2} = \mathcal{M}\overline{\overline{v^2}} \tag{1.9}$$

where the double-bar denotes averages over both time and mass. The virial theorem (equation 1.7) and the potential and kinetic energies (equations 1.8 and 1.9) then lead to an expression for the total mass

$$\mathcal{M} = \frac{5R\overline{\overline{v^2}}}{3\Gamma}. \tag{1.10}$$

A slightly more conservative assumption about the distribution of galaxies within the cluster lends itself to a very simple inequality

$$\mathcal{M} > \frac{3R\overline{\overline{v_s^2}}}{5\Gamma}. \tag{1.11}$$

where v_s is the spherically symmetric velocity. Measurements of the average of the square velocities have found $\overline{\overline{v_s^2}} = 5 \times 10^{15}\,\mathrm{cm}^2\,\mathrm{sec}^{-2}$ such that average mass of a nebula is $\overline{M} > 9 \times 10^{43}\,g = 4.5 \times 10^{10} M_\odot$. The average luminosity of a nebula is approximately 8.5×10^7 suns, leading to a mass to light ratio on the order of 500. Typical ratios for local stellar systems are about 3, or two orders of magnitude less than that observed in the Coma cluster.

Many other methods now exist to measure the mass of clusters [13] supporting this notion of excess mass. The evidence for dark matter at such large scales has reinforced the existence of a new matter over other modified gravity theories to explain these observations.

1.1.3 Weak Gravitational Lensing and the Bullet Cluster

One of the other important methods to infer the mass distribution of galaxy clusters is weak gravitational lensing [14]. A map of the gravitational potential of the cluster can be reconstructed by measuring the distortion of background galaxy images due to gravitional deflection of light. The image will appear stretched along a direction perpendicular to that of the center of mass of the distribution betwen the observer and background galaxy [15].

This technique has been applied to the interacting cluster 1E 0657–558, the

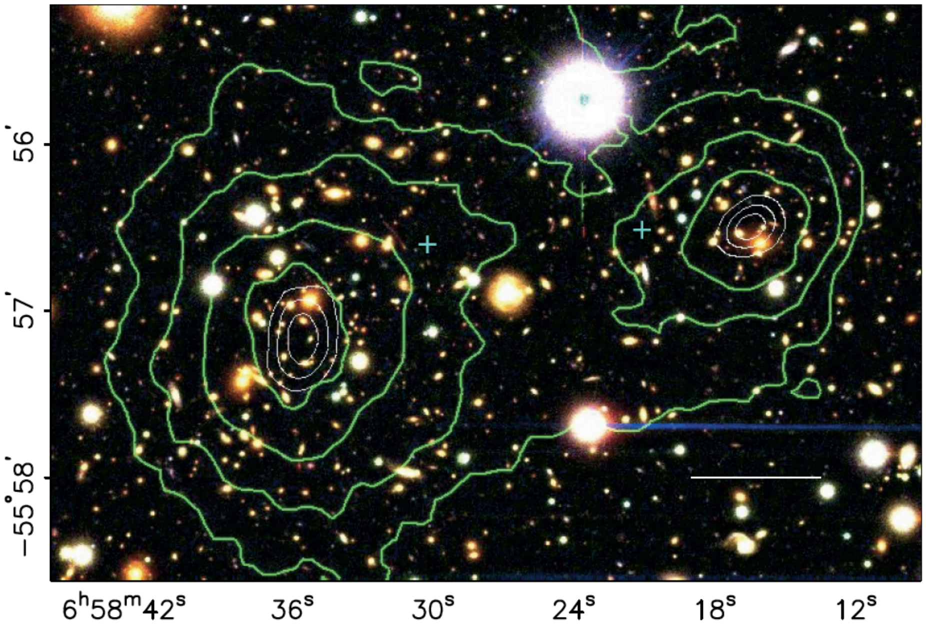

Figure 1.2: Interacting galaxy cluster 1E0657–558 (the Bullet Cluster) from Magellan images. Overplotted in green contours are the weak gravitational lensing reconstructions. Two peaks in the lensing map are evident from the dark matter distributions of the individual clusters. Taken from [16].

Bullet Cluster, in which a smaller subcluster has undergone infall and pass-through of the main cluster. In the collision, it is believed most of the cluster behaves in a collision-less manner (roughly 80%-90%), while the X-ray-emitting plasma (5%-15%) undergoes ram pressure causing the majority of the mass to become decoupled from the plasma [16].

The result of weak lensing, figure 1.2, shows the gravitational potential map from four optical imaging sets from the Wide Field Imager (WFI) [17], the Inamori Magellan Areal Camera and Spectrograph (IMACS) [18], and the Hubble Space Telescope (HST - NASA). Two distinct distributions are present, for the main cluster to the eastern side (left) and the subcluster on the western side

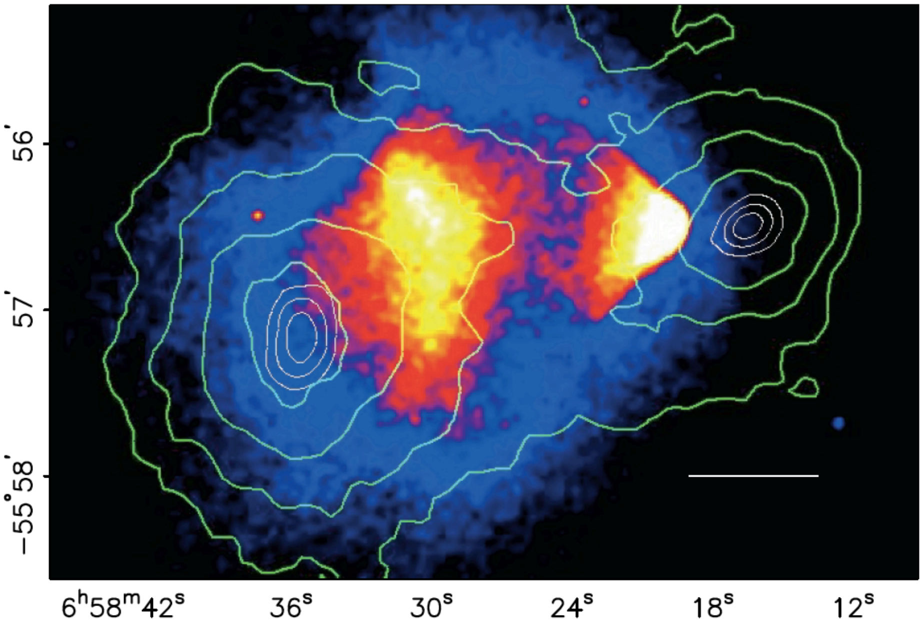

Figure 1.3: Interacting galaxy cluster 1E0657–558 (the Bullet Cluster) from the *Chandra* X-ray telescope. Overplotted in green contours are the weak gravitational lensing reconstructions. The X-ray peak for the main cluster is offset from the weak lensing peak at a 3.4σ significance. Taken from [16].

(right). In relation to the brightest cluster galaxy of each, the larger cluster is detected at 12σ and the subcluster at 8σ significance.

Data is also available from the *Chandra* X-ray telescope [19], which detects emission from the X-ray plasma, the dominant baryonic component of the clusters shown in figure 1.3. Again, two distributions are observed, but in much closer proximity. The peaks of the weak lensing are observed at about 8σ away from the peaks of the respective plasma clouds.

The phenomenon observed in this merger of two galaxy clusters provides convincing proof for the hypothesis of a large amount of dark matter in large scale structures. The lensing map and X-ray measurements demonstrate the collision-less properties of the majority of the clusters, while the intracluster baryonic plasma has cooled and slowed down through ram pressure. This suggests that a modification to the gravitational laws (MOND, to be detailed later) cannot explain these observations.

1.1.4 Cosmic Microwave Background

The final, and perhaps most important, point to be discussed is the observation and subsequent measurements of the cosmic microwave background (CMB), leftover thermal radiation shortly after the big bang when photons decoupled from matter. Alpher and Herman first discussed this radiation in 1948, which they estimated to be around 5 K [20]. In 1965, Penzias and Wilson, at Bell Telephone Laboratories, found an ambient excess temperature reading of 3.5K from their radio instruments [21], which they proved to be due to the cosmic microwave background in a Nobel Prize winning discovery. Initially thought to be extremely uniform, many satellites over the next 30 years began to measure the blackbody spectrum much more precisely and found anisotropies on the order of 10^{-4} or 10^{-5} leading to the Nobel Prize winning achievement in Physics in 2006 for precision measurement of the CMB radiation from the COsmic Background Explorer (COBE) [22]. A more recent measurement of the CMB, performed by the PLANCK mission [23], can be seen in figure 1.4.

Following the COBE measurement, several other experiments, including the Mobile Anisotropy Telescope (MAT/TOCO) [24], BOOMERANG [25] (balloon observations), Wilkinson Microwave Anisotropy Probe (WMAP) [26], and PLANCK began to measure the anisotropies on smaller angular scales to improve the understanding of acoustic oscillations from the early universe. These oscillations, originating from the photon-baryon plasma in the early universe and the opposi-

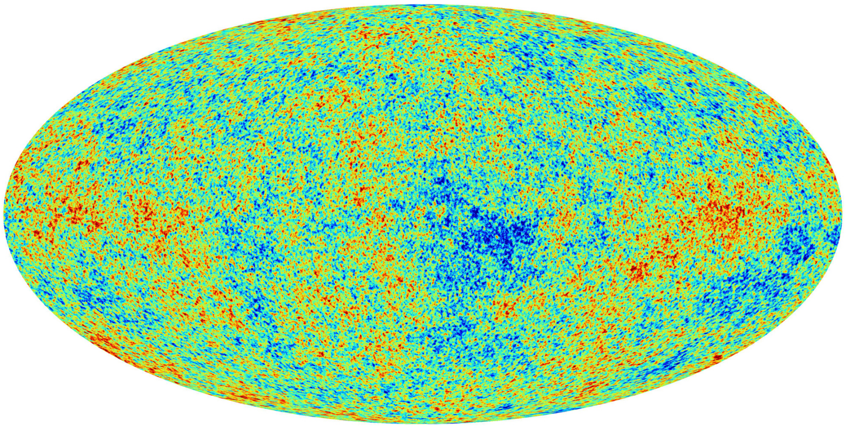

Figure 1.4: A full sky survey of the cosmic microwave background radiation from the PLANCK mission. Anisotropies present are on the order of 10^{-4} or 10^{-5} with a 50 μK range from cold (blue) to hot (red). Figure taken from ESA (http://spaceinimages.esa.int/Images/2013/03/Planck_CMB).

tion of radiation pressure from photons to gravitational potential of matter, leave evidence of the composition and history of the universe [27].

In particular, analysis of the PLANCK satellite data of the first few oscillation peaks of the angular power spectrum (figure 1.5) has supported Big Bang Nucleosynthesis, shown that the universe is spatially flat to within 1%, and concluded the universe must contain a dark matter component that is nonbaryonic and must be at most weakly interacting with radiation [28, 29]. The parameters of the ΛCDM model best-fit in figure 1.5 for the matter components obtained from both the second and third acoustic peaks [29] are $\Omega_b h^2 = 0.02266 \pm 0.00043$ and $\Omega_c h^2 = 0.1157 \pm 0.0023$, for a baryonic matter component of 4.5% and a dark matter component of 24%.

The multitude of observations have provided a strong evidence for the existence of dark matter, but dedicated experiments have been unable to directly or

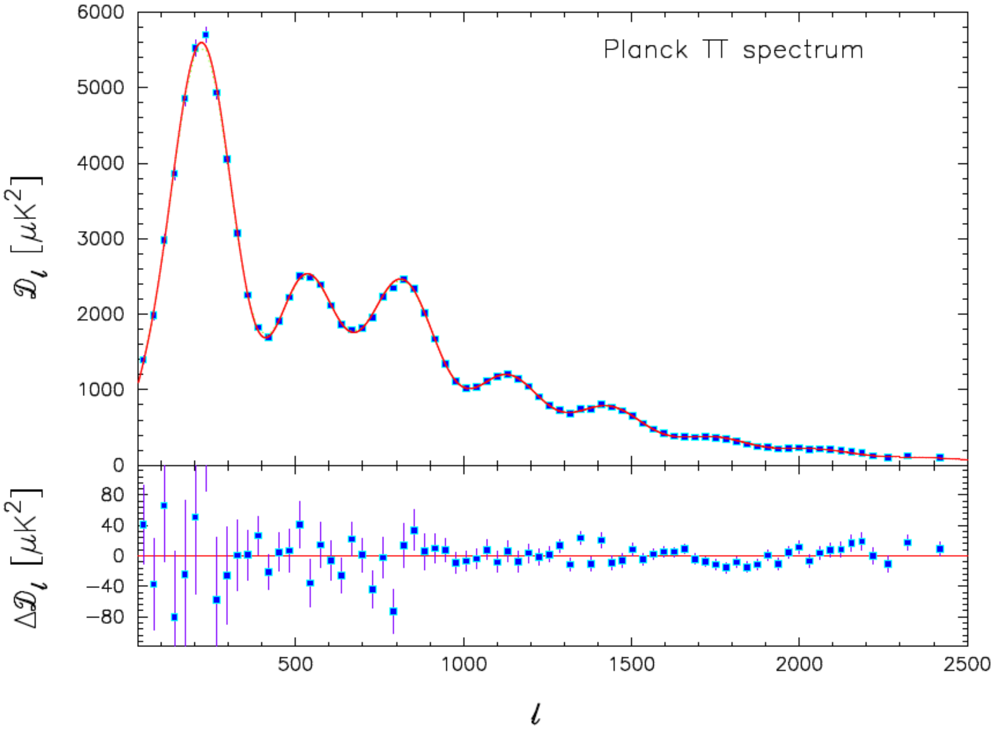

Figure 1.5: Angular power spectrum of the CMB temperature expanded in spherical harmonics from the PLANCK mission. Overplotted is a curve from the ΛCDM model best fit with residuals in the bottom panel. Figure taken from [3].

indirectly observe it, or produce it in accelerators. The challenges to observation are presented in section 1.4.1.

1.2 MOND

An alternative explanation for some of these observations, in particular discrepancies between luminous matter and the dynamics of a galaxy or cluster, is a MOdified Newtonian Dynamics (MOND) theory suggested by Milgrom [30, 31] in which traditional Newtonian gravitational laws are corrected on galactic and larger scales. The foundation for MOND is based upon the observations of flat galactic rotation curves and the luminous matter to rotation velocity relation, $M \propto v^{\alpha}$, where α is approximately 4. The modifications to Newton's gravity occur at only low accelerations such that the full theory resides upon an acceleration scale instead of a length scale as observations do not support any length scale dependences.

The resulting MOND theory will then have a force law given by

$$\boldsymbol{F} = m\boldsymbol{a}\mu \tag{1.12}$$

where $\mu = \mu(a/a_0)$, such that at low accelerations, $a \approx 10^{-8}$ cm/s^2, the effective gravitational acceleration becomes $\sqrt{G_n a_0}$, where G_n is the typical Newtonian gravitational acceleration, a_0 is a new physical constant, and μ is the acceleration scale. This results in flat rotation curves with a mass-luminosity dependence of $M \propto v^4$. The upshots of such a modified theory are a critical surface density, or a mean surface brightness, as the upper limit for rotationally supported systems, which serves as the crossover regime for Newtonian-MOND dynamics, isothermal pressure-supported systems with finite mass, and an external field effect in the neighborhood of the system that violates the strong form of the equivalence principle.

This modified gravity theory has been found to describe the rotational velocity curves of both high and low surface brightness galaxies with only a single free parameter, the mass-to-luminosity ratio while reproducing the velocity dispersion versus size for pressure-supported isothermal systems of a variety of sizes and environments for very low internal accelerations. The difficulties expected of dark matter to demonstrate these observations lies in the multitude of different galactic types and physical systems, which cannot be explained universally by a Newtonian dark matter theory.

The theoretical basis for MOND is lacking in spite of its observational triumphs due to its failure to adhere to a more familiar, logical mathematical formulation. More importantly, MOND fails to explain the phenomena present in the Bullet Cluster (section 1.1.3), which originate from different centers of gravity from the luminous center of mass [16], the acoustic oscillation peaks in the CMB, and cosmological large scale structure formation. In attempts to remedy these discrepancies, a theory called MOND+neutrinos has been developed, but will not be further discussed here [32].

1.3 Dark Matter Particle Candidates

The CMB has provided evidence for dark matter particles unlike traditional baryonic matter of protons and neutrons in the Standard Model that are instead weakly interacting with normal matter and radiation while comprising approximately 22% of the universe. Additionally, the predictive successes of the ΛCDM theory has led to the understanding that dark matter is cold, or non-relativistic at the time of decoupling, which rules out Standard Model lepton candidates, such as the neutrino.

In briefly reviewing the history of the universe, it is evident that a stable particle in the early universe (possibly dark matter) could have a considerable cosmological abundance today [33]. While in thermal equilibrium in the early universe, maintained through the annihilation and production to and from lighter particles, the expansion of the universe could have caused these particles to fall out of thermal equilibrium leaving behind a relic cosmological abundance. Attributing this leftover density to dark matter suggests a composition of weakly interacting massive particles (WIMPs) or axions.

Beyond the Standard Model are several theories, which contain possible dark matter candidates of interest. The well-motivated candidates that will be overviewed are the axion, and two WIMP particles, the supersymmetric neutralino, and the extra dimension Kaluza-Klein particle. Additionally, there are other possible dark matter candidates, like the superheavy wimpzilla (which has been ruled out) or the superpartner of the graviton, the gravitino (undetectable by current experiments).

1.3.1 Axions

A proposed solution by Peccei and Quinn to the CP violation problem of QCD [34], axions, as an extension to the Standard Model, also fit within the framework of a cold dark matter particle candidate as they are nonbaryonic and weakly interacting with regular matter and radiation and could be the dominant matter component of spiral galaxies like our own. These axions originate from oscillations of a coherent scalar field due to a misalignment of θ, the axion degree of freedom, which is initially unknown at the Peccei Quinn symmetry breaking scale (temperature near the coupling strength of the Standard Model to the axion, f_a). As the universe cooled after the QCD phase transition, the axion generates a mass on the order of 10^{-5} to 10^{-2} eV from instanton effects, which gives a mass density of $\rho = 5 \times 10^{-25}$ g cm^{-3} [35] or ~ 0.3 GeV cm^{-3} in the galactic halo, the expected dark matter density in our galaxy.

Experimental searches for axions consist of microwave cavities with strong magnetic fields as in ADMX (Axion Dark Matter eXperiment) [36], which look for monochromatic signatures from the interactions of halo dark matter with ground-based detectors. The application of a high magnetic field with a superconducting solenoid to a high-Q helium-cooled cavity searches for a resonant frequency characterized by the axion mass. The difficulty of this axion search stems from the large range of possible masses (or frequencies) needs to be scanned.

1.3.2 Supersymmetric Neutralino

Before going into details about the neutralino, it is useful to briefly overview Supersymmetry (SUSY) [37, 38], an extension to the Standard Model (SM) of particle physics. The SM consists of fermions, constituents of matter, and bosons, the force carriers; supersymmetry doubles the number of particles with a superparter for each SM particle of the opposite type, i.e. fermions for bosons and bosons for fermions (figure 1.6). This doubling of particles allows for the hierarchy problem to be solved, the merging of the electroweak and QCD sectors at the Grand Unified Theory (GUT) energy scale, and is a natural part of superstring or supergravity theories in which general relativity is to be combined with quantum mechanics.

Within a branch of these theories, called Minimal Supersymmetric Standard Model (MSSM) theories, exists a new quantum number called R-parity to suppress the possibilities for proton decay. The conservation of R-parity, SM particles are +1 and superparticles (sparticles) are -1, requires that the decay of all sparticles results in an odd number of sparticles, such that the lightest supersymmetric particle (LSP) is stable and can only decay via pair annihilation. One of the candidates for the LSP is a linear combination of the higgsino, bino, and wino, which provides a neutral, stable and massive (on the order of 50 GeV to 1 TeV) particle called the neutralino, the lightest of which is a well-motivated candidate for the dark matter of universe.

Due to its large mass and weakly interacting nature, the neutralino may provide the necessary thermal relic density required of dark matter. From the Boltz-

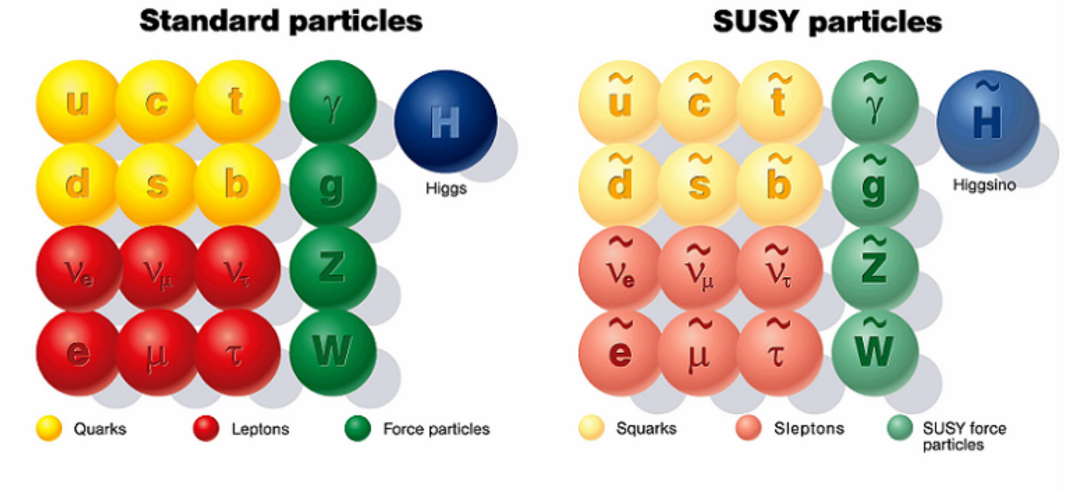

Figure 1.6: Diagram of the Standard Model on the left and the Supersymmetric extension on the right. The neutralino, the lightest supersymmetric particle, is composed of a linear combination of the higgsino, bino, and wino.

mann equation, the time evolution of the number density of dark matter particles, n_χ, is

$$\frac{dn_\chi}{dt} + 3Hn_\chi = -\langle \sigma_A v \rangle [(n_\chi)^2 - (n_\chi^{eq})^2] \tag{1.13}$$

where H is the Hubble parameter defined previously, accounting for the expansion of the universe, $\langle \sigma_A v \rangle$ is the thermally averaged total cross section for the annihilation of dark matter particles multiplied by the velocities, and right hand side denotes the creation and annihilation of particles. An order of magnitude calculation for the resulting relic density can be written in terms of the annihilation cross section through solving the Boltzmann equation under the assumption of energy independence for the cross section

$$\Omega_\chi h^2 = m_\chi n_\chi / \rho_c \simeq (3 \times 10^{-27} \mathrm{cm}^3\, \mathrm{s}^{-1} / \langle \sigma_A v \rangle). \tag{1.14}$$

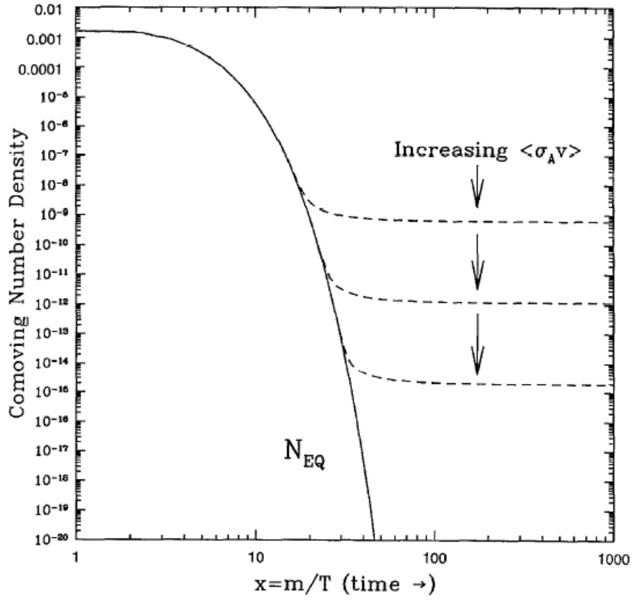

Figure 1.7: Thermal relic abundance for WIMP dark matter for different annihilation cross sections. Taken from [39].

This is independent of the WIMP mass to first order and is inversely proportional to the annihilation cross section. Figure 1.7 shows the results of numerical calculations of the Boltzmann equation as a function of m_χ/T, where an increased annihilation cross section results in a smaller relic abundance. For a new particle with weak-scale interactions, $\langle\sigma_A v\rangle \sim 10^{-25}\,\mathrm{cm}^3\,\mathrm{s}^{-1}$, which in conjunction with equation 1.14, gives a density very close to that expected from cosmology ($\Omega \sim 1$). The existence of such a coincidence suggests that the discovery of a stable particle near the electroweak energy scale could be attributable to WIMP dark matter. Currently, this provides the most well motivated dark matter candidate and is the focus of many experiments around the world including XENON100 (see Chapter 2).

1.3.3 Extra Dimensions and Kaluza-Klein Particles

The notion of extra dimensions is present in most theories which try to unify gravity with quantum mechanics like string theory. The traditional 4 dimensional spacetime, a brane, is embedded in an n dimensional spacetime called the bulk with extra compactified or large dimensions, which allows gravity (for both) and the other fields (only for compactified) to freely propagate in the extra dimensions solving the hierarchy problem [40]. The presence of extra dimensions also produces a viable dark matter candidate, namely the lightest Kaluza-Klein particle (LKP), which follows from a conservation of KK-parity (momentum conservation in extra dimensions) similar to R-parity in SUSY.

A calculation of the mass for the LKP from the supposed relic density results in a range from 400 to 1200 GeV [41], which will not be probed until next generation WIMP detectors are constructed, but nonetheless provide an interesting candidate for dark matter particles.

1.4 Detection of Dark Matter

Of the dark matter candidates overviewed, the SUSY neutralino is largely the WIMP particle of interest for this study as part of a braoder electroweak parameter search from low mass (a few GeV) to high mass (a few TeV). Other topics of interest include inelastic dark matter searches, electronic recoil band signal analysis, or axion-like dark matter searches that are not constrained by SUSY parameter space. Detection of WIMPs can proceed in three ways: direct detection through scattering off target nuclei, indirect detection through annihilation products of WIMP particles, or creation in a particle accelerator. These detection methods employ a wide array of techniques and cross-checks against one another in the search for the dark matter particle.

1.4.1 Direct Detection

The results of the galactic rotation curve observations suggest that the Milky Way galaxy provides an excellent source of dark matter particles in its galactic halo with a characteristic density of ~ 0.3 GeV cm^{-3} and a velocity dispersion of 220 $\mathrm{km\,s}^{-1}$ [42, 43]. This means that hundreds to thousands of WIMPs will pass through every square centimeter of the Earth per second. As a result, one of the most promising ways to discover WIMPs is to look for a signature through interactions with normal matter predicted by the Standard Model and SUSY in an Earth-based detector, $\chi_{dm}N \rightarrow \chi_{dm}N$, characterized by the WIMP-nucleon cross section. The expected features of such an interaction in a detector along with several direct detection techniques (ionization, scintillation, and vibration) are explored.

1.4.1.1 Theoretical WIMP Scattering Rates and Annual Modulation

The theoretical basis for WIMP nuclear recoil detection is outlined extensively by Jungman, Kamionkowski, and Griest [44] and Lewin and Smith [45]. The expected elastic scattering cross section is a composition of WIMP-quark ($\chi - q$) interactions with SM and SUSY particle exchanges, which leads to predicted cross sections on the weak scale. There are two major types of interactions, spin-spin (axial-vector) and scalar, defined by their form factors, F^2. In the spin-spin case, the strength of the WIMP-nucleon interaction is coupled to the total spin of the nucleus and in the spin-independent case, its coupled to the nucleon mass.

For the spin-independent scalar interaction, where scattering is coherent across the nucleus (interaction cross section, σ), the total event rate at the Earth can be obtained simply as $R \simeq \rho_0 \sigma \langle v \rangle / m_N m_\chi$ from basic principles and extended to a differential rate, which can be written as

$$\frac{\mathrm{d}R}{\mathrm{d}Q} = \frac{\sigma_0 \rho_0}{2 m_\chi m_r^2} \mathrm{F}^2(Q) \int_{v_{min}}^{\infty} \frac{f(v)}{v} dv \tag{1.15}$$

where Q is the energy transferred from the WIMP to the nucleus, ρ_0 is the DM density, m_χ is the DM mass, $m_r = m_N m_\chi/(m_N + m_\chi)$ is the reduced mass, $f(v)$ is the velocity distribution for WIMPs, $v_{min} = (Q m_N/(2 m_r^2))^{1/2}$, and σ_0 is the zero-momentum transfer cross section, which is given by

$$\sigma_0 = \frac{4 m_r^2}{\pi} \left[Z f_p + (A - Z) f_n \right]^2 \Big] \tag{1.16}$$

with f_p and f_n, the neutralino to proton and neutron couplings usually taken to be approximately equal for spin-independent interactions, resulting in $\sigma_0 \propto A^2$. For spin-dependent interactions (the WIMP is a spin-1/2 or spin-1 field), the WIMP-nucleus scattering cross section originates from couplings of the WIMP field to the quark-axial current, which for the lightest neutralino occurs through Z boson or squark exchange [44]. These interactions are dependent on the total angular momentum of the nucleus such that only nuclei with an odd number of protons or neutrons contribute non-negligible sensitivity. The resulting cross section is modified by the addition of an axial-vector structure function term usually based on the nuclear shell model. However, for the analysis presented here only the spin-independent interactions are of interest.

The typical velocity distribution for WIMPs is taken to be Maxwellian such that $f_v \propto \exp(-v^2/v_0^2)$. The standard form factor (Woods-Saxon [46]) used for these calculations is given by

$$\mathrm{F}(Q) = \left[\frac{3j_1(qR_1)}{qR_1}\right]^2 \exp[-(qs)^2] \tag{1.17}$$

where $q = \sqrt{2m_N Q}$ is the momentum transferred, R_1 is related to the physical size of the nucleus, s is a length constant on the order of 1 fm, and j_1 is the first-order spherical Bessel function. This form factor gives the well-known exponentially falling spectrum versus energy (figure 1.8).

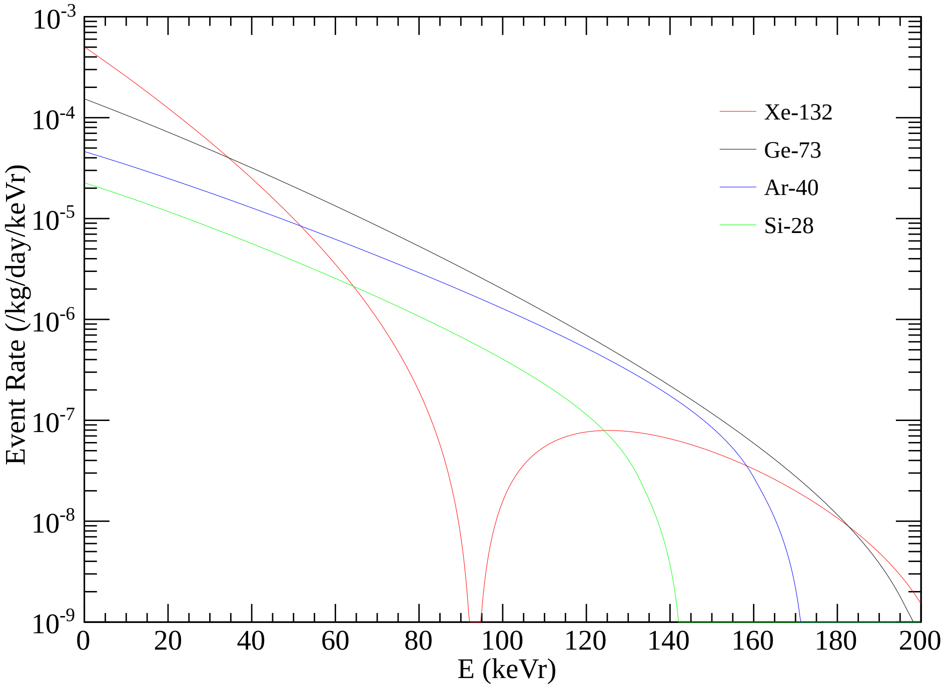

Figure 1.8: Expected WIMP rate (/kg/day/keVr) versus deposited energy (nuclear recoil equivalent) for different target material at a WIMP mass of 100 GeV and a cross section of 1×10^{-44} cm^2.

A more detailed model includes the velocity of the Earth and Sun with respect to the galaxy. This important addition allows for the prediction of another WIMP signature, namely the difference in scattering rates at certain times of the year due to the annual motion of the Earth in relation to the dark matter halo. This can be expressed in the following manner

$$v_e = v_0 \left[1.05 + 0.07\text{cos}\left(\frac{2\pi(t - t_p)}{1\ \text{yr}}\right)\right] \tag{1.18}$$

where the cosine term characterizes the annual modulation of the WIMP event rate due to the motion of the Earth around the Sun (v_e) and the Sun around the galaxy (v_0) with a maximum rate at t_p = June 2nd ± 1.3 days. The differential rate including this factor can be written as follows

$$\frac{\mathrm{d}R}{\mathrm{d}Q} = \frac{\sigma_0 \rho_0}{4 v_e m_\chi m_r^2} \mathrm{F}^2(Q) \left[\text{erf}\left(\frac{v_{min} + v_e}{v_0}\right) - \text{erf}\left(\frac{v_{min} - v_e}{v_0}\right)\right] \tag{1.19}$$

which is exclusively dependent upon astrophysical parameters. Several examples of this differential rate can be seen in figures 1.8 (for different target materials) and 1.9 (for different masses). One of the important things to note from these figures is the energy on the X-axis, here in keV$_r$ or nuclear recoil equivalent energy, as opposed to keV$_{ee}$, the electron equivalent energy. The reason for this distinction is due to the difference in quenching in the detector target between the two types of interactions for the same incoming particle energy deposit [47].

Observation of such a rate dependence in a detector requires the addition of several other factors such as the detector efficiency and threshold as well as smearing or resolution effects inherent in the physical processes and/or recording instrumentation.

1.4.1.2 Direct Detection Methods

The predicted WIMP spectra are exponentially falling with rates on the order of weak scale interactions. To detect such a particle, it is important to have an

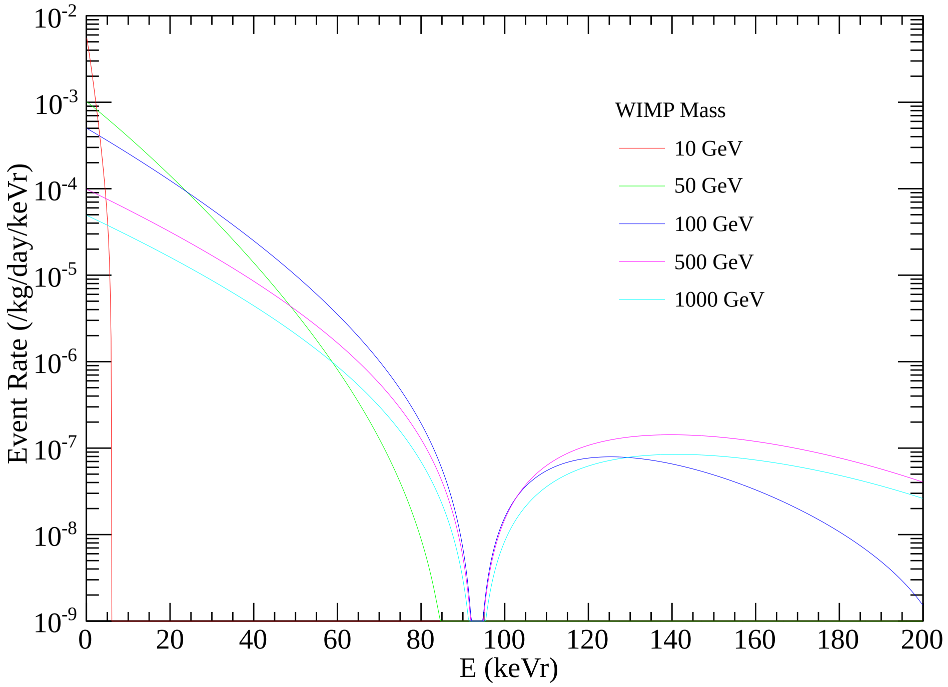

Figure 1.9: Expected WIMP rate (/kg/day/keV$_r$) versus deposited energy (nuclear recoil equivalent) for different neutralino masses for a xenon target at a cross section of 1×10^{-44} cm^2.

extremely low background environment, both through careful selection of materials and inherent background rejection techniques, and a low energy threshold, also achievable through low background, but also high observable signal yield per unit energy. The traditional WIMP signature for the direct detectors is a single scatter nuclear recoil as opposed to strongly interacting neutrons, which are prone to multiple scatter in the detector volume.

The three main methods employed to detect energy depositions in a target material are through measuring ionization, vibration (or heat), and scintillation. Depending on the material, one or several of the techniques may be used to estimate the energy of an interaction or to discriminate signal-like events from background.

Ionization electrons produced in an energy deposit may be extracted by drifting through a material by the application of an electric field. At the interface of the active detector volume, electrons that have traveled from the bulk may be collected by charge collecting wires, electrodes, or converted into scintillation in a process called electroluminescence [48]. The difference in quenching due to the field between electronic and nuclear recoils gives the ionization channel a method to discriminate background. Many of the germanium detectors as well as dual phase noble gas detectors employ information from ionization.

Scintillation photons produced from the deexcitation of excited atoms or through recombination of electron ion pairs [49] may be observed by photomultiplier tubes placed around the detector volume. The use of high quantum efficiency phototubes and highly reflective surfaces allows detectors to reach energy thresholds on the order of several keV. Additionally, the different characteristic decay times of scintillation between electronic and nuclear recoils in some materials allows for a measure of particle identification using pulse shape discrimination [50, 51]. Typical detector materials with scintillation properties are the noble gases, argon and xenon, NaI, and $CaWO_4$.

Energy deposited in a material may also be in the form of heat or phonons. Detectors designed to observe phonon pulses must be operated at extremely low temperatures (sub-Kelvin), which allows for good energy resolution and a low the energy threshold. However, no background discrimination is afforded to this detection method, as the heat produced is the same for both electronic and nuclear recoils.

Figure 1.10 gives an overview of the many direct detection experiments and

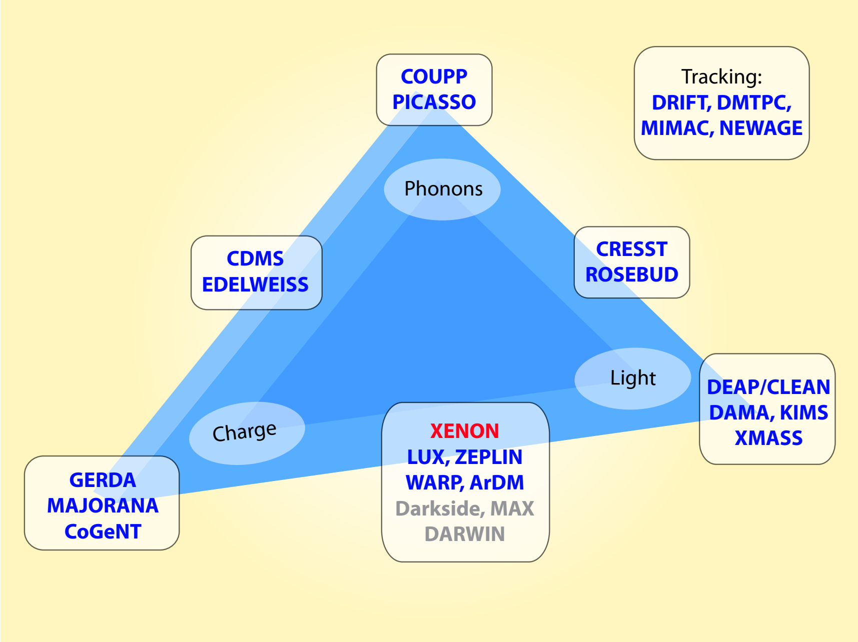

Figure 1.10: An overview of the dark matter detection community and the detection channel(s) employed. Many of the direct detection experiments are using several of the three channels to obtain better background discrimination or energy information. A handful of other detectors are attempting to use directional information or an annual modulation signature to discover a WIMP signal.

their detection techniques. The current favored detector technologies are noble liquid, both single and double phase, solid state cryogenic detectors, and other more exotic techniques.

1.4.1.3 Noble Liquid Detectors

The class of noble liquid detectors employs liquid xenon or argon for primary scintillation. In the case of dual-phase detectors, electrons drifted to the surface also produce a secondary scintillation as they are extracted into the gas phase. Background discrimination techniques for electronic recoils afforded to these types of detectors stem from pulse shape discrimination (for single phase xenon or any argon detector), self-shielding of the detector volume, or the ratio between the ionization and scintillation signals, which is known to be much larger for electronic interactions. Neutrons which only single scatter in the target volume, on the other hand, pose an irreducible background, only removed through proper material selection, characterized through extensive screening techniques, or selected by external veto criteria.

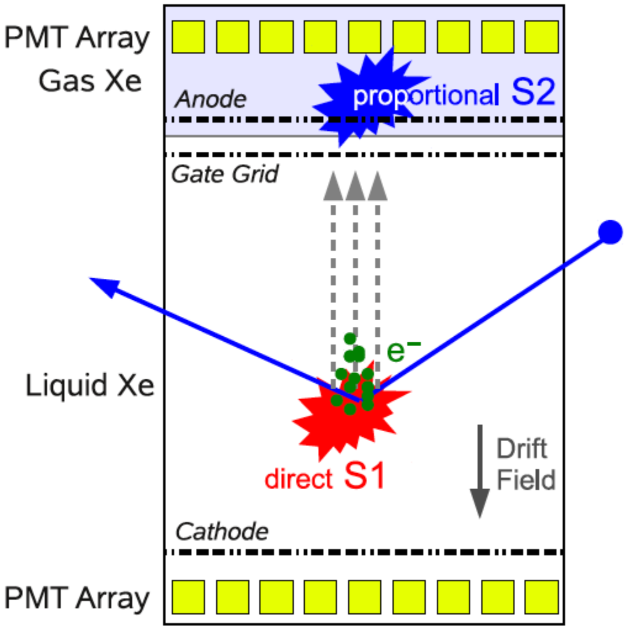

Figure 1.11: A typical schematic for a two-phase noble liquid TPC with photomultiplier tube arrays at the top and bottom of the detector. The top array provides information about the XY position of an interaction, while the time difference between the primary (S1) and secondary scintillations (S2) gives a measure of the Z position. The energy of a deposit can be obtained from both S1 and S2. Taken from [52].

The dual-phase detectors are also time projection chambers (TPC) allowing for three dimensional position reconstruction and the advantage of fiducialization for further surface background reduction. A schematic for this type of detector can be seen in figure 1.11, in which a primary scintillation (S1) at the interaction point and a secondary scintillation signal from drifted ionization electrons (S2) are observed by arrays of photomultiplier tubes (PMTs) surrounding the active detector volume. Several examples of this detector category include XENON100 [52], ZEPLINII [53], ZEPLINIII [54], LUX [55], and DarkSide [56] and a single phase detector, XMASS [57]. Perhaps the most important advantage of these detectors is their scalability to larger masses, which directly increases the sensitivity of the experiment at minimal costs and new development efforts. As a result, this technology leads the field in probing the current theorized WIMP phase space.

1.4.1.4 Cryogenic Detectors

Solid state detectors, composed of very pure crystalline structures which use ionization or scintillation, and heat to detect and measure the energies of incoming particles, are another viable technology for detection of dark matter. Using cooling technology to keep detector modules on the order of tens of mK, energy depositions even on the order of a few keV will raise the temperature of the crystal a sufficient amount to be measured using phonon sensors. Due to the small mass of these crystals, typically on the order of hundreds of grams, the external background present is overwhelming. The addition of an external electric field provides a way to drift ionization electrons and discriminate between electronic and nuclear recoils using the difference in ionization yields with respect to the phonon yield. The timing of phonon pulses are also an effective way to discriminate surface backgrounds [58].

The leading experiments in this technology are the Cryogenic Dark Matter Search (CDMS) [59] and Edelweiss [60], which both use germanium crystals equipped with phonon sensors and electrode patterns to allow for rejection of surface background, and CRESSTII [61], a $CaWO_4$ detector, which instead uses the scintillation channel for discrimination. The most serious drawback for these detector stems from inability to scale to larger masses cheaply limiting the potential sensitivity reach of these experiments.

1.4.1.5 Other Technologies

Several other detectors of interest are DAMA/LIBRA [62], a sodium-iodide (NaI) scintillation detector, and CoGeNT [63], a p-type point contact germanium detector, which have shown hints of evidence of dark matter signals, and the more traditional detection strategies of COUPP, a bubble chamber, and DRIFT, an ionization directional chamber.

DAMA/LIBRA uses NaI crystal scintillators to search for the annual modulation signature of $\sim$7% in the galactic halo dark matter rate with a predicted maximum around June 2nd. Results over the past decade from DAMA have suggested the existence of a 60 GeV WIMP at a scattering cross section on the order of 10^{-41} cm^2 from their studies of the modulation amplitudes as shown in figure 1.12 (a second region of significance is around 10 GeV and 10^{-40} cm^2). The presence of a modulation is only apparent at very low energies ($<$10 keV$_{ee}$) and follows the June 2nd maximum leading to greater than 8σ significance. Several experiments, including CDMS, Edelweiss, XENON, and ZEPLINIII, have probed the phase space inferred by these claims and found no evidence of a signal. Despite this lack of observation from other collaborations, DAMA maintains their signal is due to the presence of dark matter from the galactic halo.

CoGeNT, an ultra-low noise germanium detector with very good energy res-

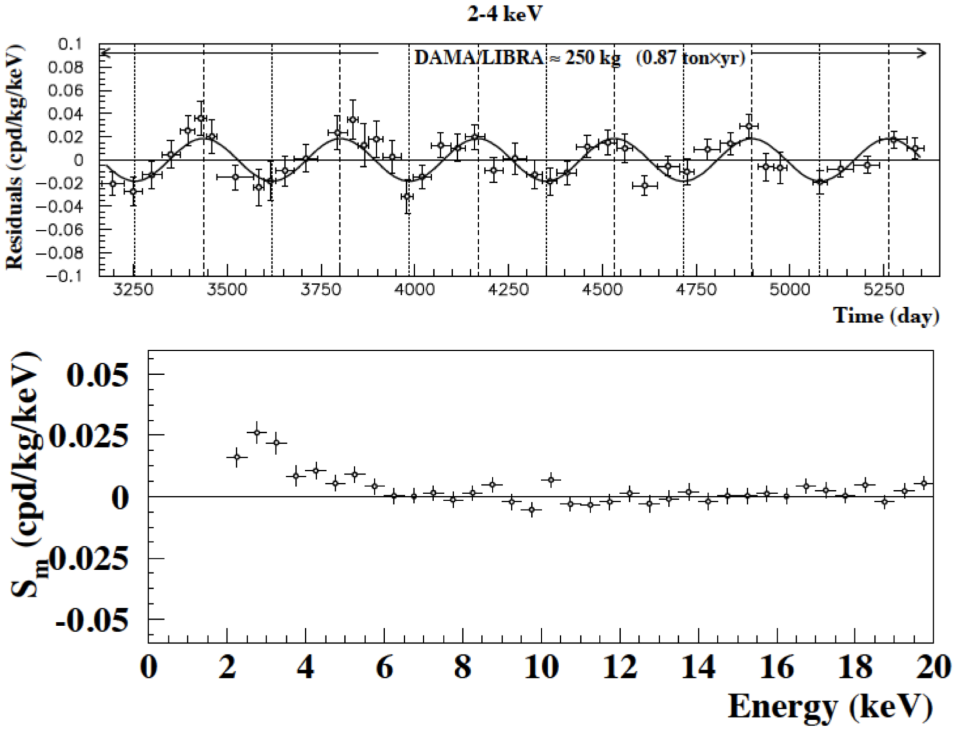

Figure 1.12: *Top Panel:* Annual rate modulation in the DAMA/LIBRA experiment in the energy range of 2-4 keV$_{ee}$ over a period of 5000 days with a period of (0.999±0.002 yrs) and maximum near June 2nd. *Bottom Panel:* Magnitude of modulation versus the energy, which peaks at around 3 keV$_{ee}$ with a rate of 0.25 events/kg/keV$_{ee}$. Taken from [62].

olution, has published evidence of an excess of events indicative of a low mass WIMP on the order of 7-10 GeV. The energy spectrum can be seen in figure 1.13 where they show an exponential increase in event rate from about 2 keVee down to their energy threshold of 0.4 keVee. Attempts to reconcile this observation with the annual modulation results of DAMA from scattering off sodium have been the focus of many phenomenological efforts over the past few years [64, 65]. A snapshot of the WIMP phase space before XENON100 2012 results are shown in figure 1.14.

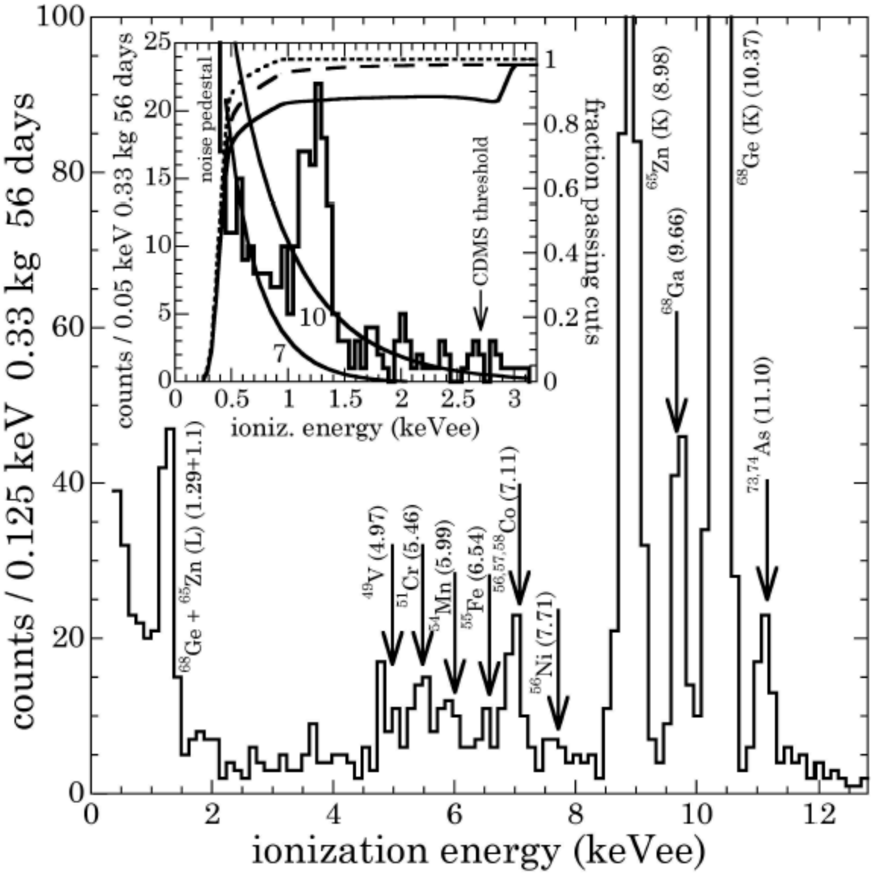

Figure 1.13: Energy spectrum of CoGeNT data at energies near the detector threshold of 0.25 keV$_{ee}$. The powerful energy resolution allows for the observation of low energy lines for calibration. The inset shows the exponentially rising event rate overplotted with different WIMP mass and cross section assumptions. Taken from [63].

A substantial portion of this work is dedicated to understanding this low mass region of the WIMP phase space and the implications stemming from Xenon100 data.

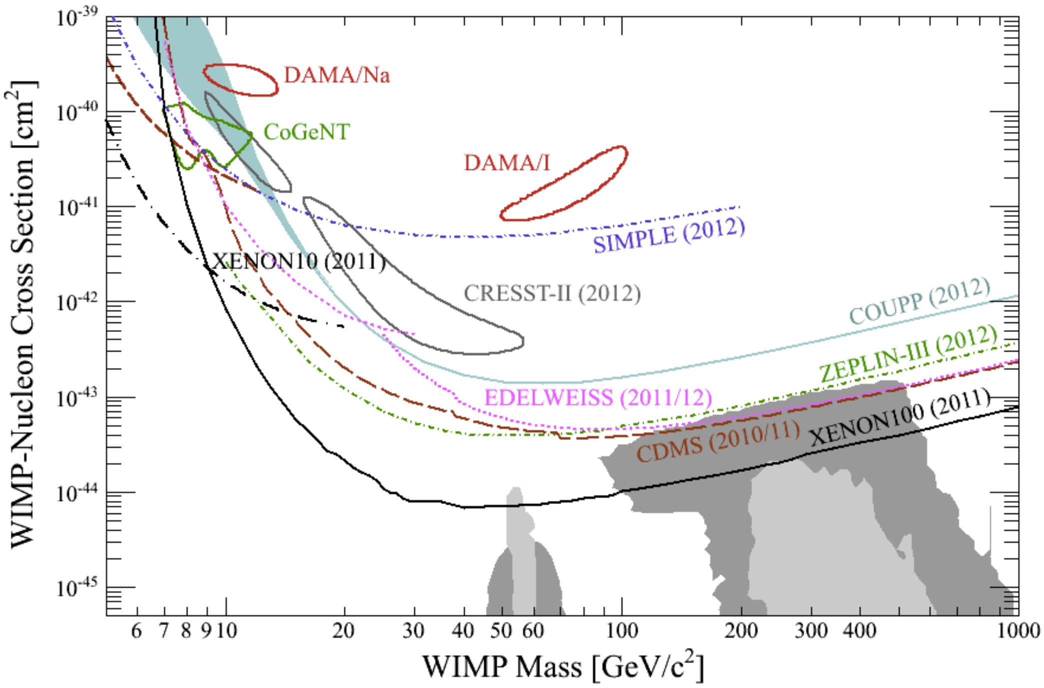

Figure 1.14: WIMP mass versus cross section phase space with expected region predicted by MSSM [66, 67, 68] along with exclusion limits and discovery regions from DAMA/LIBRA and CoGeNT at lower masses. Plot modified from [69].

1.4.2 Indirect Detection and Collider Searches

Another way to detect dark matter is indirectly through observation of WIMP annihilation products, where incoming flux is dependent on the square of the dark matter density ($\Gamma_A \propto \rho^2_{DM}$). For these indirect searches, it is typical to look in regions of proposed high dark matter density such as the galactic center for monoenergtic gamma lines from either $\chi_{dm}\chi_{dm}\to\gamma\gamma$ or $\chi_{dm}\chi_{dm}\to\gamma Z$ as in Egret [70] or Glast [71], or throughout the halo for charged particles (electron-position fraction) by AMS-02 [72] or Pamela [73]. The latter method for Pamela in 2009 in particular has produced observations of a positron rate in excess of the predicted rate from just cosmic-ray nuclei and interstellar matter interactions, which may be attributable to dark matter annihilations or position production from nearby pulsars [74].

In colliders, evidence for WIMPs can be found through dark matter pair production ($NN \rightarrow \chi_{dm}\chi_{dm}$) with initial state radiation leading to mono-jet, mono-photon, or mono-Z signals with large missing E_t [75, 76, 77]. So far, searches at both the Tevatron and more recently the LHC have yielded no evidence for supersymmetry or model-independent dark matter signal hints.

CHAPTER 2

XENON100

To search for WIMP dark matter, the XENON100 detector is being operated in the Gran Sasso mountains in the Abruzzo region of Italy. Located in a small cavern in the adjoining tunnels to the main halls of the Laboratori Nazionali del Gran Sasso in a meter thick shield, the instrument observes particle interactions occurring in a two-phase xenon time projection chamber (TPC) through ionization and scintillation processes. This chapter details the principles of radiation detection in liquid xenon, the infrastructure of the XENON100 TPC, the composition of the shielding enclosure, properties of cooling and recirculation, the slow control monitoring system, and data acquisition.

2.1 Liquid Xenon Physics and Two-Phase TPC

Detection of dark matter requires the precise knowledge of the energy and particle type of an interaction. The XENON100 detector takes advantage of liquid xenon's scintillation and ionization properties to achieve both; the energy scale can be determined from either channel using results from dedicated external measurements and the ratio of the two gives a method of background discrimination (or particle identification).

2.1.1 Ionization

Particles which deposit energy in liquid xenon produce electron-ion pairs, excited atoms, and free electrons with kinetic energies below the first excited level of the xenon atom [78]. The energy deposited into the individual channels is determined by the Platzman equation for rare gases (equation 2.1) and the characteristic energy required to create one electron-hole pair, W. Measurements have determined that the ionization energy in liquid xenon is 15.6 ± 0.3 [79], such that the total energy deposit of the interaction may be inferred from the ionization signal

$$E_d = N_i E_i + N_{ex} E_x + N_i \epsilon, W = E_d/N_i = E_i + E_x(N_{ex}/N_i) + \epsilon \tag{2.1}$$

where N_i is the number of electron-ion pairs, N_{ex} is the number of excited atoms, and E_i, E_x, and ϵ are the energies of the pairs, excited electrons, and kinetic energy of subexcitation electrons.

This signal can be measured by applying a constant external electric field potential to prevent electrons from recombining and then drift them to a charge collecting mechanism. Practical limitations of finite electric fields and impurities in the liquid xenon allow only a portion of the total ionization electrons to be collected. Some of the electron-ion pairs recombine, while drifting electrons may become attached to electronegative impurities such as oxygen or nitrogen. This results in a secondary attenuation (after finite field) characterized by the electron lifetime (usually on the order of several hundred μs) measured through detector calibrations and corrected in software. This remaining ionization signal can be observed when the drifted electrons reach the liquid-gas interface and are converted to a secondary scintillation signal in a process called electroluminescence.

2.1.2 Recombination and Primary Scintillation

Though the characteristic recombination process in noble liquids has been modeled by Onsager [80], Thomas-Imel [81], and others, a fully consistent model has not yet been achieved that predicts the experimental data for the electric field, the ionization density of tracks, and the energy dependences. Nevertheless, the liquid xenon community has proceeded in using measurements that characterize these limiting cases for use in applications.

This data is used to characterize the recombination of electron-ion pairs that are not extracted by the external applied electric field, which along with the deexcitation of excited atoms (equations 2.2 and 2.3), produce scintillation light in the vacuum ultraviolet (VUV) regime centered at 177.6 nm [49].

$$\begin{aligned} \mathrm{Xe}^{+} + \mathrm{Xe} &\rightarrow \mathrm{Xe}_2^{+} \\ \mathrm{Xe}_2^{+} + \mathrm{e}^{-} &\rightarrow \mathrm{Xe}^{**} + \mathrm{Xe} \\ \mathrm{Xe}^{**} &\rightarrow \mathrm{Xe}^{*} + \mathrm{heat} \\ \mathrm{Xe}^{*} + \mathrm{Xe} &\rightarrow \mathrm{Xe}_2^{*} \\ \mathrm{Xe}_2^{2} &\rightarrow 2\mathrm{Xe} + h\nu. \end{aligned} \tag{2.2}$$

$$\begin{aligned} \mathrm{Xe}^{*} + \mathrm{Xe} &\rightarrow \mathrm{Xe}_2^{*} \\ \mathrm{Xe}_2^{*} &\rightarrow 2\mathrm{Xe} + h\nu. \end{aligned} \tag{2.3}$$

The excitation of the xenon atoms into singlet and triplet states of the dimer Xe_2^2 creates scintillation with two characteristic decay time components (depending on the radiation and electric field applied) on the order of tens of nanoseconds [82], which allows for identification of the interacting particle. Application of an electric field reduces the difference in decay times to a negligible factor, such that it is no longer considered for dual-phase detectors.

The degree of transparency of liquid xenon to the VUV scintillation light [83] allows the photons to be detected with photomultiplier tubes surrounding the active volume. This scintillation signal may be attenuated by both elastic scattering of photons (mostly Rayleigh scattering with a characteristic length of $\sim$ 30 cm [84]) and by impurities including water vapor, a common contaminant due to outgassing of internal detector materials. The necessity for purity for both electron drift and scintillation yield requires the continuous circulation and removal of impurities of the liquid xenon volume.

2.1.3 Electroluminescence

Under the influence of a very large electric field ($\sim$10 kV/cm), electrons traveling in either liquid or gas xenon can create photons in a process called proportional scintillation or electroluminescence. In the XENON100 TPC, the amount of light produced at the liquid gas interface is highly dependent on the field and characteristics of the gas as shown in equation 2.4

$$N_\gamma = \alpha N_e (E/p - \beta) p d \tag{2.4}$$

where N_γ and N_e are the number of proportional photons and ionization electrons, p is the pressure of the xenon gas, E is the extraction field, d is the gas gap distance, α is an amplification factor, and β is related to the threshold of proportional scintillation emission. The proportion of extracted electrons from the surface of the liquid is 100% for fields larger than 10 kV/cm [85].

2.1.4 Two-Phase TPC and Discrimination

The discrimination power afforded to liquid xenon detectors stems from the inherent differences in ionization density along the tracks of electrons such as from gamma ray interactions versus neutrons or other nuclear recoils. The gamma rays are known to produce sparsely populated tracks [85], such that the electric field is able to more effectively strip off electrons while alpha or neutron tracks have dense cores, which result in a high recombination rate. This causes electronic recoils to produce much more proportional scintillation (S2) than primary scintillation (S1) as compared to nuclear recoil interactions.

This ratio between the S1 and S2 gives a powerful tool for liquid xenon detectors to discriminate between different types of incoming particles giving about a factor of 100-10000 rejection power depending on the electric fields applied [52, 86]. An additional parameter for discrimination, also related to the track length in the liquid, is from the time width of the S2 signal (on the order of μs). Due to the longer gamma ray tracks, the diffusion of the electron cloud during drift is spread over time more than a neutron interaction would be. The difference in widths between electronic or nuclear recoil energy depositions is characterized by an analysis cut on neutron calibration data of S2 widths.

The XY position of an event in the detector is determined by the signal pattern of the secondary scintillation light on the PMTs while the Z position is obtained from the time difference between the primary and secondary scintillation signals. The resolution afforded to the detector is related to the size of the PMTs used (for XY) and the drift speed and liquid-gas gap at the interface (for the Z position). This allows for the detection of both single and multiple scatters to the degree achieved by the detector instrumentation. Additionally, the possibility for fiducialization affords the detector further gamma background reduction by the high atomic number ($Z = 54$) and density (~ 3 g/cm^3) of liquid xenon.

2.1.5 Energy Scales

For observation of dark matter, we are interested in looking for nuclear recoils and we require conversions from the visible signal i.e S1 and S2 in photoelectrons (PE), to the respective nuclear recoil equivalent energy i.e. the energy deposited. Typically this is performed through the use of the relative scintillation efficiency, $\mathcal{L}_{eff}$ for S1 and the ionization yield $\mathcal{Q}_y$ for S2.

2.1.5.1 Relative Scintillation Efficiency

The conversion from S1 photoelectrons observed to the nuclear recoil energy is dependent upon the ratio between the scintillation yields of electronic and nuclear recoils in the following way

$$E_{nr} = \frac{\mathrm{S1}}{\mathcal{L_Y}(122\mathrm{keV_{ee}})} \frac{1}{\mathcal{L}_{eff}(E_{nr})} \frac{S_{ee}}{S_{nr}} \tag{2.5}$$

where $\mathcal{L_Y}$ is the light yield at 122 keVee (with field) and S_{ee} and S_{nr} are field dependent quantities for the quenching of electronic and nuclear recoil energy deposits, and $\mathcal{L}_{eff}$ is defined to be the ratio of the scintillation yield of nuclear recoils to the scintillation yield of electron recoils at 122 keV electron-equivalent energy (i.e. from that of γ-rays from a ^{57}Co source). The observed S1 is first converted to an energy in keVee through the field-dependent LY and S_{ee}/S_{nr} and then to nuclear recoil energy through the dimensionless relative scintillation efficiency, $\mathcal{L}_{eff}$.

Many direct measurements [87, 88, 89, 90, 91] and indirect methods have been performed to determine the relative scintillation efficiency with the most recent measurement down to 3 keV$_\mathrm{r}$. The dedicated experiments are typically performed through measurements of monoenergetic neutrons elastically scattering at fixed-angles using the traditional kinematics of energy deposition and angular dependence to determine the energy deposited. The results are shown in figure 2.1 for several different experimental setups.

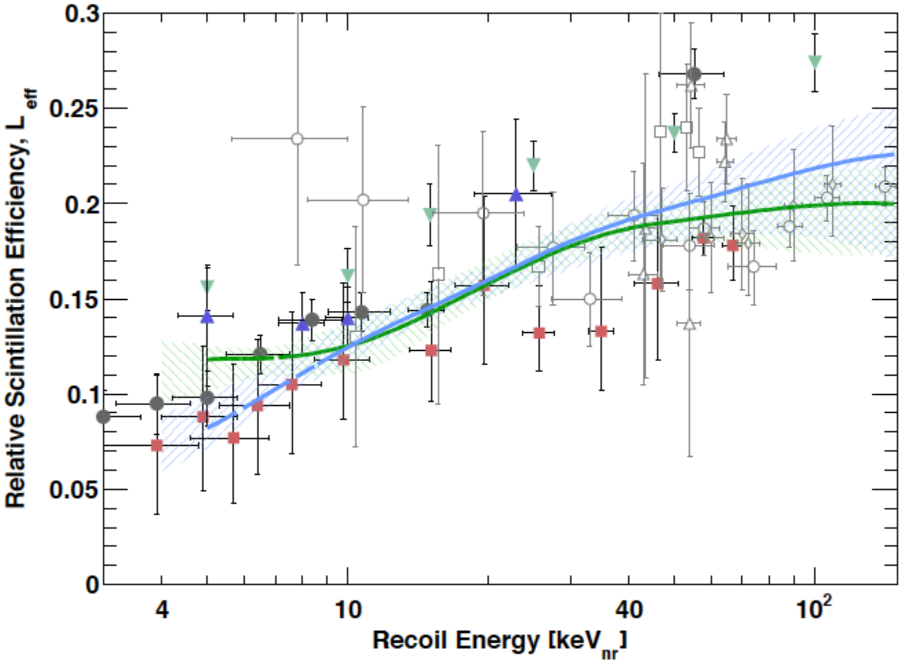

Figure 2.1: Current landscape of measurements of relative scintillation efficiency used to convert primary scintillation measurements into a nuclear recoil energy scale. Hatched areas and solid lines are obtained from indirect measurements of $\mathcal{L}_{eff}$. Taken from [92].

From this figure, it is evident that there are significant systematics present increasing the uncertainty in any measurement of the energy of an event using the primary scintillation signal. Additionally, due to the statistical fluctuations afforded to the Poisson processes of the electron and photon creation in the interaction and photodevice conversion of photons to recorded photoelectrons, extrapolation below 3 keV$_\mathrm{r}$ of the $\mathcal{L}_{eff}$ is particularly of interest for the exponentially falling WIMP spectrum. This extrapolation and uncertainty has been the target of much controversy regarding any low mass WIMP results from liquid xenon detectors [93].

2.1.5.2 Ionization Yield

Simultaneously, the S2 signal can be used to measure the energy of an interaction with the ionization yield, $\mathcal{Q}_y$ in units of electrons per keV$_\mathrm{r}$

$$E_{nr} = \frac{\mathrm{S2}}{\mathcal{Q}_y \alpha_{se}} \tag{2.6}$$

where α_{se} is a detector dependent conversion parameter from the electroluminescence process in units of photoelectrons per electron. Measurements of the ionization yield for different electric field strengths and nuclear recoil energies are shown in figure 2.2.

The measurements of both the relative scintillation efficiency and ionization yield give liquid xenon detectors the flexibility to infer the energy from both the primary and proportional scintillation signals depending on necessity. The inherent advantages to each lie in the quantity of measurements for $\mathcal{L}_{eff}$ and for the decrease in statistical uncertainty for $\mathcal{Q}_y$. In chapter 5, we'll take a closer look at how these energy scale conversions are applicable to the detector.

2.2 XENON100 Time Projection Chamber

The inner portion of the XENON100 detector consists of a TPC of 152.4 mm radius and 305 mm height with 62 kg of liquid xenon in an active volume optically separated from a veto region by 24 polytetrafluoroethylene (PTFE) panels. The

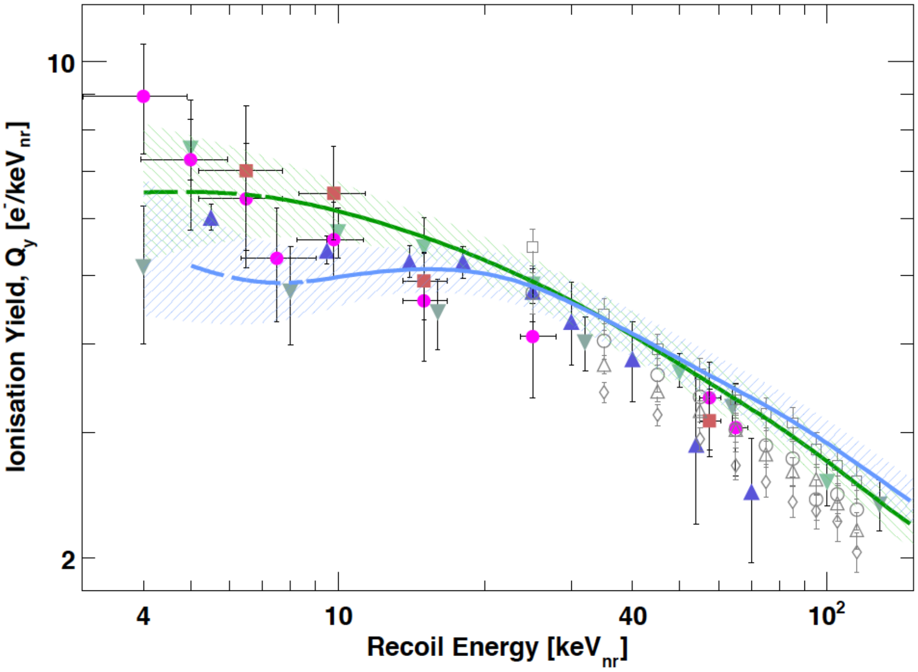

Figure 2.2: Current landscape of measurements of the ionization yield in liquid xenon for conversion of recoil energy into drifted electrons. Taken from [92].

veto contains an additional 99 kg of xenon and provides a diagnostic tool and additional background reduction through operation in anti-coincidence mode. Photomultiplier tubes placed at the top and bottom of the TPC and in the veto region readout xenon scintillation light to characterize interactions in the liquid xenon. An applied electric field vertically across the active volume provides a drift field for electrons to the ionization channel in a secondary scintillation (S2) through electroluminescence.

2.2.1 Photomultiplier Tubes

In the active region of the TPC, 178 Hamamatsu R8520 low temperature bialkali 1-inch low radioactivity PMTs are arranged at the top and bottom to observe

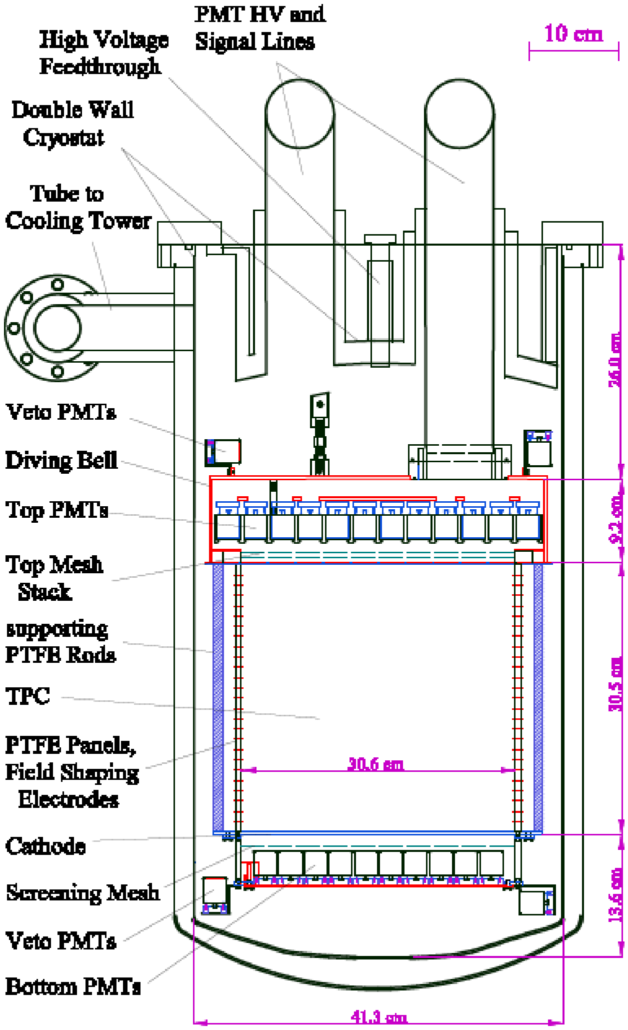

Figure 2.3: Schematic of the XENON100 TPC with the inner (active) volume, meshes, field shaping wires, external veto volume, PMT arrays at the top and bottom, and interfaces to other external systems. Taken from [52].

scintillation photons (figure 2.4). An additional 64 are placed in the veto region just outside the active volume to provide an additional way to tag multiple scatter events.

The 80 PMTs at the bottom of the volume collect most of the light ($\sim 80\%$)

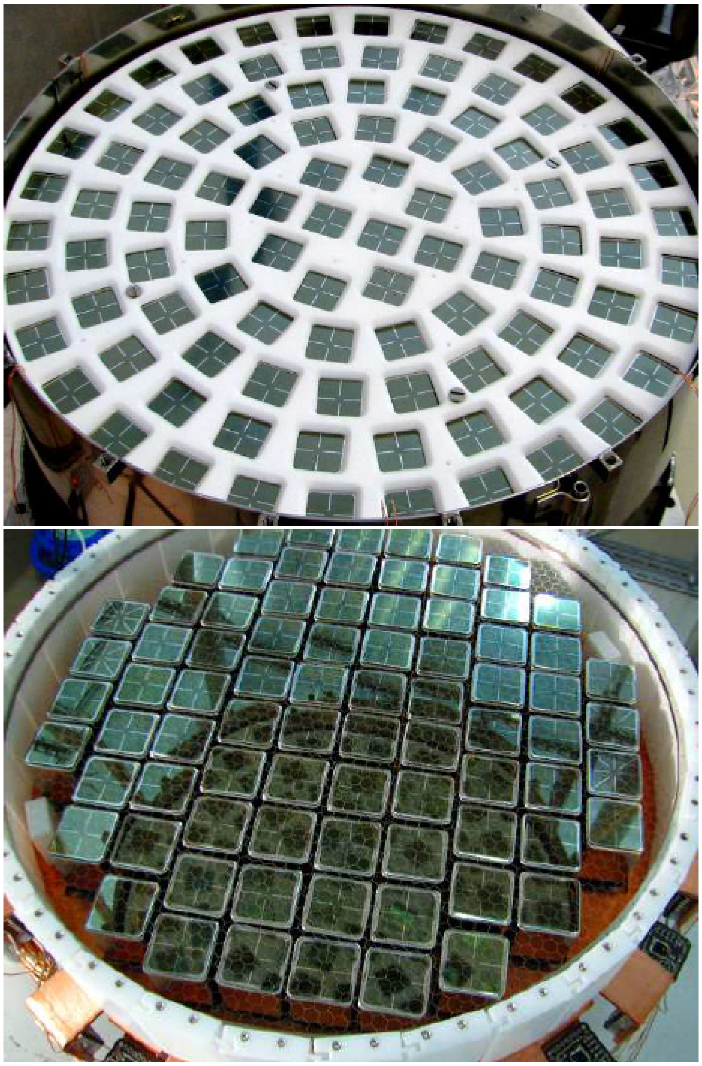

Figure 2.4: *Top Panel*: Top PMT array containing 98 PMTs arranged in circular rings to aid in radial position reconstruction. About 43% is covered by active PMT photocathode area. *Bottom Panel*: Bottom PMT array containing 80 PMTs densely packed to observe primary scintillation light with high QE from total batch with about 52% coverage. Taken from [52].

from the primary scintillation due to the reflection of photons at the liquid-gas xenon interface ($n_{Xe} = 1.69 \pm 0.02$ [94]) and were chosen from the total batch to have the highest quantum efficiency of around 30%. The pattern at the bottom shown in figure 2.4 has approximately 52% PMT photocathode coverage. The 98 PMTs at the top of the detector are placed in multiple circular rings to improve radial position reconstruction information inferred from the localization of the S2 pattern and have an average quantum efficiency of 23% with 43% photocathode coverage. The outer ring of this arrangement extends beyond the PTFE wall to improve position reconstruction near the edges.

PTFE insulated and Kapton insulated cables attached to the low radioactive PMT Cirlex® base voltage divider read the signal and supply the high voltage necessary to operate the phototube. These cables for each of the 242 PMTs are grouped into bunches which are guided to the top of the bell where they are then routed through one of the tubes in the cryostat to the data acquisition (CAEN VME) and high voltage supply (CAEN HV) systems.

2.2.2 Electric Field Cage

The electric field for drifting electrons is supplied by a combination of thin metal meshes with high optical transparency chemically etched from stainless steel foils, and copper wires acting as electrodes, which create uniform field lines in the target volume. Two meshes at the bottom of the detector are placed above the PMT array to provide shielding and to supply a cathode voltage of -16 kilovolts (higher potentials are likely limited by field emission near sharp edges of the mesh). The chain of 40 copper wire rings are equally spaced along the Z axis separated by 700 MΩ resistors giving a field of -0.53 V/cm. This field results in an electron drift velocity of 1.78 mm/μs [95].

The presence of a liquid gap between the bottom PMTs and the cathode results in a charge insensitive region in which electrons are not drifted to the gas

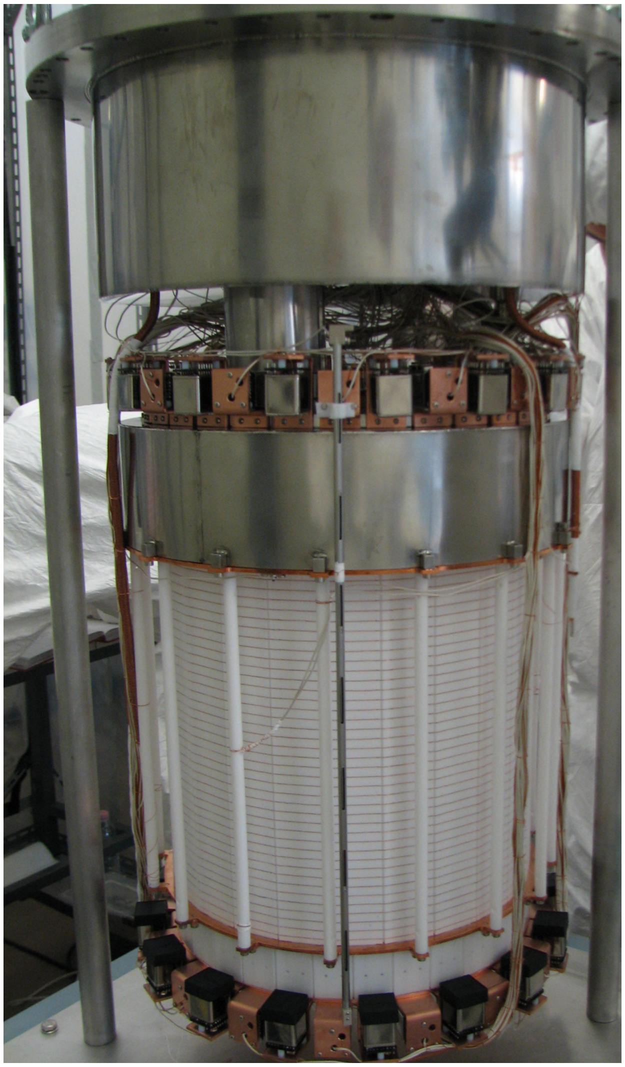

Figure 2.5: The interlocking PTFE panels are seen with the external field shaping wires surrounding the active volume. The PMTs overlooking the veto volume are at the top and bottom.

phase allowing for the possibility of double scatter events recognizable only as a single scatter due to the presence of a sole ionization signal. The loss of a second ionization signal results in the ratio of S2 to S1 to decrease, which leads to the possibility of a gamma event behaving like a neutron. This type of background forms perhaps the biggest challenge for this type of detector.

To provide an electric field for electroluminescence in the gas phase, three additional meshes are placed around the liquid-gas interface. The first is a grounding mesh just beneath the liquid surface, which effectively terminates the drift field. The field in the gas is generated by an anode mesh with 4.4-4.5 kV potential fixed at 5 mm above the grounded mesh. This field can be adjusted by raising or lowering the liquid level to achieve a field in the gas of about 12 kV/cm, which results in almost 100% efficiency in extracting drifted electrons. A third mesh (grounded) shields the top PMTs from the anode potential. The detector contains two set screws to tilt the detector allowing for the liquid surface to be parallel to the anode mesh to minimize the position dependence of the S2 signal. This leveling is performed through measurement of either the capacitances of four level meters with partially-filled liquid xenon stainless steel tubes or the widths of the ionization signal at various XY positions.

2.2.3 Veto Detector

The liquid xenon veto is optically separated from the active volume by the interlocking PTFE panels (figure 2.5) and provides a useful diagnostic tool to probe low energy neutron multiple scatters and actively veto multiple scatter interactions. The PTFE panels are highly reflective (99% reflectivity [96]) to preserve the majority of primary scintillation light both inside and outside the TPC. The extra layer of xenon in the veto provides additional passive shielding from external radiation and reduces the rate of accidental coincidences in the target volume. The 99 kg of liquid xenon is instrumented with only 64 PMTs, which reduces the effective cost of the detector while providing a method of discrimination.

The difficulties inherent with the veto stem from the inability to ascertain the position dependent light yield and in extracting information from energy depositions in the veto detector simulations. As a result, the anti-coincidence criteria are simplified to a very basic level (single photoelectron) with no consideration of the incoming direction, energy, or particle type.

2.3 External Structure

The Xenon100 TPC and veto provide the means to observe single scatter nuclear recoils with high rejection power against external gamma backgrounds. However, both the neutron and electromagnetic background can be significantly reduced with the addition of an extensive shielding enclosure and cryostat. The detector is instrumented inside a diving bell, which allows for total liquid coverage around the full TPC (for the veto) and minimizes liquid and gas xenon fluctuations through pressurization of the gas layer giving a precise liquid level. This is placed inside a double-walled stainless steel 316Ti cryostat (figure 2.6), which contains pipes for signal and high voltage cables and feedthroughs, and external cooling apparatuses attached to the inside wall of the shielding.

At a depth of 3700 m water equivalent, which reduces the muon flux by a factor of 10^6 to about 1 muon/m^3/hr [97], the majority of external backgrounds for the detector will originate from the surrounding Gran Sasso mountain cavern. The cryostat is placed inside several layers of passive shielding materials to reduce this remaining background. The outer shielding layer consists of two types of lead of 15 and 5 cm thicknesses where the inner layer has a reduced radioactive ^{210}Pb component. The high atomic mass of lead makes it an excellent attenuator for the external gamma and x-rays.

The next layer is composed of 20 cm thick polyethylene, which serves to

Figure 2.6: External shielding enclosure and cryostat attached to the right wall. The shield is composed of two layers of lead, polyethylene, and copper. The stainless steel cryostat has a copper ring surrounding it for detector calibrations.

reduce external neutron energies through thermalization (elastic scatters due to the neutron's short mean free path) allowing them to be radiatively captured before they reach the detector. The final shielding layer is a 5 cm ultrapure oxygen-free high-conductivity copper layer which shields from the radioactivity emanating from the polyethylene and lead layers. The region between the copper and cryostat is continuously flushed with gas nitrogen to prevent radon from entering into the shield, which tends to adhere to the surfaces of materials or diffuse through leaks into the liquid xenon.

The shielding setup effectively attenuates the external background as the majority of remaining radioactive background entering the liquid xenon arises from both internal sources and the PMT materials as obtained from studies the electromagnetic background spectrum and simulations [98] and input screening values (section 2.4).

2.4 Radioactive Screening and Materials Selection

The materials implemented in the XENON100 detector have undergone an extensive series of radioactive assaying and been chosen based on their results as detailed here [99]. The measurements of the materials were performed in the GATOR screening facility [100], a high purity p-type coaxial germanium detector enclosed in a copper cryostat and lead/copper shield, and the LNGS counting facility, also high purity germanium detectors with larger volume (GeMPI-I,II). The results of the screening from these facilities can be seen in table 2.1 for the content from ^{238}U, ^{232}Th, ^{40}K, and ^{60}Co.

These screening results not only predict the expected gamma background but also the neutron background due to spontaneous fission and alpha-n reactions inferred from the SOURCES [101] package for neutron cross sections (usually under the assumption of equilibrium in the decay chain). The remaining background for the detector, from internal sources in the liquid xenon, is understood through analysis methods involving delayed coincidence timings, or through direct mea-

			Radioactivity (mBq/unit)			
Material	Unit	Quantity	^{238}U	^{232}Th	^{40}K	^{60}Co
PMTs	pc	242	0.15	0.17	11	0.6
PMT Bases	pc	242	0.16	0.07	0.16	0.01
PTFE	kg	11.8	0.31	0.16	2.25	0.11
Cryostat (SS)	kg	73.6	1.65	2.00	9.00	5.50
Copper Plate	kg	3.88	0.22	0.18	1.34	0.24
Copper Shield	kg	2.1×10^3	0.08	0.02	0.04	0.00
Polyethylene Shield	kg	1.6×10^3	0.23	0.094	0.7	0.89

Table 2.1: Several of the important input parameters for the XENON100 Geant4 Monte Carlo Model, which have been averaged over the selected materials for the detector

surements (as for krypton through a Residual Gas Mass Spectrometer).

2.5 Detector Recirculation, Cooling, Purification and Stability

Xenon gas circulates through the detector by introduction to the TPC through a diving bell at the top and a pipe at the bottom of the veto region. An external pulse tube refrigerator (PTR) with 200 W of cooling power, attached directly to a copper block inside the cryostat that acts as a cold finger, liquifies the circulated gas from several cylinders, which then drips into the veto and TPC. A proportional-integral-derivative controller regulates the temperature through heating of the cold head to maintain a stable internal environment.

The xenon gas purification system is essential for sustaining a high light yield and low background rate necessary for WIMP detection. A high temperature zirconium getter (SAEX MonoTorr PS3-MT3-R/N-1/2) in the recirculation cycle removes electronegative impurities in the gas such as water, oxygen, and nitrogen, which absorb scintillation light and attach themselves to drifting electrons, to the part per billion level (ppb) by chemically bonding impurities to the getter material. The purified xenon gas reenters the detector through the pipe in the diving bell and may again be liquified at the copper cold finger.

In addition to the electronegative impurities, both krypton and radon pose significant background concerns. Krypton, introduced into the atmosphere as part of nuclear weapons testing and nuclear power plant accidents, is found in xenon when gathered from the atmosphere; it contains the isotope ^{85}Kr, which has a low energy beta decay with an endpoint of 687 keV and half-life of 10.87 years, and is difficult to remove from the xenon. Radon is easily dissolved in the liquid xenon either through diffusion due to leaks or from emanation from internal detector materials i.e. PTFE or PMT surfaces; the radon daughters produce both alpha and gamma decays with an initial half-life of 3.8 days and nuclear recoils. The techniques for removal of radon are still under development so the most effective ways to mitigate the radon background is to prevent it through careful material preparation and cleaning in a dedicated clean room.

Krypton may be removed from the liquid xenon in a distillation column (figure 2.7) due to their differing boiling point temperatures. Liquid xenon (165 K) and krypton (120 K) present in the xenon are passed through a constant temperature gradient along the length of the column. Because the xenon will boil off faster, it is possible to retain krypton depleted xenon gas at the top of the column, which can then be sent through the column repeatedly. This process has a speed of about 0.6 kg/hour, such that it takes about two weeks to pass

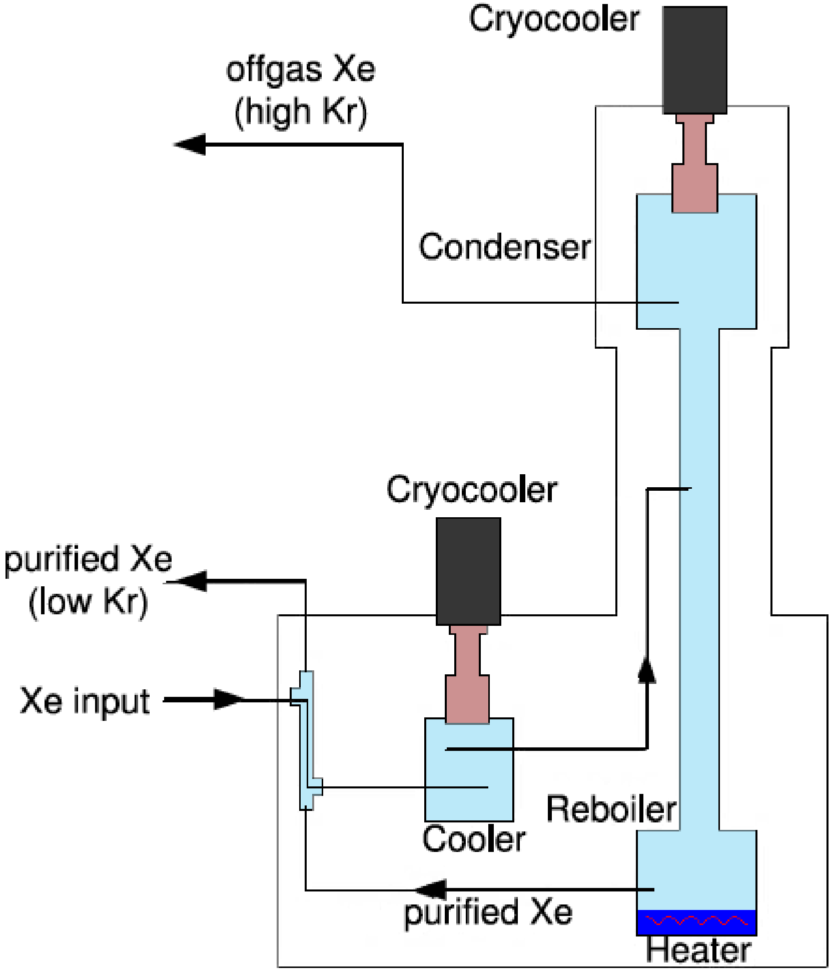

Figure 2.7: A schematic of the krypton distillation column, which is used to remove krypton and its beta-decaying isotope, ^{85}Kr, from the liquid xenon. Taken from [52].

the full detector mass of xenon, with each individual pass reducing the krypton proportion by a factor 100-1000 from the ppb level to the ppt (parts per trillion) level.

The detector operation is overseen by a continuously monitoring slow control system [102], which relays information about detector properties such as temperature, pressure, voltages, flow rates, and other variables of interest to ensure the stability conditions required for the dark matter search over the lifetime of the detector (several years). Data samples taken at the sub-Hz level are used for both monitoring, possibly for correlations with abnormalities observed in data as well as stability, and safety management, in temperature control or other sensitive areas.

2.6 Data Acquisition and Data Processing

The data acquisition system (DAQ) consists of the trigger, data digitization, and data storage feeding into the software data processor, which allows for simple data analysis. PMT signals are digitized by a CAEN VME V1724 Flash ADC with 100 MHz sampling rate, 14-bit resolution, and 2.25 V full scale, which allows for practically deadtime-less measurements during background data taking conditions ($\sim$1 Hz). A sum of 84 PMT (68 from the top and 16 from the bottom) channels forms the majority, or S2 trigger, such that with a signal threshold for digitization on an individual channel of $\sim$0.3 PE, a 100% trigger efficiency can be achieved at 150 S2 PE. Once an event is triggered (most likely from an S2), a $\pm$200 μs window around the trigger (more than the drift length of the detector, 176 μs) is digitized and recorded for all individual channels, which surpass the digitizer threshold (figure 2.8).

The processor takes the digitized waveforms and characterizes each peak within that event based on its area, width, height, and PMT information into primary or secondary scintillation category. Using inputs from PMT gain calibrations and detector specific corrections (S2 electron lifetime, S1 position dependent light yield, and S2 XY position), the resulting output contains several important

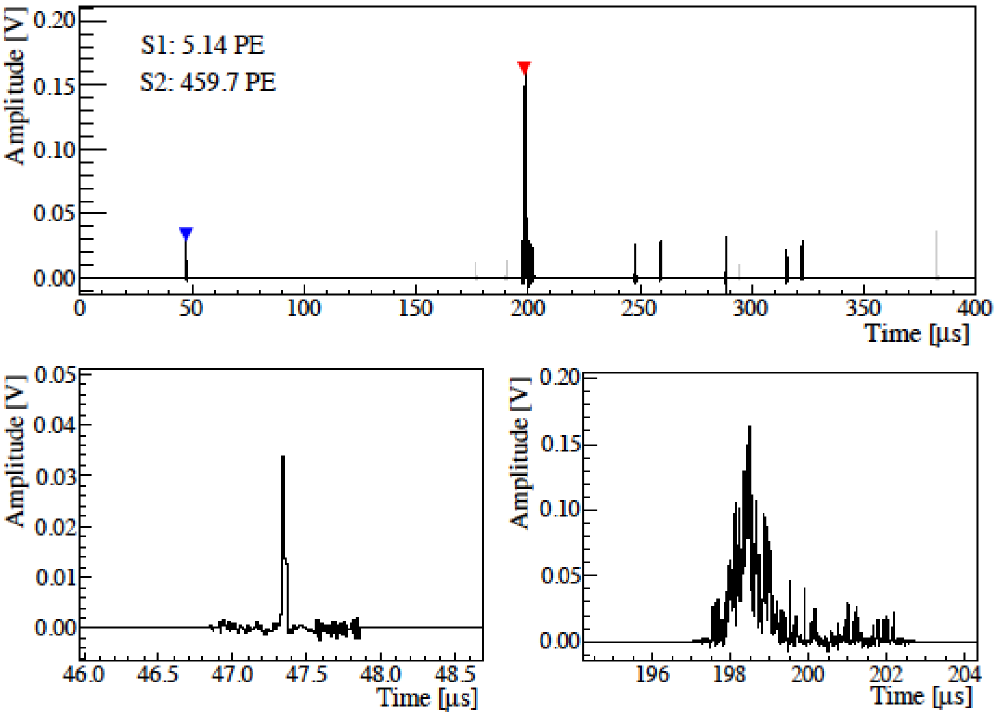

Figure 2.8: A waveform of a low energy gamma background event. *Top:* Total waveform over the 400 μs digitization window for the sum across the 178 PMTs surrounding the TPC, which shows the timing of the S1 (*blue*) and S2 (*red*). The small peaks after the main S2 peak are from single electrons extracted into the gas phase. *Bottom:* Zoomed views of the S1 (5.14 PE) and S2 (459.7 PE) signals. Taken from [52].

details for each of these peaks: area in photoelectrons, number of PMT coincidences, position, and time width. A typical analysis involves searching for single scatter events above threshold, which leads to events with only a single S1 peak and a single S2 peak as candidates for dark matter particle interactions.

CHAPTER 3

XENON100 Data Analysis and Results

The latest XENON100 results in 2012 [103] follow a year after producing the world's best limits on WIMP detection in 2011 [69]. The new results for 225 live days of dark matter data taking offer improvements in trigger threshold, exposure, increased calibration statistics, and lower intrinsic background. This chapter details the calibration efforts and analysis procedures behind the limit published in 2012.

3.1 Calibrations

The XENON100 detector is designed to allow for three dimensional position reconstruction through TPC technology and to measure the energy deposition and characterize the type of particle from intrinsic radioactivity and/or dark matter. This requires calibrations from collimated sources and light sources for PMT gain measurements as well as gamma and neutron sources to characterize background and signal signatures.

3.1.1 Position Reconstruction

In a standard event, electrons drifted from the point of interaction produce a localized secondary scintillation signal from just above the liquid-gas interface on the top PMT array of the detector. The drift time, between the primary and secondary scintillation ($\Delta t = t_{S2} - t_{S1}$, see figure 2.8), defines the Z position due to the presence of a constant electric field and resulting constant drift velocity while the PMT pattern (figure 3.1) determines the XY position of the interaction.

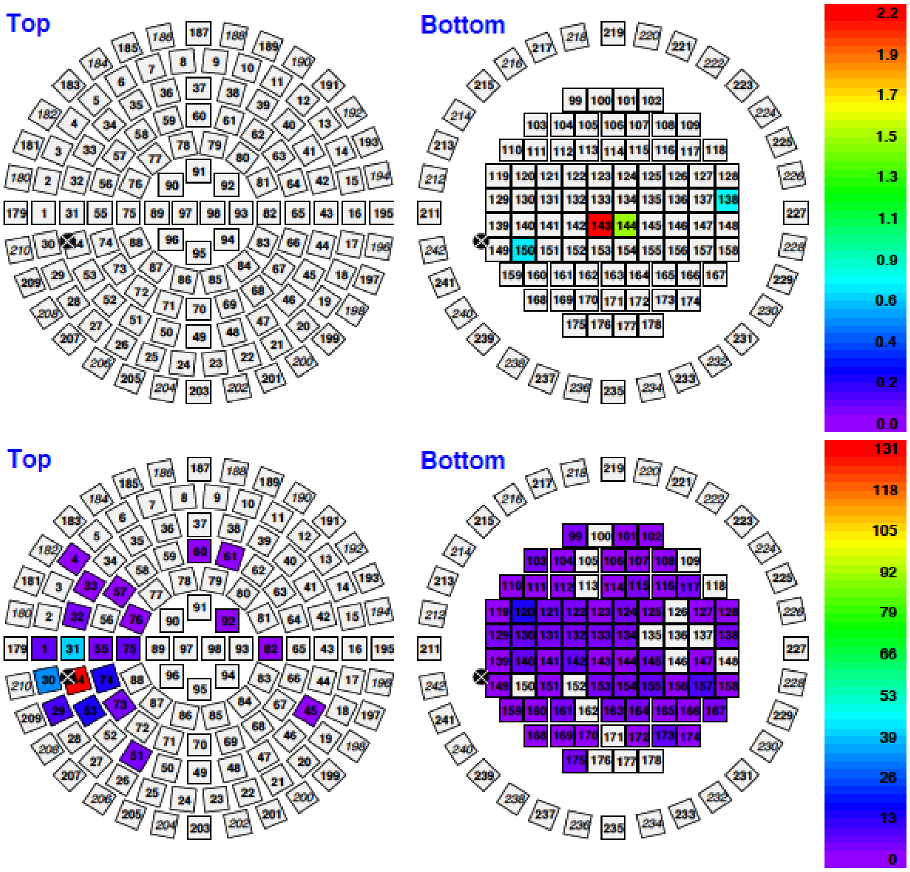

Figure 3.1: PMT patterns for both the S1 (*top*) and S2 (*bottom*) signals from which the XY position can be reconstructed from the low energy background gamma event shown in figure 2.8. Taken from [52].

Three position reconstruction algorithms, chi-squared, support vector machine (SVM) [104], and neural network (NN) [105], use the PMT pattern in comparison to one from a Monte Carlo generation to estimate the origin of the interaction. The chi-squared method minimizes the χ^2 value between data and simulation to find the position. SVM depends on training samples from the Monte Carlo to generate a base of vectors in a multidimensional space. The resulting position is found by solving for the scalar products between the input data vector and the base vectors of the training. Neural network, the reconstruction of choice for this analysis due to its homogeneity and agreement with simulation, uses a network of neurons with the full top PMT pattern as inputs and an underlying layer of 30 neurons trained on Monte Carlo data to produce the output position vector.

The position reconstruction algorithms have been tested by using a collimated ^{57}Co source placed above the TPC, which resulted in XY resolutions $<$3 mm for radii $<$ 142 mm. The Z resolution is limited by the width of the S2 signal to about 3 mm. This allows for external background reduction through the good self-shielding properties of liquid xenon (high Z).

3.1.2 Source Calibrations

The XENON100 calibration schedule consisted of weekly light, ^{137}Cs, ^{60}Co, and ^{232}Th source dedicated data taking runs. Additionally, before and after the dark matter data taking period, neutron calibrations were performed using an Americium-Beryllium (AmBe) source. The light calibrations record and normalize the PMT gains across the full array while checking for abnormal behavior. Data from the ^{137}Cs source is used to monitor the liquid xenon purity and corresponding electron lifetime to correct the S2 signal for lost electrons and for XY inhomogeneities in the signal on both PMT arrays. For this dark matter session, the electron lifetime ranged from 374 μs to 611 μs with an average of 514 μs.

The other source calibrations characterize the expected background electronic recoil distributions from 48 live days of ^{60}Co and ^{232}Th data taking, which produce a flat Compton scatters spectrum at lower energies in the liquid xenon. The distributions for both electronic recoils and nuclear recoils in the standard Log10(S2/S1) vs S1 phase space can be seen in figure 3.2, with the characteristic discrimination power inherent due to the quenching of nuclear recoil energy deposits along the Y axis.

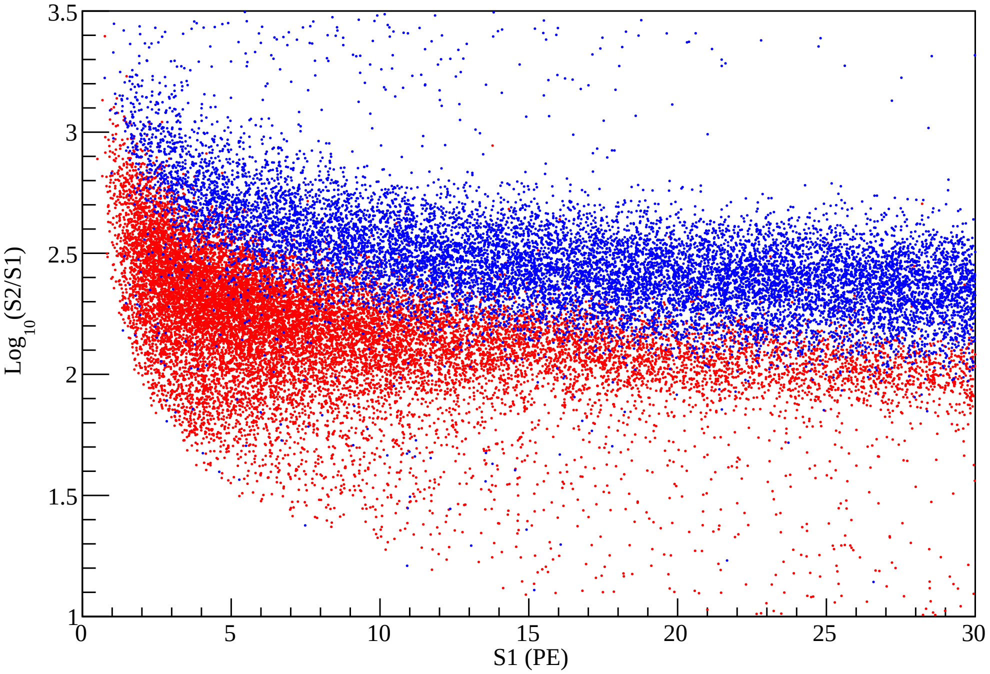

Figure 3.2: Calibrations from gamma data (*blue*) and neutron data (*red*) in the traditional phase space in the region of interest from 3-30 S1 PE after signal corrections for position dependence. Discrimination between the two types of recoils is provided by the log ratio of the secondary and primary scintillation signals (Section 2.1.4).

The AmBe calibration provides not only nuclear recoil data to model WIMP scatters, but also activated xenon lines (^{136m}Xe) and inelastic scattering lines (^{129m}Xe), which have a uniform position distribution and allow for measuring of the relative light yield for the primary scintillation within the TPC. The light yield depends highly on the position of interaction, ranging from solid angle effects to PTFE reflectivity and transmission of meshes. The light collection efficiency (LCE) map to correct for these effects was obtained from the inelastic 40 keV line, the lowest monoenergetic line available for calibration, as shown in figure 3.3. The light yield varies by a factor of three within the detector, with the highest light yield at the bottom middle ($Z = -300$ mm) of the detector to the lowest near the edges at the top ($Z = 0$ mm). The LCE map takes the reconstructed position of an event and modifies relative signal size such that the event occurred at the center of the detector, thereby normalizing over the full volume.

3.2 Analysis and Detector Behavior

In searching for WIMP dark matter, the principle is to retain as many single scatter nuclear recoil candidate events while rejecting the most background through the application of various software selection cuts. The most important selection criteria are the threshold cuts for both S1 and S2 and the single scatter selection. The S2 threshold cut is determined such that all events have a measured trigger efficiency of 100%. The S1 threshold, or coincidence cut, requires that the primary scintillation signal be recorded by more than one PMT over a time window of 50 ns. This aims to reject the many events produced by dark pulses or other spurious signals that are not associated with a true energy deposit. However, this also removes many of the low energy events, which only result in a single photoelectron observed by the PMTs.

We expect WIMPs to scatter only a single time in the detector due to the low

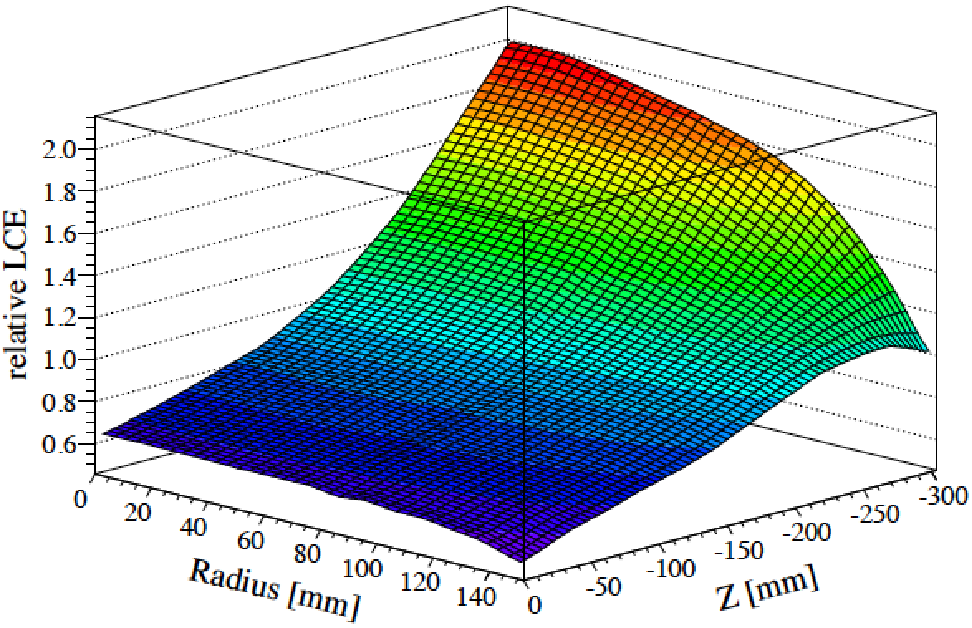

Figure 3.3: Position dependent relative light yield in the XENON100 detector obtained from the 40 keV inelastic scattering line, used to correct the primary scintillation signal relative to the center of the detector. The light collection map is axially symmetric as expected. Taken from [52].

predicted interaction cross section. Single scatter cuts discriminate the double scatter events through requirements of only a single S2 and a single S1. There is additional cut for the width of the secondary scintillation to remove gamma events and a host of quality cuts for the noisy signals and anomalous behavior.

The acceptance of these cuts was determined using nuclear recoil calibration data except for the quality cuts, which used dark matter data due to time-varying detector conditions. The resulting acceptance for the proposed WIMP signal due to these cuts and selection criteria can be seen in figure 3.4. The drop off at low energies in the acceptance curve is primarily due to the coincidence cut on the primary scintillation signal, which was obtained using data from vetoed signals to probe the lowest energies possible. In this analysis, the acceptance curve for the S2 threshold cut is applied to the WIMP spectrum before any poisson smearing of the S1 signal.

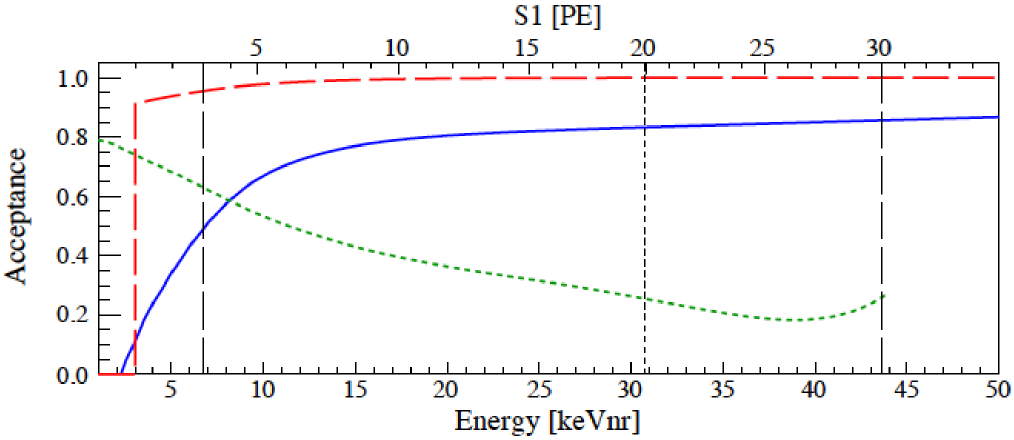

Figure 3.4: The total acceptance for all cuts with the exception of the S2 threshold cut is seen in *blue*. The *red* dashed line signifies the acceptance for the S2 threshold cut, which is applied before smearing of the S1 signal. The *green* dotted line shows the acceptance of a 99.75% cut on the discrimination parameter, Log(S2/S1), which decreases with energy due to loss of discrimination power. The axes are shown in both S1 photoelectrons and the deposited nuclear recoil energy obtained from conversion using a maximum likelihood fit to $\mathcal{L}_{eff}$. Taken from [103].

The analyses performed include a standard analysis using a hard cut on the rejection parameter as well as a profile likelihood analysis which takes advantage of the full phase space. The hard cut for the rejection parameter is determined from gamma calibration data for a stated background rejection level of 99.75% across the full region of interest (3-20 PE or 6.6-30.5 $\mathrm{keV_r}$). The profile likelihood analysis incorporates systematic uncertainties due to the energy scale ($\mathcal{L}_{eff}$) and variations across simulated experiments while scanning over a larger region (3-30

PE or 6.6-43.3 $\mathrm{keV_r}$). In slicing the parameter space, $\mathrm{Log_{10}}$(S2/S1) vs S1, probabilities for both signal (neutron distribution, weighted in S1 by the expected WIMP energy spectrum) and background from the gamma calibration data are obtained and input into a likelihood analysis with nuisance parameters and a parameter of interest, the cross section or number of signal events. This allows for an expected sensitivity to be inferred using Monte Carlo generation of pseudoexperiments as well as a 90% CL upper limit from the dark matter dataset or any significant discovery reach of the experiment.

To limit any analysis bias, a blinding cut is applied to the dark matter dataset for the signal region defined in the standard analysis. The raw exposure was reduced through removal of periods with increased electronic noise, large temperature or pressure fluctuations, and very localized light emission on the top PMT array giving the final exposure of 224.6 days.

3.2.1 Expected Background

The expected gamma background for the data taking run is determined both from the distribution of gamma calibration data from ^{60}Co and ^{232}Th scaled to the runtime exposure of 224.6 days and 34 kg and Monte Carlo simulations of anomalous events from below the cathode, the gamma-X events. This resulted in an expectation of 0.79±0.16 events in the signal region. Simulations of neutron production from (α,n) and spontaneous fission using SOURCES using the results from intrinsic radioactivity screenings (30%) and muon-induced neutron generation (70%) contributed to $0.17^{+0.12}_{-0.07}$ neutron events in the benchmark region, leading to a total background expectation of (1.0±0.2) events.

In addition to the low energies of the signal region, the electromagnetic background has also been studied up to the major gamma peaks around 2600 keV for

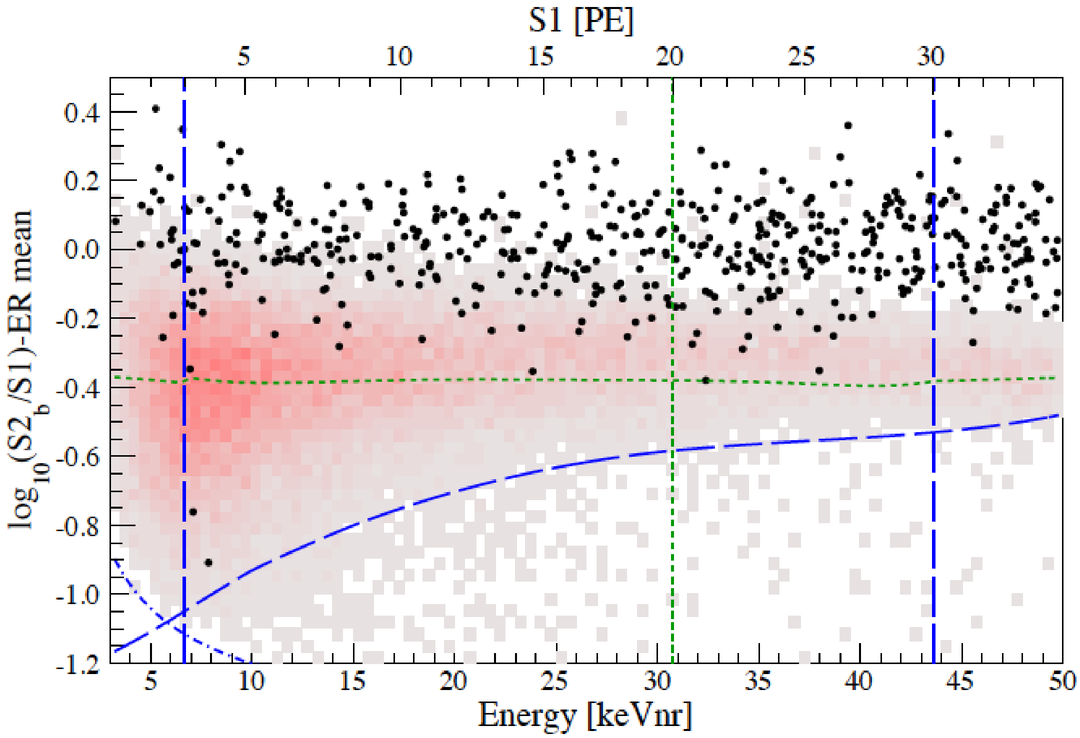

Figure 3.5: Event distribution for the 224.6 day exposure for data taken in 2011-2012 represented by the *black* points in the flattened $\text{Log}_{10}(\text{S2}_b/\text{S1})$ vs S1 (energy) phase space obtained by subtracting the fitted mean for the electronic recoil band. In the background is the neutron distribution obtained from AmBe calibration data. The *green* horizontal dotted line is the 99.75% gamma background rejection line determined from gamma calibration data. The *blue* line at the bottom is for the 3σ neutron recoil band. The energy region of interest is from 3-30 PE (6.6-43.3 keV_r) for the profile likelihood analysis. Taken from [103].

this run (similar to previous analyses [98]). Figure 3.6 shows the comparison of Monte Carlo simulations using input screening values (section 2.4) for all detector materials and internal detector impurities to the spectrum obtained from data for a 10 kg fiducial volume to reduce errors in position reconstruction due to PMT saturation. The energy scale for these recoils is determined from a combination of the S1 and S2 signals from the inherent anti-correlation of the two channels for monoenergetic gamma lines, the lowest of which is from 40 keV$_r$ inelastic scattering.

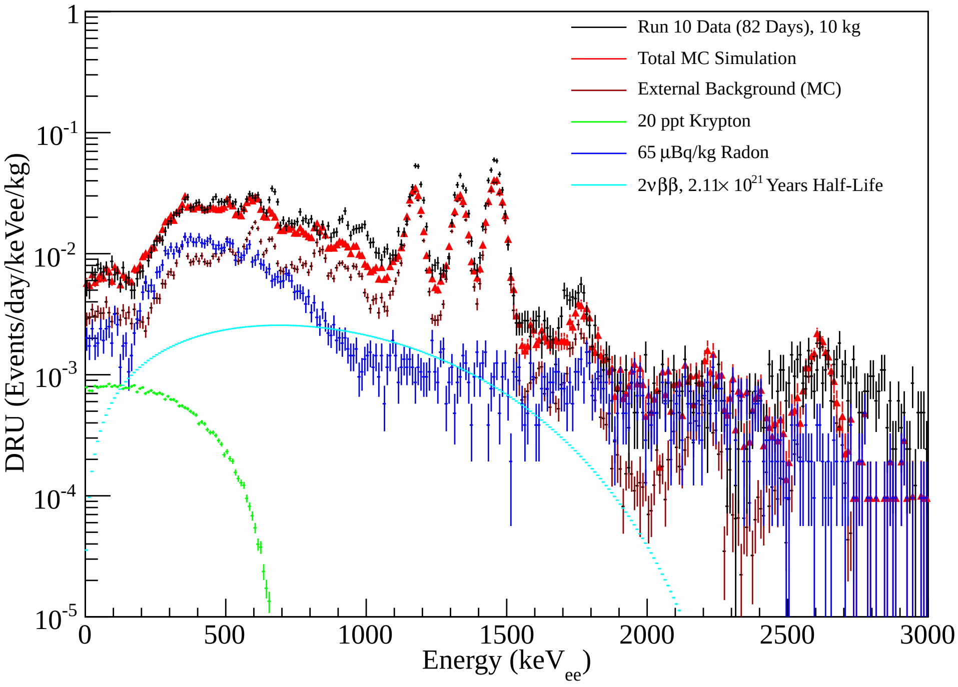

Figure 3.6: Differential background energy spectrum of the XENON100 data from the most recent run for a 10 kg fiducial volume without veto selection. A small fiducial volume is used to reduce the systematic effects of poor position reconstruction due to photomultiplier tube saturation for large S2 signals. The energy resolution applied to the Monte Carlo is obtained from measurements of the widths of the gamma lines in the data spectrum.

This comparison demonstrates detector understanding far outside the signal region (about 1-10 keV$_{ee}$) of the contributions of individual sources to the total electronic recoil background. Radon in the liquid xenon volume accounts for about half the low energy background and is not reduced effectively by fiducialization; this poses one of the challenges for next generation ton-scale detectors.

3.3 Run10 Results

The results after all the analysis cuts and unblinding can be seen in figures 3.5 and 3.7 for flattened $\mathrm{Log}_{10}(\mathrm{S2}_b/\mathrm{S1})$ vs S1 and the spatial distributions. The flattened variable for only the bottom S2 signal has been chosen due to better homogeneity of the signal over the PMT array reducing the effects of saturation. In the region of interest, two events were found at 3.3 PE (7.1 $\mathrm{keV_r}$) and 3.8 PE (7.8 $\mathrm{keV_r}$) and appear at the lower values of the discrimination parameter. This distribution suggests the presence of an underlying background not considered previously, as these events are unlikely to be either gamma background (such as multiple scintillation single ionization events) or signal events. Further investigation after unblinding has tended to attribute these events to a population below the S2 threshold, but the results are inconclusive. The spatial reconstruction of these events places them near the outer fiducial region, but still well within the volume designated. The waveforms are of high quality and are both kept for the statistical analysis.

Both the profile likelihood, which yields a p-value of $\geq$5% for all WIMP masses for the background-only hypothesis, and poisson probabilities, whereby a single background event fluctuates to two events (26.4%), suggest the lack of an excess due to a dark matter signal. For the standard isothermal WIMP halo model with density $\rho_\chi = 0.3$ GeV/c^3, local circular velocity $v_0 = 220$ km/s and a galactic escape velocity $v_{esc} = 544$ km/s, a 90% confidence level exclusion limit for spin-independent cross sections, σ_χ of the WIMP-nucleon interaction is calculated using the profile likelihood method.

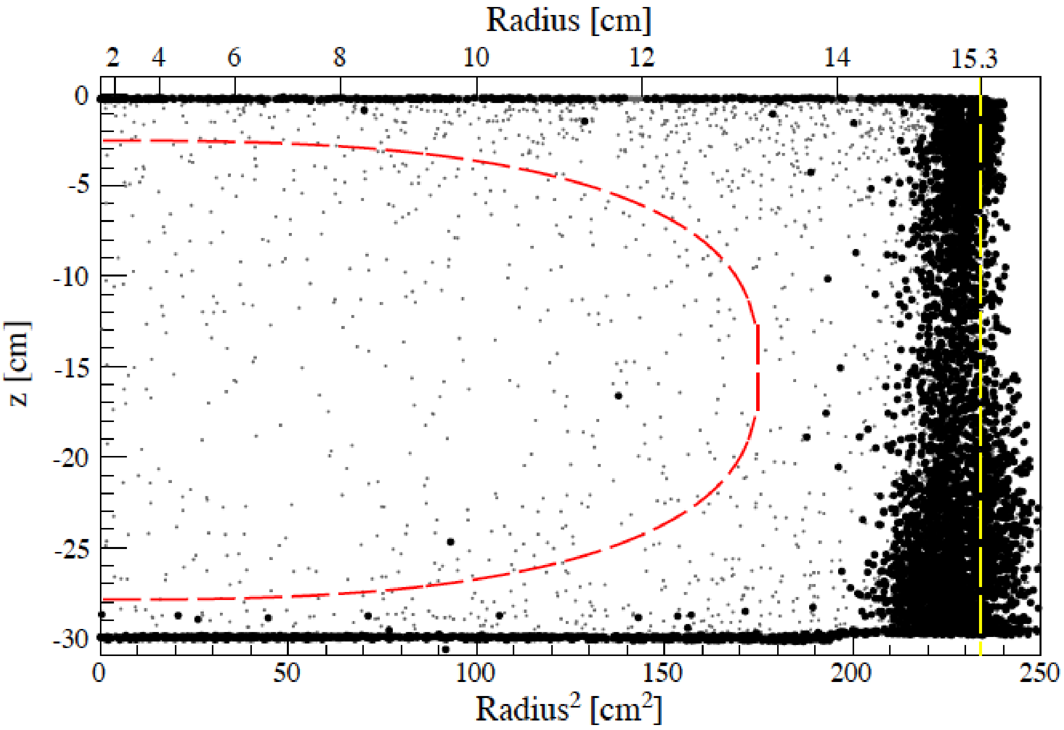

Figure 3.7: Spatial distribution of events in the energy region of interest (6.6-43.3 keV$_\mathrm{r}$). *Black* points are events that fall below the 99.75% rejection line while *gray* points are for the full phase space. The 34 kg fiducial volume is inside the red dashed line. Taken from [103].

The results of the profile likelihood statistical analysis are shown in figure 3.8 and provide the most stringent limit for masses greater than 8 GeV/c^2 with a minimum at σ=2.0 × 10^{-45}cm^2 at a WIMP mass of 55 GeV/c^2. The upper limit below 8 GeV/c^2 further excludes the interpretations of DAMA, CoGeNT, and CRESST-II results as evidence for scalar dark matter interactions.

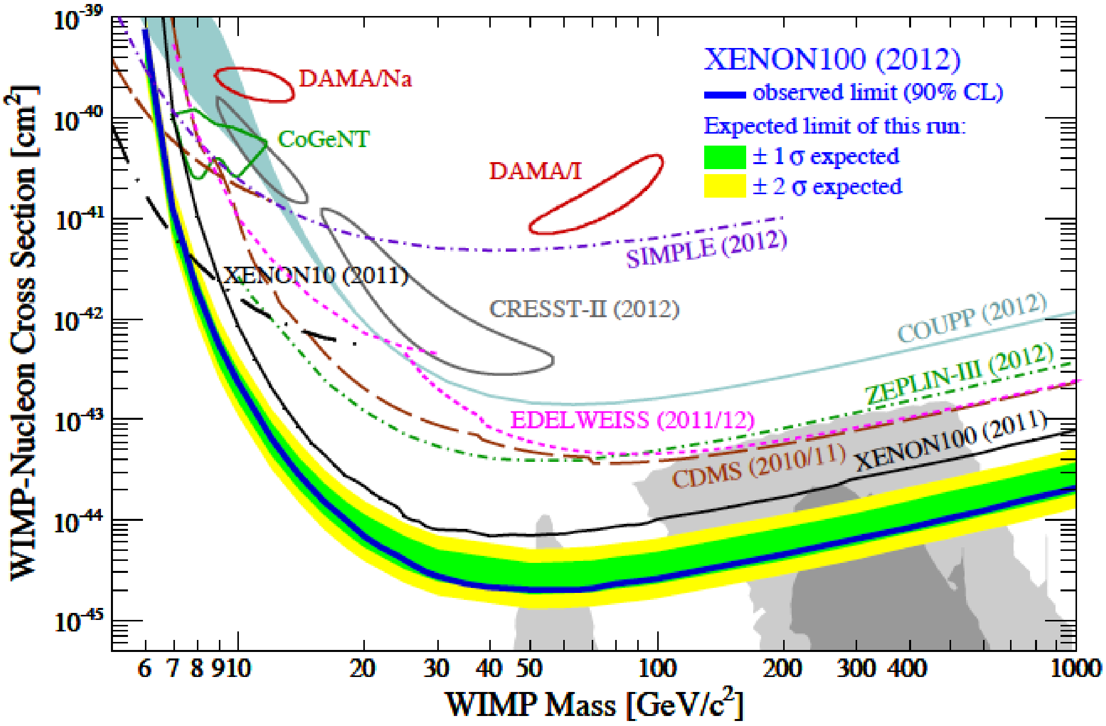

Figure 3.8: Result from the latest XENON100 dark matter data taking run. The expected sensitivity of the run obtained from the profile likelihood approach is shown by the green/yellow bands ($1\sigma/2\sigma$). The 90% CL upper limit from the data set is given by the blue curve. Previous upper limits from other experimental results are shown as is the preferred parameter space of CMSSM models. Taken from [103].

CHAPTER 4

Two Dimensional Analysis Method for Noble Liquid Detectors

Traditionally, the standard two-phase liquid xenon analysis has been to use the primary scintillation signal (S1) as the energy estimator, while the secondary scintillation (S2) provides the means for discrimination between background and signal using a ratio of the two. Due to statistical fluctations present in S1 signal production and detection, this channel has the inherent effects of poor energy resolution and energy reconstruction at threshold. Additionally, the coincidence requirement among multiple PMTs results in a high self-imposed analysis energy threshold. The signal model for this analysis incorporates only spectral information for the S1 signal, using the AmBe calibration data signature along the $\mathrm{Log}_{10}(\mathrm{S2}/\mathrm{S1})$ variable. For setting limits on WIMP-nucleon cross sections where no signal is observed, this analysis is sufficient. However, the change to using the S2 signal as the variable of interest for energy estimation greatly enhances the power of a spectral analysis especially in the event of a WIMP discovery.

This new method for analysis [106] maintains the advantages of the traditional analysis i.e. three dimensional position reconstruction and particle discrimination, but allows for the freedom of spectral analysis of potential signal events due to improved energy determination and energy resolution near the energy threshold. The basis for these improvements lies in the larger absolute yield of signal quanta available to the ionization channel of detection. The remaining caveat to this discussion is the uncertainty in the underlying energy scale for the ionization channel, which has only a handful of external measurements. The method shown here is a general analysis technique applicable for noble liquid detectors and uses approximate input variables only for illustration.

Chapter 5 details the indirect determination of the conversion from ionization signal to recoil energy using an absolute comparison between simulation and nuclear recoil calibration data. This conversion is useful for extending simulations of WIMP signals to the ionization channel for use in a profile likelihood analysis of XENON100 data as in Chapter 6.

4.1 Nuclear Recoil Energy Conversions

The energy deposited by an interaction in the liquid xenon target volume can be measured using either the primary scintillation signal (S1) or the ionization or secondary scintillation signal (S2). Just following the interaction, the xenon atoms are in both excited and ionized states as shown in figure 4.1 (recall equations 2.2 and 2.3, which detail the initial scintillation process of ultraviolet photons response for the S1 signal). In the presence of an electric field, some of the ionized electrons become free and drift to the liquid/gas interface, where they produce a secondary light signal through electroluminesence in the gas phase (S2) while the rest recombine into excited states and emit scintillation light as part of the S1.

The S1 signal produced in an interaction encounters several difficulties at low energy in both detection and energy determination. The S1 signal is small due to yield per $\mathrm{keV_r}$ being only a fraction of a photoelectron at low energies resulting in large statistical fluctuations. Theoretical models and direct measurements of $\mathcal{L}_{eff}$

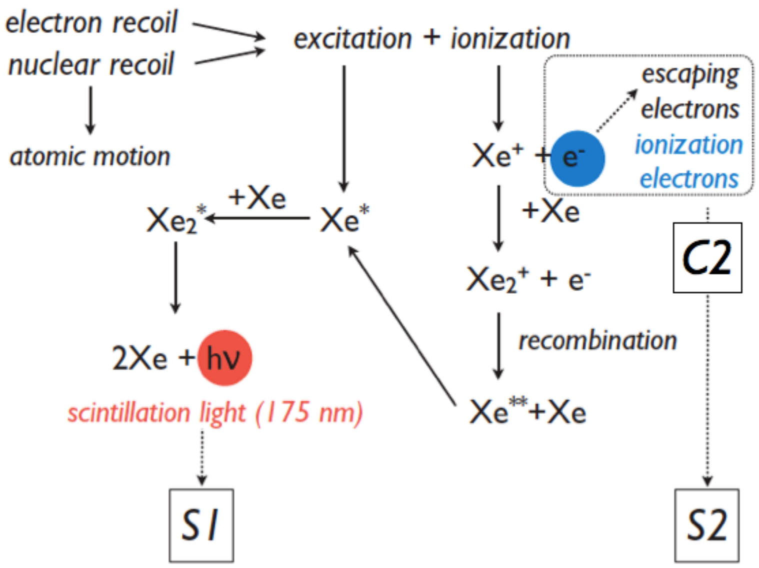

Figure 4.1: Diagram for the mechanism behind the production of S1 and S2 scintillation signals in liquid xenon detectors. Taken with slight modifications from [90].

predict or indicate a drop off at lower energies as in figure 4.2, resulting in poor energy measurement due to low statistics. Additionally, recalling equation 2.5, reproduced here

$$E_{nr} = \frac{\mathrm{S1}}{\mathcal{L}_{\mathcal{Y}}(122\mathrm{keV}_{\mathrm{ee}})} \frac{1}{\mathcal{L}_{eff}(E_{nr})} \frac{S_{ee}}{S_{nr}}$$

shows that even with existing measurements for the relative scintillation efficiency there requires several steps before conversion to the energy from the scintillation signal. Traditionally, the absolute calibration point for the $\mathcal{L}_{\mathcal{Y}}$ is measured relative to 122 $\mathrm{keV}_{\mathrm{ee}}$ while additional corrections are required for the field dependent response to both gamma rays and neutrons (S_{ee} and S_{nr}). The last step is including the energy dependence of the relative scintillation yield from $\mathcal{L}_{eff}$. This conversion as a piece by piece calibration propagates large systematic errors at each stage as opposed to calibrations performed directly with the detector, which cancel out systematic errors.

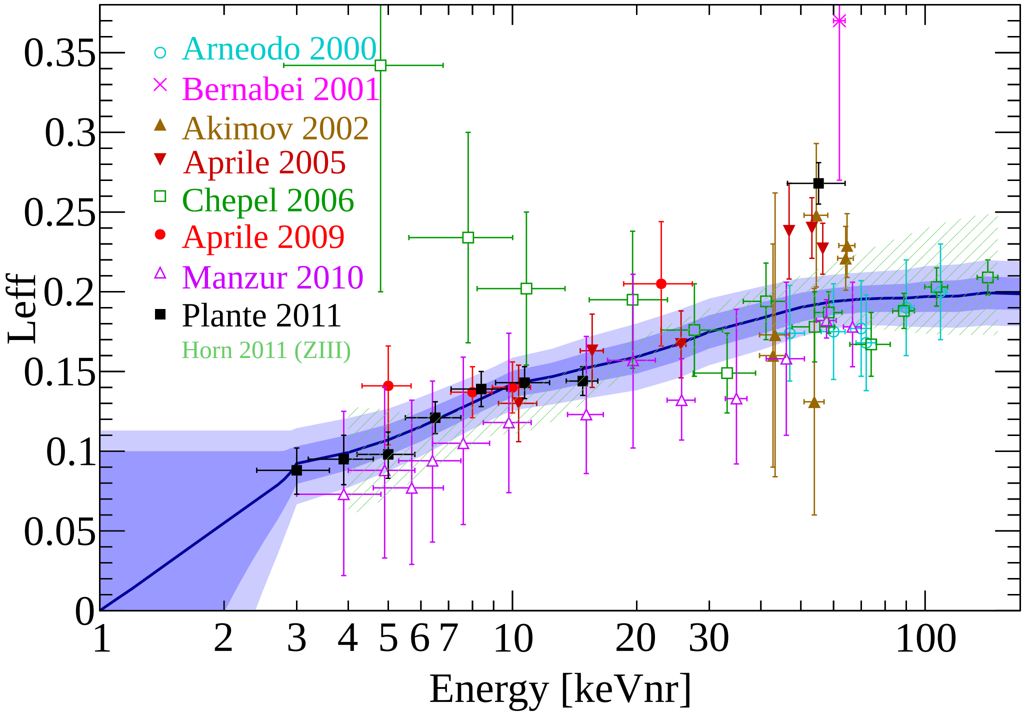

Figure 4.2: Relative scintillation yield from direct (*points*) and indirect (*hatched*) measurements. The $\mathcal{L}_{eff}$ parameterization used for this study (*black*) is the maximum likelihood fit to all the measurements with a smooth decrease to 0 at 1 keV_r.

The S2 signal, on the other hand, originates from the field extraction and drift, which gives a much larger quantity of measurable quanta than for the S1 signal. Typically, the yield is on the order of 100 photoelectrons per $\mathrm{keV_r}$ as opposed to the fraction of a photoelectron per $\mathrm{keV_r}$ for the S1 and does not decrease quickly at low energies. The conversion from the S2 signal to energy (equation 2.6)

$$E_{nr} = \frac{\mathrm{S2}}{\mathcal{Q}_y \alpha_{se}}$$

depends only on the ionization yield, $\mathcal{Q}_y$, and the detector-dependent quantity α_{se}, the secondary scintillation gain achieved through electroluminescence.

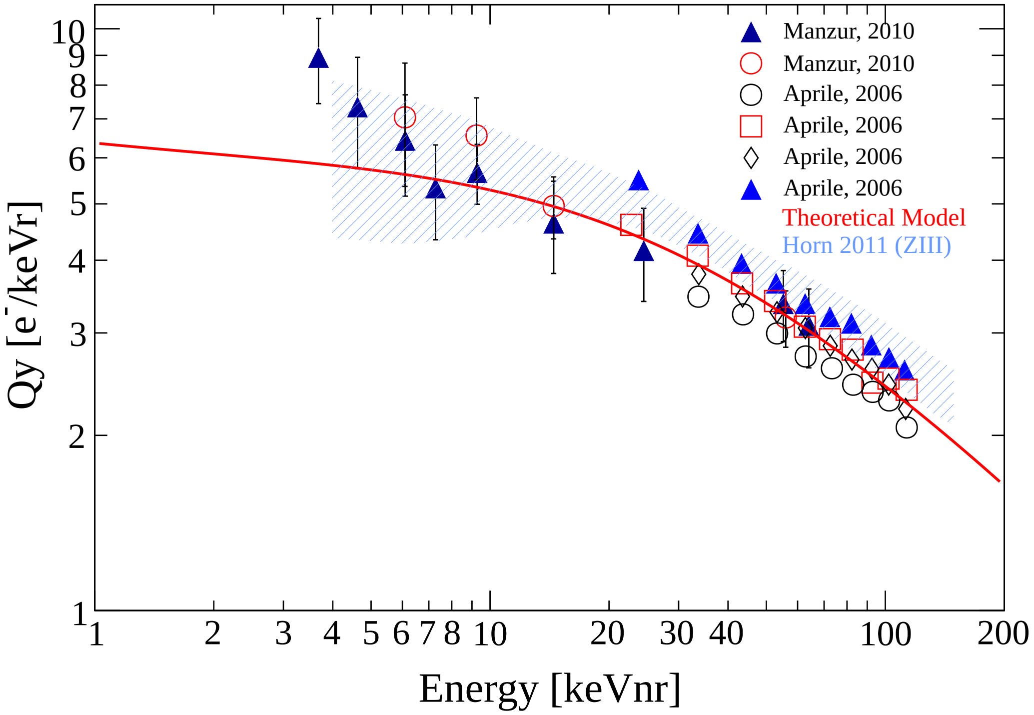

Figure 4.3: Reproduction of figure 2.2 with the addition of the parameterization (*red*) from a theoretical model using Thomas-Imel recombination and the Ziegler stopping power.

4.2 Generic Model for the S1 and S2 signals

The advantages gained by using the S2 instead of the S1 signal as the parameter of interest are best illustrated using a simple detector model and relevant simulations. The model uses the maximum likelihood fit to all measurements of $\mathcal{L}_{eff}$ as parameterized in figure 4.2 and a theoretical ionization yield derived using the universal stopping power from Ziegler et al [107] and the recombination model from Thomas-Imel [81] as shown in figure 4.3.

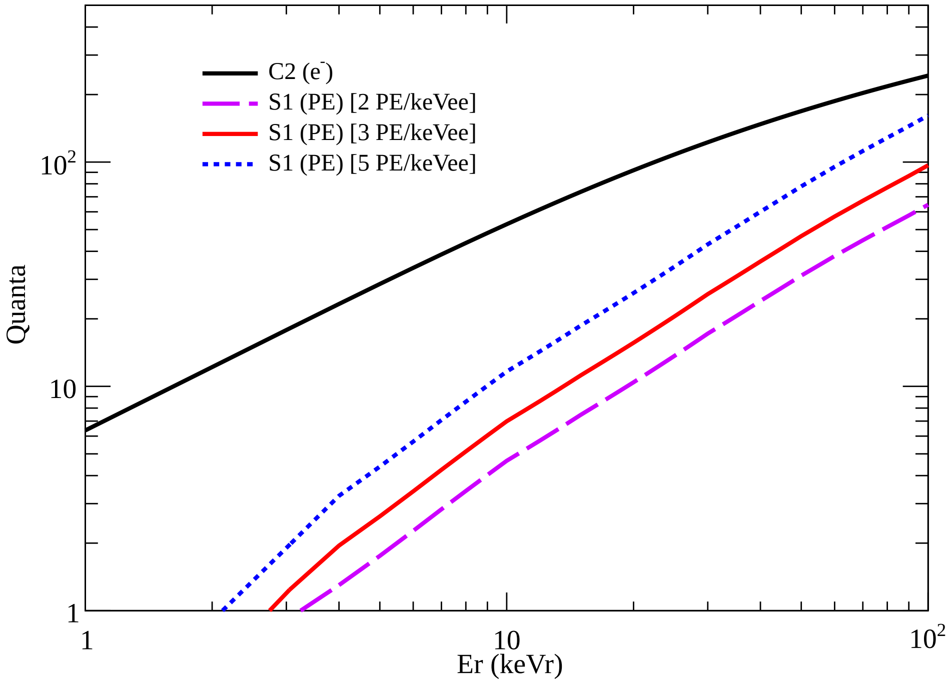

Figure 4.4: Absolute quanta for S1 for three light yields and for C2 (before gas amplification). The S1 is in units of photoelectrons and C2 is in units of electrons. Modified from [106].

The other parameter assumptions to be used are $\mathcal{L}_y(122\mathrm{keV_{ee}}) = 3\ \mathrm{PE/keV_{ee}}$, electric field dependent S_{nr} and S_{ee} are chosen for an electric field of 0.5 kV/cm, and the gas gain with a mean, α=20 PE/electron. The S1 and S2 signals are modeled using Poisson distributions for the number of photoelectrons and number of electrons freed in the initial interaction, respectively. These underlying Poisson fluctuations in the modeling is the largest source of uncertainty regarding the measurement of the energy of an interaction. For ease of quanta comparison, the charge signal (C2) is denoted by, C2 = S2/α_{se}.

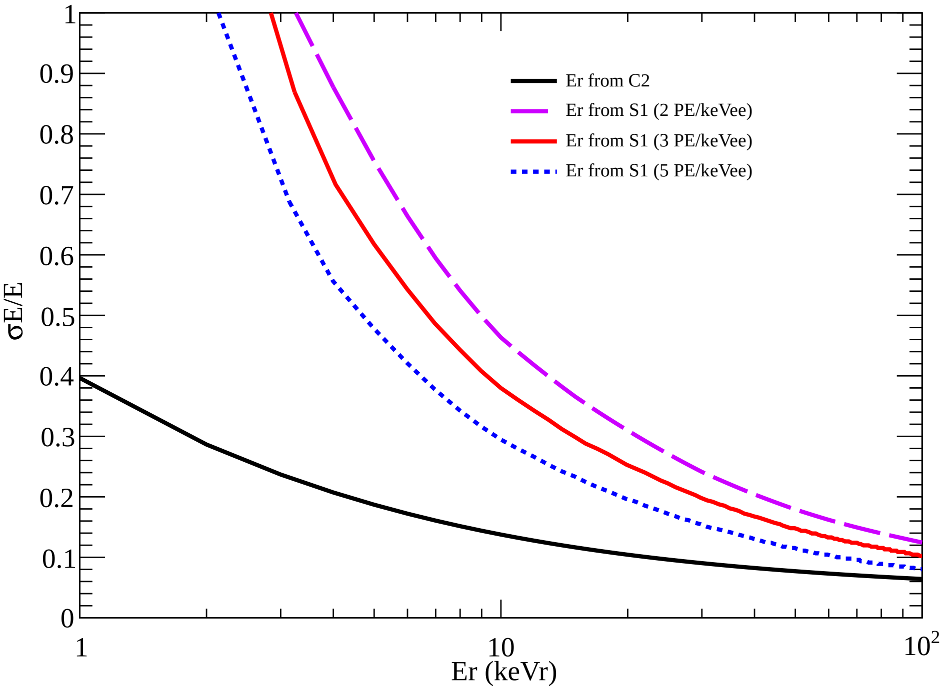

Figure 4.5: Energy resolution of the S1 and C2 signals as a function of the energy in keV$_r$. For energies above 50 keV$_r$, the resolutions to each channel become comparable, but below the improvement available to the ionization channel is increasingly evident. Modified from [106].

Using this model and assumptions, we can compare the potential of each channel to measure an energy deposition. Figures 4.4 and 4.5 show the increasing effectiveness of C2 (or S2) at lower energies due to the larger amount of signal as compared to S1. This difference in signal size allows for resolution of less than 20% down to about 3 keV$_r$ for the C2 signal while the resolution from S1 is about 50% and higher at less than 7 keV$_r$.

4.3 Two Dimensional Phase Spaces

The difference between estimating the energy deposition from S1 and C2 is evident in looking at two phase spaces: the standard Log_{10}(S2/S1) versus S1 and the new Log_{10}(S1/S2) versus S2. A third phase space of Log_{10}(E1/E2) versus E2 is notable for its detector independence as all quantities have been converted to energy, while the mean of the signal distribution is set to zero ($\text{Log}_{10}(\text{E1}/\text{E2}) = 0$) by construction. This latter distribution is presented only for illustration, however, as the profile likelihood analysis performed in Chapter 6 uses the S2 phase space due to ease of analysis. Because S1 and S2 have one to one relationships with both E1 and E2 through $\mathcal{L}_{eff}$ and $\mathcal{Q}_y$, all of these phase spaces are equivalent through simple transformations.

4.3.1 Injection of Monoenergetic Signals

A method to illustrate advantages of the S2 energy estimator is to simulate monoenergetic signals at several nuclear recoil energies, namely 4, 8 16, and 32 keV_r. In the next chapter, this simulation is extended to a continuum of energies of typical neutron calibration sources like AmBe or ^{252}Cf.

Figure 4.7 shows the traditional phase space for injecting monoenergetic nuclear recoils. The individual distributions are distorted along the lines of constant E1 and E2 in slanted elliptical fashion. The proportion of the distortion along the S1 axis makes it difficult to reconstruct the energy of individual events using the S1 signal.

In figure 4.7, the monoenergetic distributions for the Log_{10}(S1/S2) versus S2 phase space are again elliptical but aligned more vertically than in the traditional phase space. This reduces the ambiguity in the conversion between the nuclear

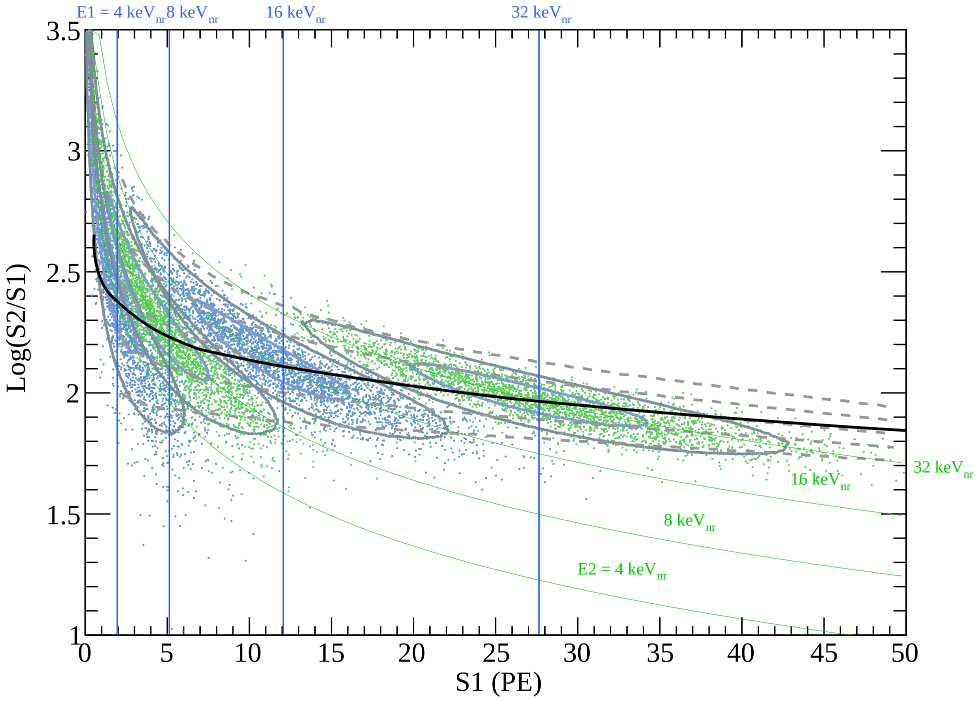

Figure 4.6: Monoenergetic energy distributions for the Log_{10}(S2/S1) versus S1 phase space for recoil energies of 4, 8, 16, and 32 keV$_r$. The overlap in energies demonstrates the inability of the S1 to represent the true energy of an event on an event-by-event basis. The monoenergetic lines for energies derived from both S1 (*blue*) and S2 (*green*) are plotted as well. Contours of the distributions are given by the *gray* dashed lines.

recoil energy and the signal observable. Additionally, the Y-axis still provides a measure of discrimination. The background distribution in this new phase space is presented in Chapter 6 and demonstrates the power of using the S2 variable as the parameter of interest as additional discrimination originates from the spectral shape. This provides the most important advantage in the possibility of the hint of a discovery of a WIMP particle and the characteristic exponentially falling energy spectrum, which is easily discernible using the S2 as the energy estimator.

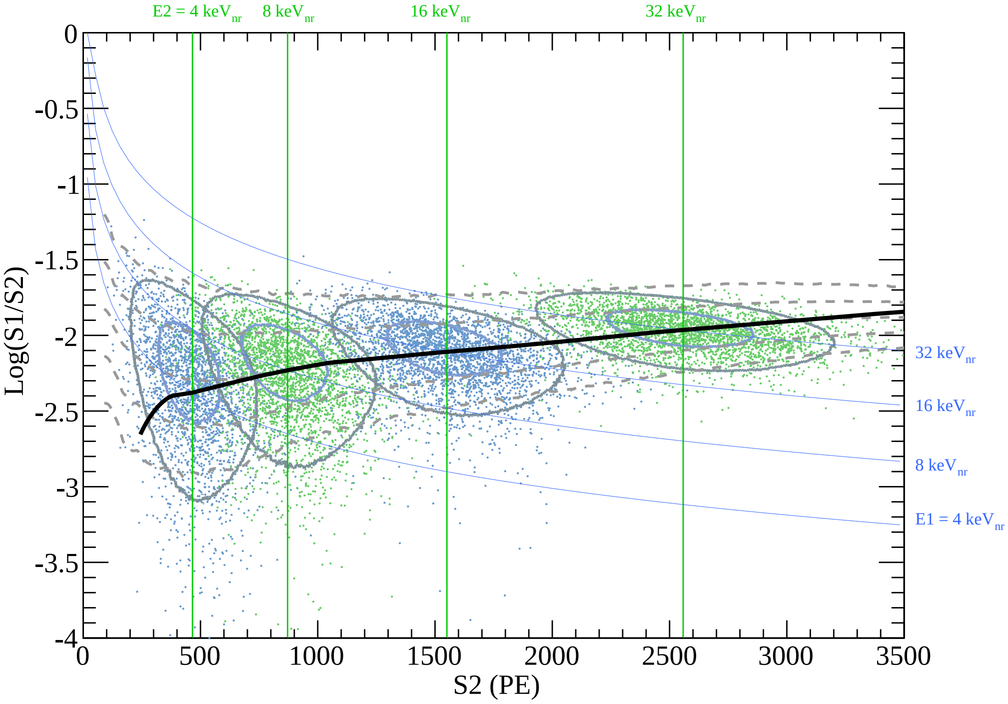

Figure 4.7: Monoenergetic energy distributions for the $\text{Log}_{10}(\text{S1/S1})$ versus S2 phase space. In comparison to the traditional phase space, the uncertainty on the energy of an event is reduced significantly without sacrificing discrimination power.

4.3.2 Signal Region Definition

The traditional signal region is characterized by boundaries of constant S1 and the lower portion of the nuclear recoil event distribution from the mean to lower 2σ in the $\text{Log}_{10}(\text{S2/S1})$ versus S1 phase space. An example of this region is shown in figure 4.8, where the high energy bound of 32 keV$_r$ only contains a small fraction of the actual 32 keV$_r$ events. Similarly at low energies, the effects of S1 Poisson smearing are evident as some events from below threshold may appear in the signal region and allows for some detector sensitivity to lower energy scatters.

Due to the poor energy estimation afforded to the S1 channel, the traditional signal region using boundaries of constant S1 is undesirable. A new signal box using the same energy bounds from 4 to 32 keV$_r$ but with constant S2 instead, due to its improved energy resolution and energy determination (the 4 keV$_r$ threshold denotes the lowest energy direct measurement of the ionization yield). The lowered energy threshold takes advantage of signals down to 2 PE in S1 (with detector efficiencies losses parameterized). This signal region in both phase spaces is shown in figure 4.9 and demonstrates the improved acceptance of low and high energy nuclear recoils.

Aside from these two signal box parameterizations, the ideal signal region consists of the full phase space down to the lowest energies above trigger threshold. This requires a statistical analysis that characterizes signal and background effectively especially in regions with a high background content, and improved knowledge of the conversions between observable and recoil energy. The latter is realized through comparison of Monte Carlo and neutron calibration data to understand the relative scintillation yield and ionization yields for liquid xenon (Chapter 5) to the lowest energies possible and the former is addressed by a profile likelihood analysis (Chapter 6), which takes into account the distribution of signal and background over the entire region of interest.

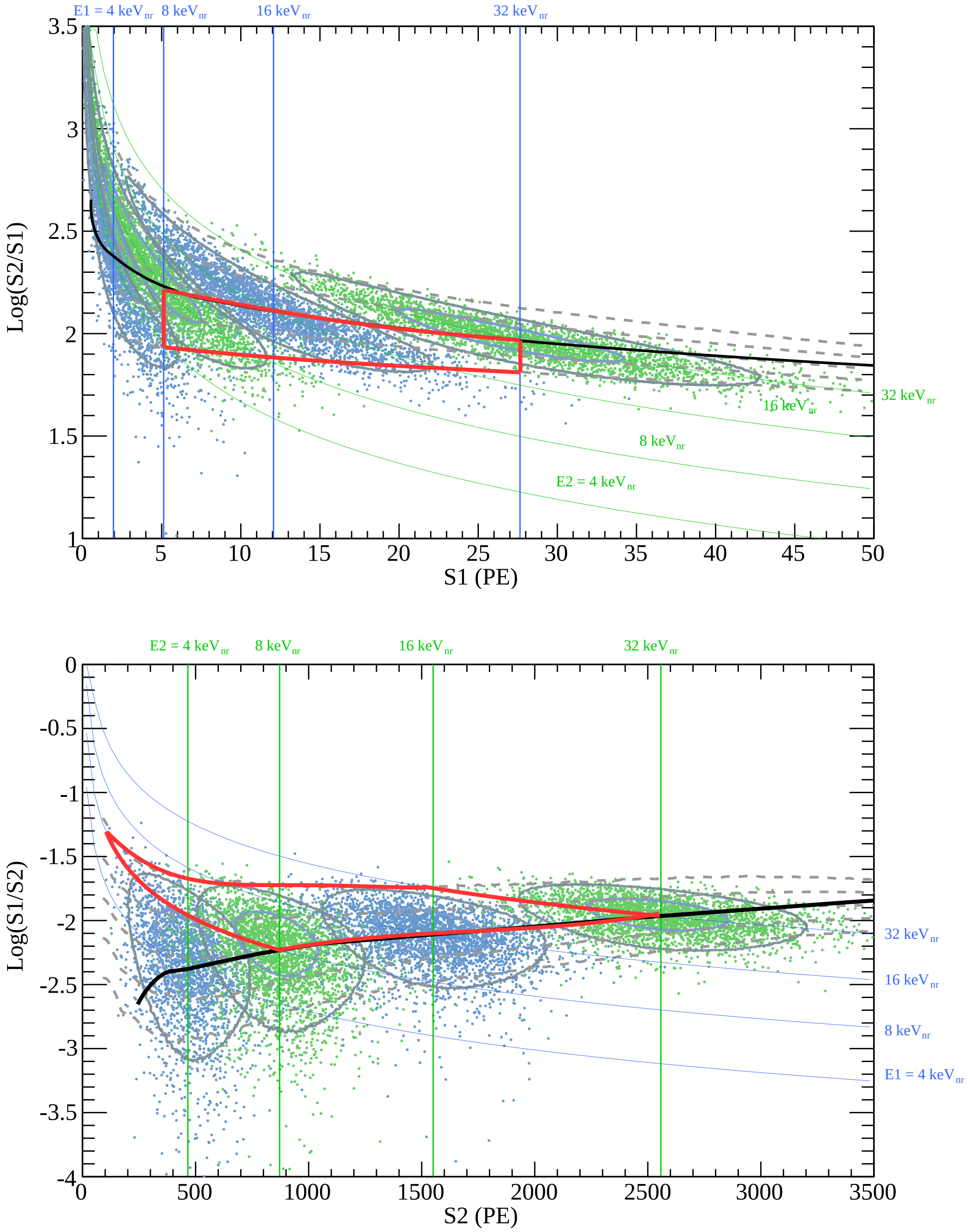

Figure 4.8: Traditional signal region definition in both Log$_{10}$(S2/S1) versus S1 (*top*) and Log$_{10}$(S1/S1) versus S2 (*bottom*) phase spaces. The bounds imposed are poorly defined in energy as many events from above and below the energy range may appear in the region due to Poisson smearing effects.

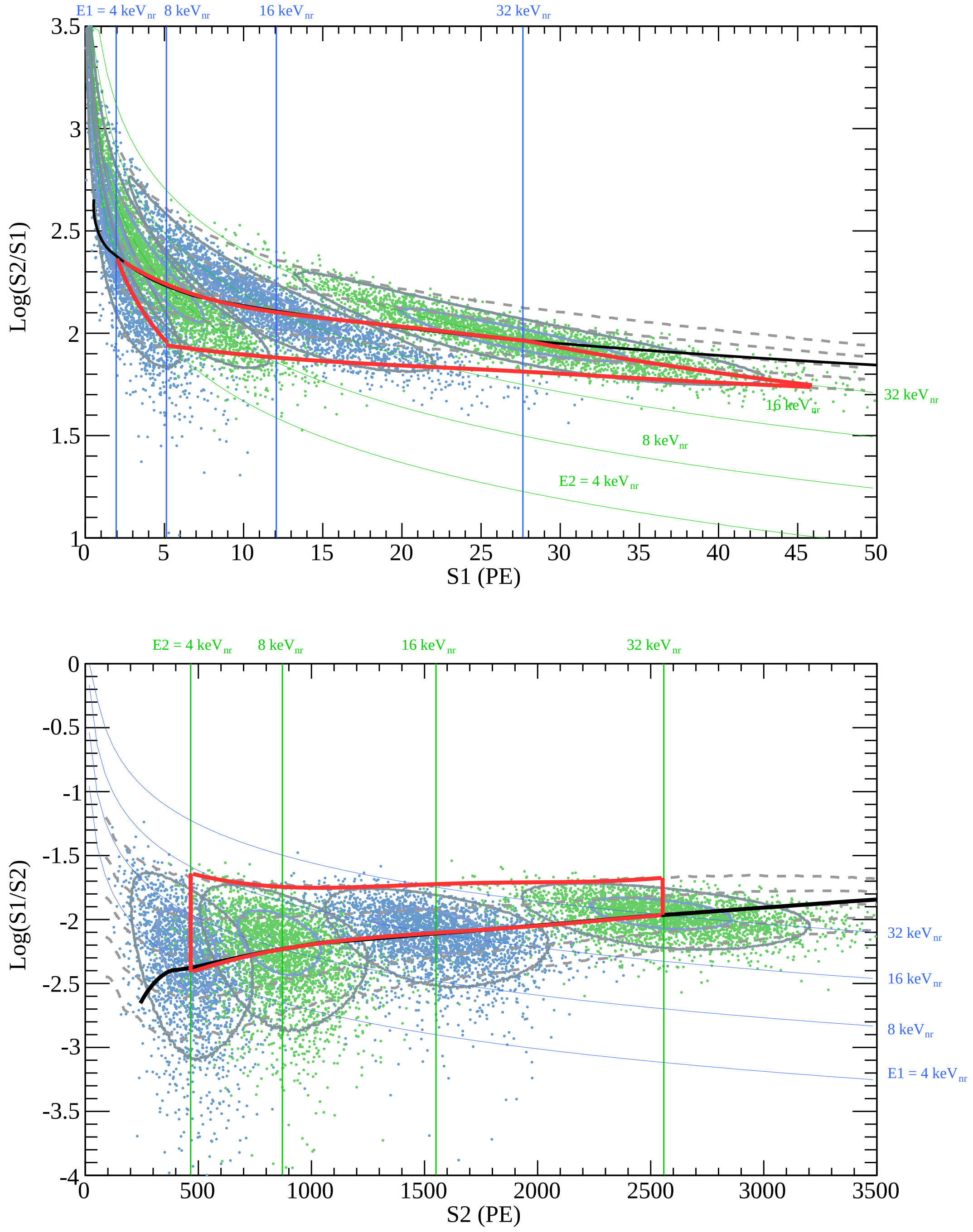

Figure 4.9: New signal region definition in both Log$_{10}$(S2/S1) versus S1 (*top*) and Log$_{10}$(S1/S1) versus S2 (*bottom*) phase spaces.

CHAPTER 5

Determination of the Ionization Yield and Relative Scintillation Yield from XENON100 Data

Moving to the Log_{10}(S1/S2) versus S2 phase space and employing a new WIMP model for analysis requires the knowledge of the nuclear recoil energy scales in liquid xenon. The primary scintillation (S1) scale is determined by the relative scintillation yield inferred from direct measurements in dedicated experimental setups [90, 91]. The energy of an ionization signal (S2) is similarly defined by the ionization yield but has only a few direct measurements [87, 90]. Modeling the detector and simulating interactions in the liquid xenon allows for the extraction of the ionization yield indirectly by comparing Monte Carlo data to neutron calibration data in lieu of an *in situ* measurement, which will be used in the future.

This extraction is performed by a minimization procedure consisting of a non-linear least squares method and a varying spline interpolation for the ionization yield to obtain the best fit result for the given inputs: detector efficiencies, the scintillation energy scale, and the simulation geometry and data. The systematic effects of the inputs upon the ionization yield are considered as well. The extracted yield and associated systematics are necessary for creating the WIMP model for statistical analyses (Chapter 6).

5.1 XENON100 Neutron Simulation

The Monte Carlo simulation used to generate nuclear recoils is a combination of a Geant4 [108] geometry and simulation package with particle generation and energy deposits, and an analytical addition, which includes the conversion from energy to detector observable, inherent fluctuations of signal, and detector acceptances and efficiencies.

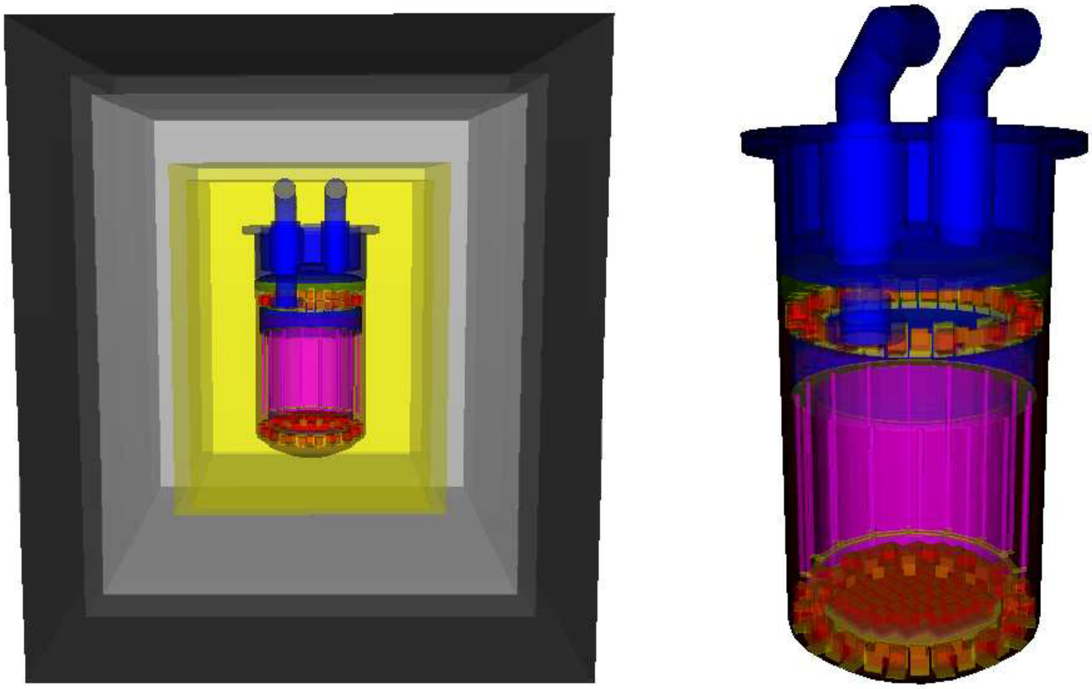

Figure 5.1: Schematic of the XENON100 detector geometry as visualized in Geant4. *Left:* Shielding enclosure and cryostat and *Right:* Time Projection Chamber allow for Monte Carlo simulations using the true dimensions of the detector.

5.1.1 Geant4 Simulation

The XENON100 detector geometry (figure 5.1) modeled in Geant4.9.3.p02 consists of the shielding materials and TPC. The physics package for neutron scatters uses neutron cross sections from the ENDF/B-VI library [109]. A pointlike neutron source, with an input energy spectrum from Americium Beryllium decays (ISO 8529-1 (2001), figure 5.2 [110]), is placed in an external lead brick to reduce gamma flux as it is in the real experiment. Using the G4NDL3.13 package, only elastic scatters from nuclear recoils in the liquid xenon are recorded and grouped using a range cut of 0.5 mm. Following the initial Geant4 generation of 27 million neutron events and subsequent clustering of scatters, a resolution of 3 mm in the Z-direction is applied to model the detector response [52], such that events occurring within this length are summed in energy and energy-weighted in position.

The final Geant4 data sample contains events with one or more nuclear scatters in the liquid xenon volume with their energies and positions. Figure 5.3 shows the energy spectrum of single scatter events after application of internal Geant4 clustering and detector resolution. This spectrum is only negligibly affected by neutron emission energy input spectra ($<$0.5%).

5.1.2 Simulation of Scintillation and Ionization Signals

The next step of the simulation converts the energy deposited into detected signals from the photomultiplier tubes using the relative scintillation yield ($\mathcal{L}_{eff}$) and ionization yield ($\mathcal{Q}_y$) while applying the proper statistical fluctuations inherent in the underlying processes. Also included are detector corrections and detector efficiencies explained in a later section. The random number generator from the ROOT data analysis framework used here consists of the Mersenne twister

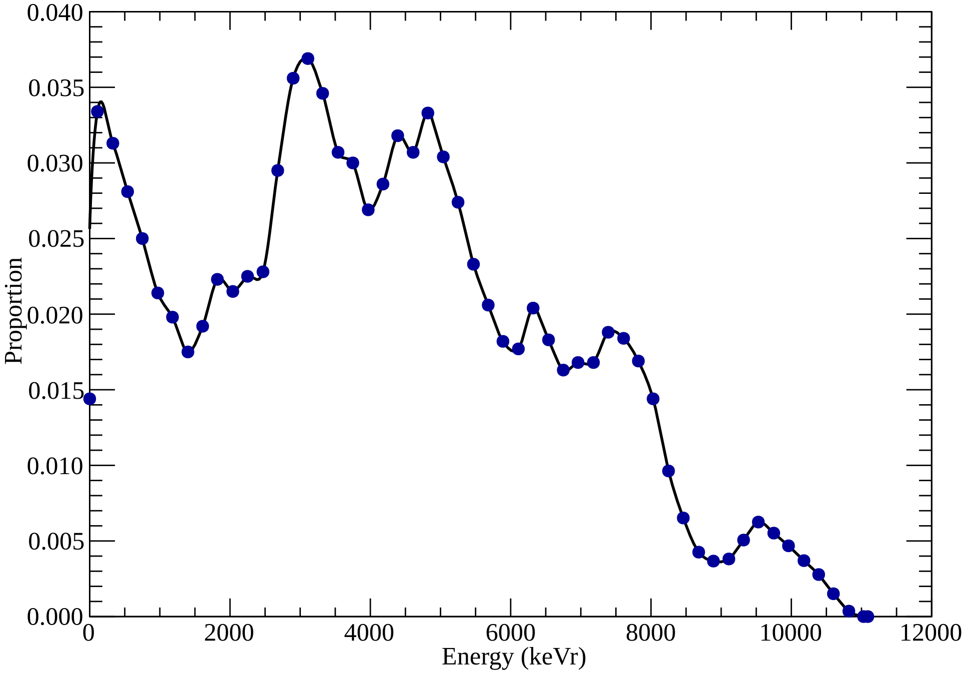

Figure 5.2: Input spectrum for the simulated Americium Beryllium neutron source from ISO 8529-1, 2001 [110].

generator [111].

The simulation of the primary scintillation signal is performed following equations 5.1 and 5.2. The relative scintillation efficiency gives a mean of the number of S1 photoelectrons generated (μ_{S1}) from an energy deposit, E_{nr}, normalized to the center of the detector by the $L_y(122\text{keV}_{\text{ee}})$ ($\tilde{\mu}_{s1}$). This mean is scaled to reflect the position dependent relative light yield of the detector given by figure 3.3. The fluctuations due to photon generation to photostatistics of light collection of the S1 signal are folded into a Poisson distribution with the mean obtained from using $\mathcal{L}_{eff}$ to give N_{pe}.

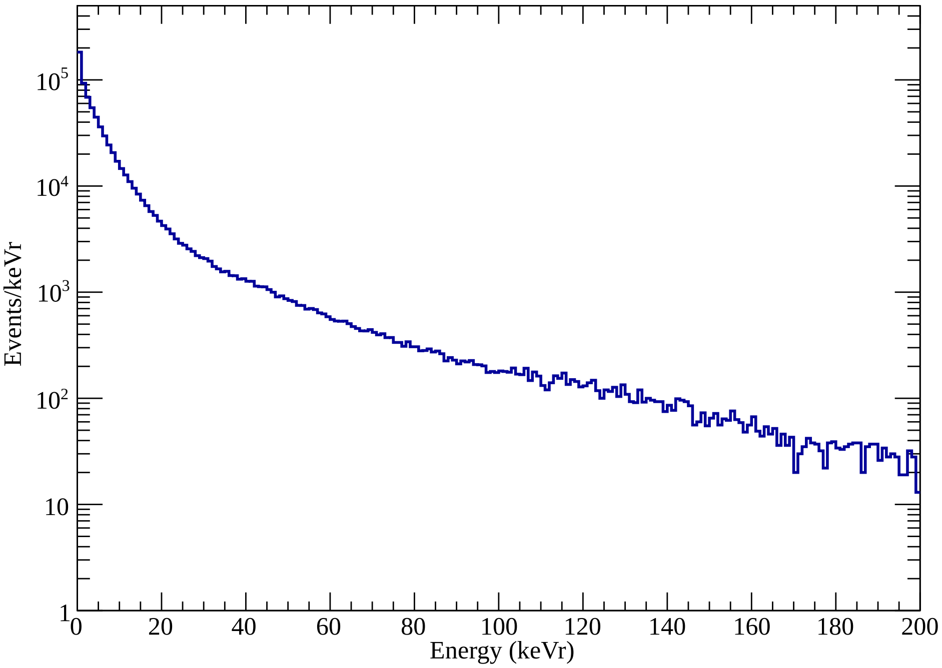

Figure 5.3: Energy spectrum of the Monte Carlo generated data sample of single scatter elastic nuclear recoil events depositing energy in the liquid xenon. From the input spectrum in figure 5.2, 2.7×10^6 events are generated resulting in the detector response shown here.

$$\begin{aligned} \mu_{s1} &= \mathcal{L}_{eff}(E_{nr})E_{nr}\frac{S_{ee}}{S_{nr}}L_y(122\mathrm{keV_{ee}}) \\ \tilde{\mu}_{s1} &= \mu_{s1} \cdot LY_{rel}(R,Z) \\ \mathrm{N}_{pe} &= \mathrm{Poiss}(\tilde{\mu}_{s1}) \end{aligned} \tag{5.1}$$

where the quenching factors for electronic and nuclear recoils are $S_{ee} = 0.58$ and $S_{nr} = 0.95$ for the XENON100 electric field in liquid of 0.53 V/cm [87]. The light yield at 122 $\mathrm{keV_{ee}}$ is determined to be (2.28±0.04) PE/$\mathrm{keV_{ee}}$ from interpolation between the yields of the inelastic 40 and 80 $\mathrm{keV_{ee}}$ lines, the neutron activated

164 and 236 $\mathrm{keV_{ee}}$ lines, and ^{137}Cs calibrations (662 $\mathrm{keV_{ee}}$).

The other smearing to be applied is due to the single photoelectron resolution of the photomultiplier tube, $\sigma_{spe} = 0.45$, determined from experimental data. The processor has a built in efficiency as well, characterized by ϵ_P, denoting the pulse height threshold of 0.35 PE for signal digitization. The signal is then renormalized to the center of the detector, as described in section 3.1.2, using the relative light yield. For events with multiple scatters, the values of the individual S1 signals are added together due the fast timing of the prompt scintillation and small size of the detector while the S2 signals may be distinguished due to the difference in drift times.

$$\begin{aligned} \mathrm{S1}_{sim} &= \sum_{i=1}^{\mathrm{N}_{pe}} \mathrm{Gaus}(\mu_{spe}, \sigma_{spe}) \epsilon_P(\mu_{spe}) \\ \mathrm{cS1}_{sim} &= \frac{S1_{sim}}{LY_{rel}(R, Z)} \end{aligned} \tag{5.2}$$

Starting from a mean charge value μ_{c2}, determined from the ionization yield ($\mathcal{Q}_y$) as shown in equation 5.3, a number of freed electrons in the ionization signal is obtained at the interaction point using a Poisson distribution. In the detector, this electron cloud becomes attenuated due to impurities along the drift path such that S2 signals must be corrected according to the electron lifetime, τ. To account for this in simulation, the initial simulated signal value is considered to be the corrected signal in data and the simulated signal is then "uncorrected" to the raw S2 signal.

$$\begin{aligned}
\mu_{c2} &= \mathcal{Q}_y E_{nr} \\
\mathrm{N}_{e^-} &= \mathrm{Poiss}(\mu_{c2}) \\
\mathrm{cS2}_{sim} &= \sum_{i=1}^{N_{e^-}} \mathrm{Gaus}(\alpha_{se}, \sigma_{se}) \\
\mathrm{S2}_{sim} &= \mathrm{cS2}_{sim} \mathrm{exp}\left(\frac{z}{v\tau}\right)
\end{aligned} \tag{5.3}$$

The electroluminescence process is approximated by summing over the integer value of Poisson fluctuated electrons at the interaction point scaled by the gas gain, $\alpha_{se} = 19.5 \pm 1.1$ PE/electron, sampled from a Gaussian distribution for each electron. To obtain the uncorrected S2 signal, the original simulated signal is modified according to the z-position of the interaction using a standard exponential decay factor, where $v = 1.78 \pm 0.2$ mm/μs is the electron drift velocity at the XENON100 liquid xenon electric field similarly to how the light yield correction was applied to the S1 signal.

A summary of the input parameters for this simulation can be seen in table 5.1. The resulting output consists of observed and corrected S1 and S2 signals, and position information for each scatter of every event.

5.1.3 Modeling the Detector Cuts and Selection Criteria

Extracting the ionization yield from the Monte Carlo to data comparison is performed using the detector response to single scatter nuclear recoils. In data, this is accomplished through the standard single scatter selection

$$\mathrm{S2}[1] < (70 + (\mathrm{S2}[0] - 300)/100) \tag{5.4}$$

where S2[0] and S2[1] are the largest and second largest S2 peaks recognized by

Parameter	Value	Method
Z Resolution	3 mm	Detector
Drift Speed (v)	1.78±0.2 mm/μsec	External [95]
Electron Lifetime (τ)	355±15 μsec	Detector (^{137}Cs)
Light Yield ($L_y(122\mathrm{keV}_{\mathrm{ee}})$)	2.28±0.04 PE/keVee	Detector Interpolation
Quenching for ER (S_{ee})	0.58	External [87]
Quenching for NR (S_{nr})	0.95	External [87]
SPE Mean (μ_{spe})	1.00±0.15 PE	Detector (AmBe)
SPE Width (σ_{spe})	0.44±0.05 PE	Detector (AmBe)
SE Mean (α_{se})	19.5±1.1 PE/e^-	Detector (AmBe)
SE Width (σ_{se})	7.2±0.7 PE/e^-	Detector (AmBe)
S1 Time Window	±20 ns (50 ns total)	Processor

Table 5.1: Input parameters for the XENON100 analytical Monte Carlo.

the processor. This protects against removing an event due to the presence of single electron emission signals from photoionization [112] typically on the order of 20 PE following large S2 signals. This selection criterion has been measured to have greater than 99% acceptance of single scatter nuclear recoils. On the other hand, events with genuine double scatters are removed effectively, with the exception of second scatters falling under the $(70+(\mathrm{S2}[0]-300)/100))$ threshold. These scatters remain in data but are also present in Monte Carlo data and do not pose a problem for spectral matching between the two data samples.

The other two important selection criteria are related to the thresholds for each of the signal channels: the S1 coincidence cut and the S2 threshold. The S1 coincidence cut assures that the S1 signal is recorded by two PMTs during a 50 ns window setting a soft threshold at 2 PE. The acceptance of this cut has been

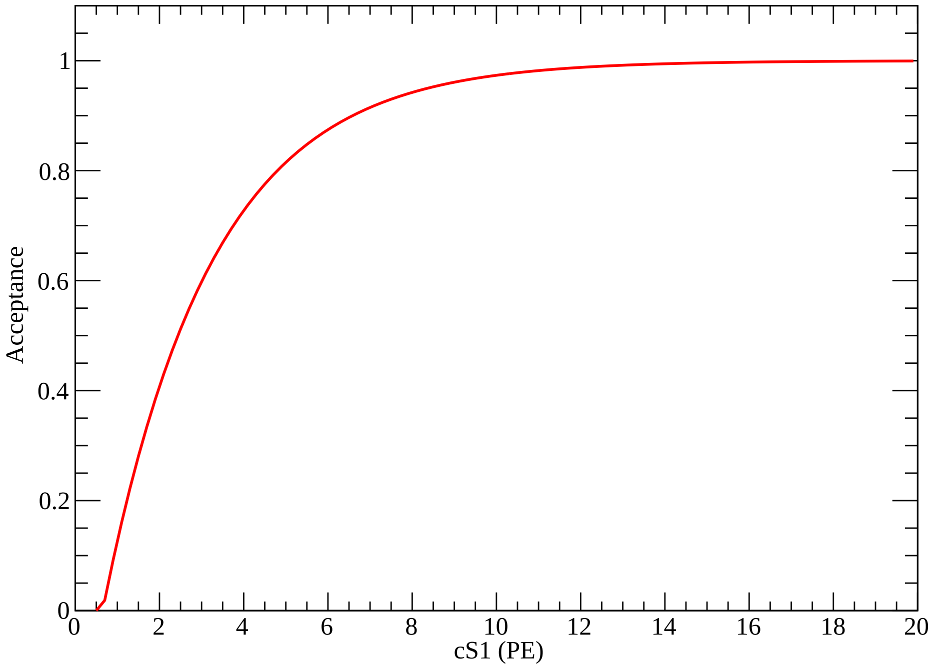

Figure 5.4: Acceptance of the S1 coincidence cut applied to simulated neutron data as a function of the S1 signal size. The acceptance was determined from vetoed events, which allows for the improved accuracy at low S1 values.

quantified by using a sample of vetoed data to ensure the validity of an event even for if it has only a single event in the TPC (with an additional one in the veto as a requirement). Its functional dependence is shown in figure 5.4. In the simulation, the analytical form of the acceptance is used and events are removed following a binomial process. The S2 threshold at 150 PE is set such that there is greater than 99% trigger efficiency for all signals. This is applied inherently to the Monte Carlo data through the uncorrected S2 signal. The acceptance loss is characterized in comparison to the Xenon100 parameterization using the WIMP model described in section 5.5.

The data sample also includes acceptance losses due to data quality cuts. The acceptance for the nuclear recoil scatters has been determined as shown in the two dimensional distribution in figure 5.5. This is obtained by taking the sample of events following single scatter selection, applying the remaining cuts (table 5.2), and dividing the two

$$\epsilon_i = \left(\frac{N_{ac}}{N_{ss}}\right)_i \tag{5.5}$$

for the i-th bin in S1 versus S2 phase space, where ac is for all cuts and ss is for single scatter. This is applied to the simulation using a binomial process for each event.

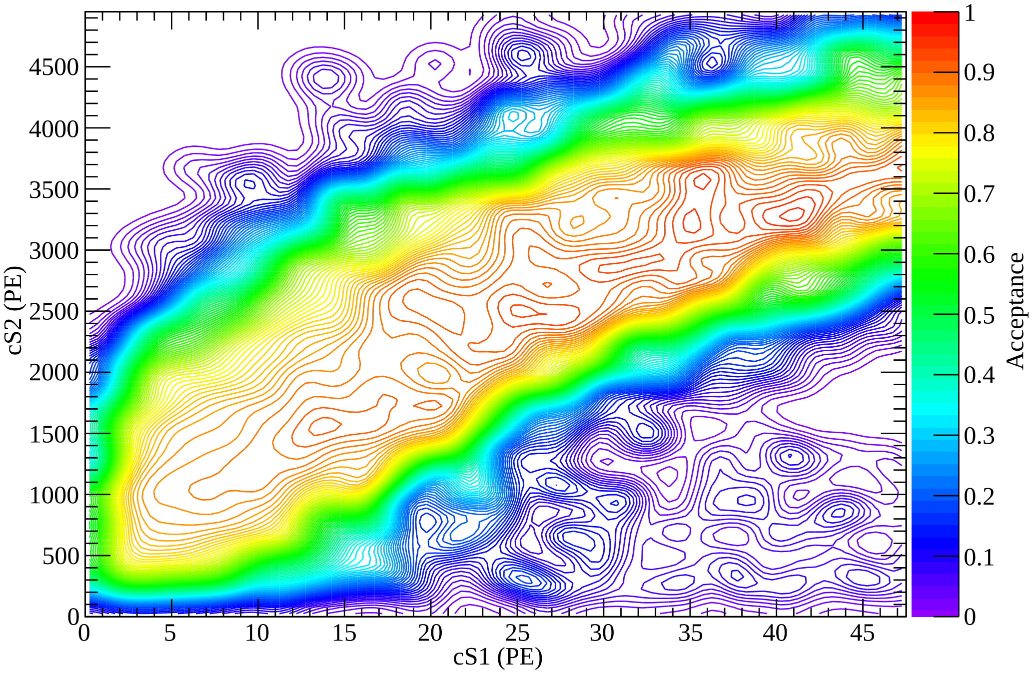

Figure 5.5: Acceptance of the quality cuts in the two dimensional space of S1 versus S2. The majority of the loss of acceptance comes from the S2 width cut.

The individual cut acceptances shown in table 5.2 are determined by taking the data sample with all cuts normalized by a sample with all cuts besides the one of interest. The cuts with the largest effects are the S2 width and PMT pattern likelihood cuts, which select neutron events based on the characteristic width distribution and the expected PMT pattern of nuclear recoil events from optical simulations.

Cut Name	Purpose	Avg. Acceptance (%)
S2 Width	Background discrimination using ionization signal time width	92
Signal-to-Noise	Removes events with high proportion of total waveform area not in main signal peaks	98
S1 Width	Removes fast signals	100
S1 Single	Events can only have a single S1 peak	98
PMT Patt. LL	Anomalous PMT pattern events	100
S2 χ^2		100
PosRec		96

Table 5.2: Data quality cuts with their purposes and acceptances

5.2 Neutron Calibration Data Sample

The data sample used for this study from the AmBe calibration source uses the single scatter selection and data quality cuts (previous section) and a $\pm 3\sigma$ cut on the discrimination parameter for outlying events. The data consists of 1.1 days of livetime taken during in February 2011 with 4.3×10^4 events passing all cuts. The data acquisition rate of 18 Hz during this period resulted in a negligible 0.25% deadtime due to the 1 ms trigger holdoff.

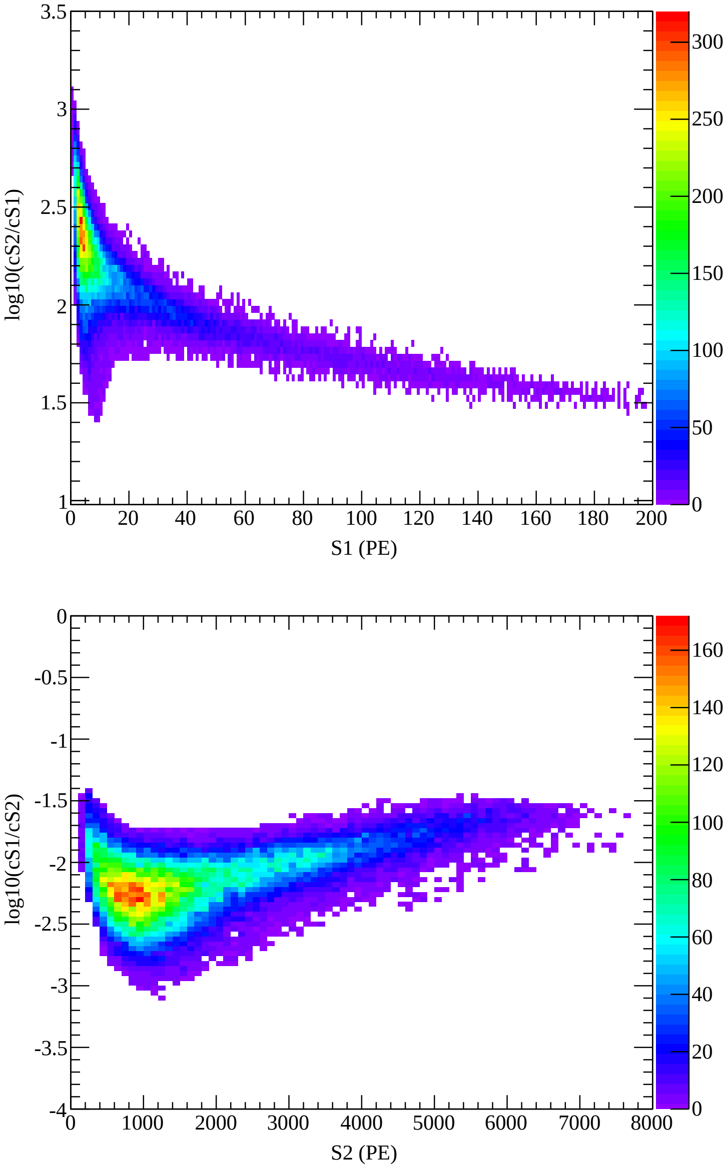

Figure 5.6: Two dimensional distributions of neutron calibration data in both phase spaces discussed previously, $\text{Log}_{10}(\text{S2}/\text{S1})$ versus S1 (*top*) and $\text{Log}_{10}(\text{S1}/\text{S2})$ versus S2 (*bottom*).

Figure 5.6 shows the distributions of the data for a 30 kg fiducial volume in the traditional $\text{Log}_{10}(\text{S2/S1})$ versus S1 and new $\text{Log}_{10}(\text{S1/S2})$ versus S2 phase spaces after removal of the inelastic gamma lines, which are at 40 and 80 keV_{ee} (or around 100 and 250 PE S1), but separated from the neutron population. The one dimensional distributions of the calibration data shown in figure 5.7 are used for the minimization of both $\mathcal{Q}_y$ and $\mathcal{L}_{eff}$.

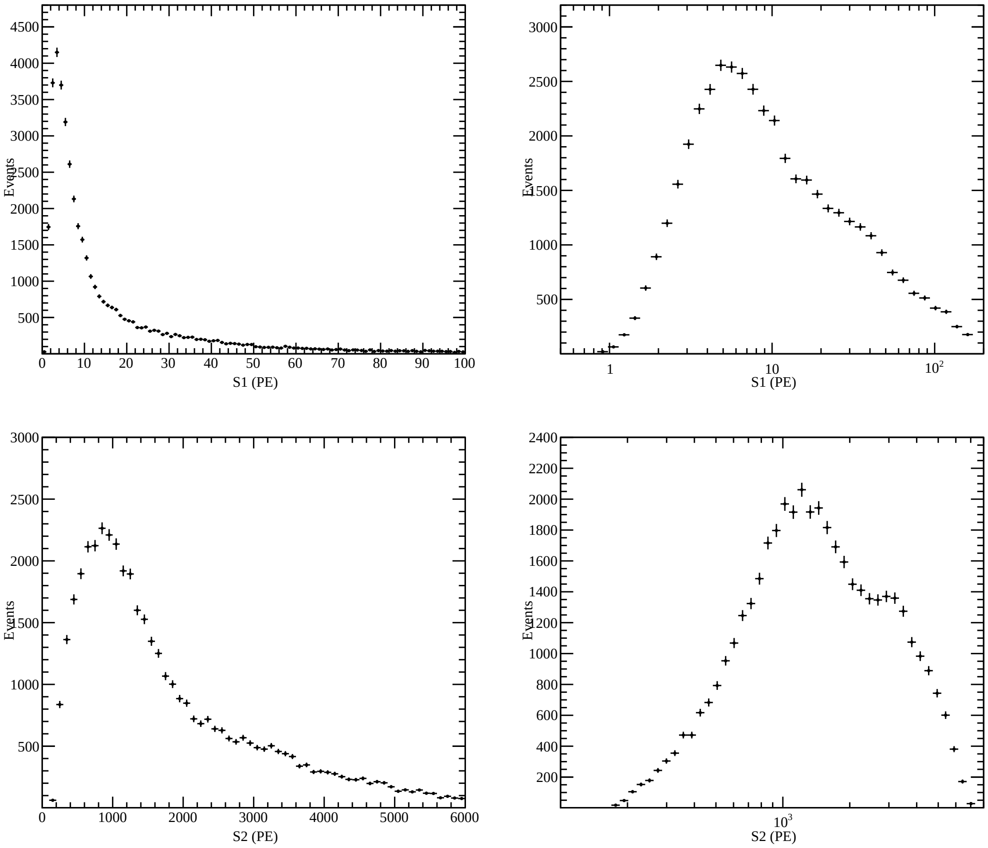

Figure 5.7: Spectra from neutron calibration data after application of all data cuts. *Top Row:* Event distribution along the S1 axis in both linear and log binning. *Bottom Row:* Event distribution along the S2 axis. The log distributed spectra are used in the minimization comparison.

The data for the observed S1 is placed into 50 evenly spaced log-bins or 200 linear bins over the range 0 to 200 PE while the S2 spectra is split over 50 log-bins in the range or 80 linear bins for 0 to 8000 PE. The fitting range for $\mathcal{L}_{eff}$ and $\mathcal{Q}_y$ determination will be discussed in a later section.

5.3 Absolute Flux Normalization

An external measurement of the AmBe neutron source strength has been measured in a dedicated ^{3}He spectrometer setup by the German National Metrology Institute, PTB. The emission rate was measured to be (161±10) n/s, which includes systematic uncertainties due to flow isotropy. For the comparison between Monte Carlo data and neutron calibration data, this rate is held fixed such that no scaling to the simulated neutron rate is applied. Additionally, coincidences between neutrons and direct γ-rays from the source affect this result only negligibly as they are uncorrelated in angular distribution.

5.4 Minimization Procedure

The nonlinear least squares Levenberg-Marquardt (LM) algorithm [113, 114, 115] is a damped Gauss-Newton method, which oscillates between steepest descent and Gauss-Newton modes. This allows it to be effective even when the initial choice of parameters is far from the minimum. The algorithm is characterized by the damping parameter, which determines the direction and size of the next step and is iteratively modified depending on the χ^2-value at each stage. The χ^2 statistic is determined by the binned Monte Carlo (Theoretical) and neutron calibration (Experimental) data from Pearson's chi-squared test [116]

$$\chi^2 = \sum_{i=1}^{n} \frac{(N_o^i - N_e^i)^2}{N_e^i} \tag{5.6}$$

where N_o and N_e are the number of events observed in data and expected by the simulation.

The two minimizations of interest are for determination of the ionization yield while holding the relative scintillation yield fixed (by default, the $\mathcal{L}_{eff}$ for the XENON100 experiment is chosen) and for understanding the relative scintillation yield using the result from the initial ionization yield minimization routine. Because the two channels are decoupled once the energy of an event is known, this two-fold technique provides the simplest way to determine the yields. A two dimensional minimization was attempted using both ionization and relative scintillation yields as free parameters, but a lack of statistics in the data sample made it increasingly difficult to obtain a consistent result.

5.4.1 Determining $\mathcal{Q}_y$

The ionization yield is modeled by a set of seven spline points at E$_{nr}$= {1, 3, 8, 15, 25, 40, 100, 250} keV$_\mathrm{r}$ connected using an Akima spline interpolation [117], which is stable near the outlying points with a continuous first derivative. The yield assumes a constant value outside the endpoints equal to the yield at that endpoint. The spline energies were chosen to be able to reflect the expected shape of the curve and are independent and unconstrained in value. The spline values are then varied to give the best agreement between the measured and simulated S2 spectra. Similar analyses have been performed by the XENON10 [118] and ZEPLIN III [92] collaborations.

The minimization is performed over the log binned histograms above 160 PE

S2 for a total of 43 bins with the seven spline points, which results in 36 degrees of freedom. After a minimum of 100 trials, using a different random seed each time to characterize the simulation with the same initial spline values at $x_s = \{3.0, 3.0, 3.0, 3.0, 3.0, 3.0, 3.0\}$, the result of the best-fit Monte Carlo-observed data spectral comparison can be seen in figure 5.8, with a χ^2=233.0/36 from an initial χ^2=19751.5/36. The large reduced-χ^2 for this fit is due to underlying systematic errors, which if included at an average of 6% due to input spline starting choice and random number generation then χ^2=49.0/36.

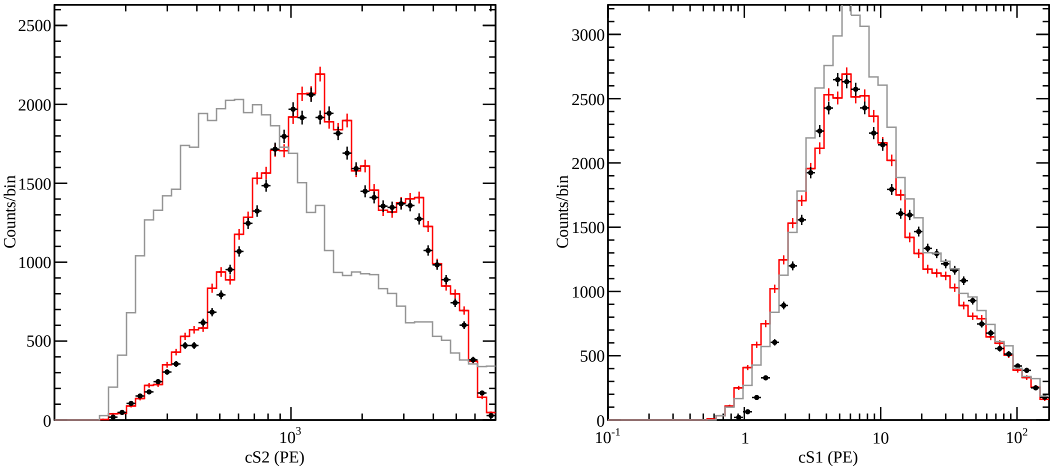

Figure 5.8: Spectral comparison of the fitted simulation (*red*) and observed data (*black*) after fitting the S2 spectrum for the ionization yield. Shown in *gray* is the spectrum with spline values at their initial positions.

The ionization yield can be seen in figure 5.9 with error bars originating from both statistical and systematic uncertainties. The result follows the theoretical expectation over the full energy range except for a variation in shape over low to intermediate energies. This could be modified with the variation of the theoretical input parameters. Once the best-fit yield has been found, the initial spline starting points for the systematic studies are modified to the best-fit values.

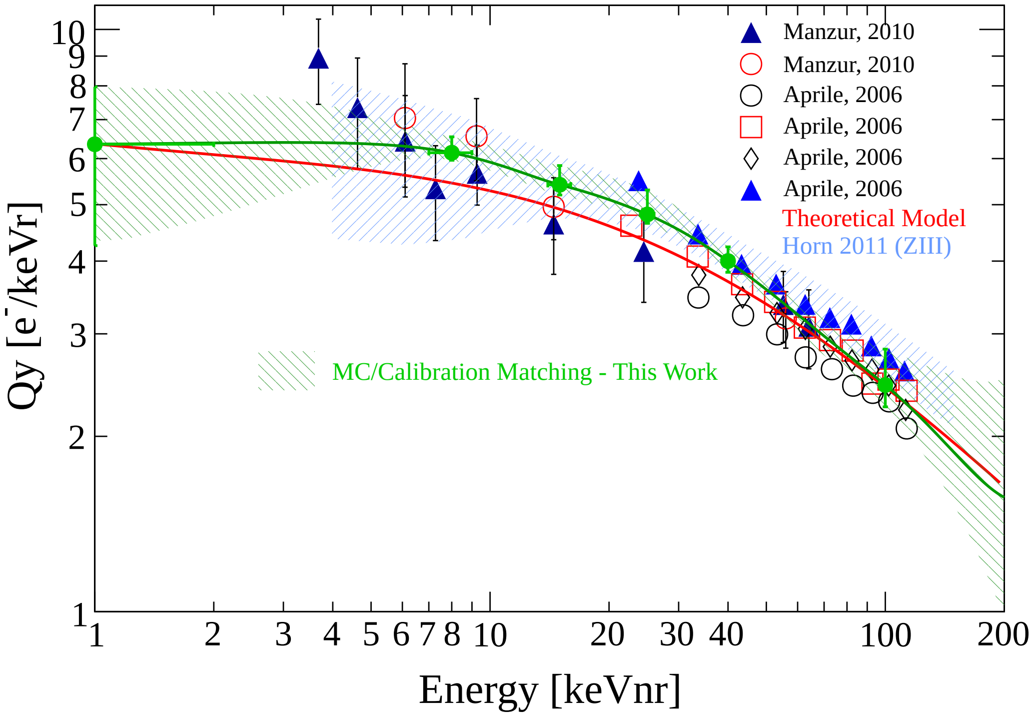

Figure 5.9: Ionization yield obtained from nonlinear χ^2 minimization of the Monte Carlo and calibration data. Uncertainty bounds are determined by adding each of the uncertainties in table 5.3 in quadrature. The theoretical model is the same as was used in the previous chapter.

5.4.1.1 Uncertainties in the Ionization Energy Scale

The major uncertainties in determining the ionization yield are due to the systematic uncertainties of the input parameters from $\mathcal{L}_{eff}$, the cut acceptances, and initial conditions on spline value definition. Other lesser systematic uncertainties arise from statistical fluctuations inherent in the random generation of signal statistics or minimization starting parameter, μ. A summary of the results of the uncertainties studied are shown in table 5.3.

		Uncertainties			
Energy	Value	Statistical	$\mathcal{L}_{eff}$	Acceptance	Initial Spline Choice
1	6.35	$^{+0.17}_{-0.09}$	$^{+1.32}_{-0.79}$	$^{+0.84}_{-1.6}$	$^{+0.38}_{-1.10}$
8	6.14	$^{+0.04}_{-0.05}$	$^{+0.34}_{-0.14}$	$^{+0.14}_{-0.15}$	$^{+0.15}_{-0.10}$
15	5.41	$^{+0.03}_{-0.03}$	$^{+0.36}_{-0.08}$	$^{+0.17}_{-0.05}$	$^{+0.15}_{-0.19}$
25	4.81	$^{+0.05}_{-0.03}$	$^{+0.34}_{-0.02}$	$^{+0.22}_{-0.02}$	$^{+0.27}_{-0.16}$
40	4.00	$^{+0.02}_{-0.03}$	$^{+0.16}_{-0.01}$	$^{+0.09}_{-0.00}$	$^{+0.15}_{-0.17}$
100	2.45	$^{+0.02}_{-0.01}$	$^{+0.15}_{-0.01}$	$^{+0.21}_{-0.03}$	$^{+0.27}_{-0.20}$
250	1.61	$^{+0.02}_{-0.03}$	$^{+0.13}_{-0.03}$	$^{+0.43}_{-0.16}$	$^{+1.20}_{-0.89}$

Table 5.3: Uncertainties in the determination of the Ionization Yield, $\mathcal{Q}_y$

The uncertainties in the table are obtained by varying input conditions (within their individual uncertainties if they are characterized): the random generation seed, observed histogram statistics, $\mathcal{L}_{eff}$, acceptance, and spline properties. The underlying random seed for the generation of observable S1 and S2 signals is varied for every iteration such that some measure of its uncertainty is convoluted within the uncertainties of the other qualities. The histogram bin contents are allowed to vary within their Poisson fluctuations, which characterizes the statistical uncertainty. The uncertainty bounds for the relative scintillation yield are taken from figure 5.11 as determined by the XENON100 collaboration [69]. Uncertainty for the acceptance is conservatively taken to be ±5% from the central value. Spline uncertainty originates from choice of spline energies (negligible if energies are reasonable), and initial spline value. For the latter, both the choice of absolute spline value and fluctuations around the best fit $\mathcal{Q}_y$ are included.

The majority of uncertainty in the ionization yield appears at low energies, where variation in the input parameters causes the largest fluctuations. In general, the $\mathcal{Q}_y$ is skewed towards higher yields for the different sources of uncertainty. Other situations where the minimization does not converge are not taken further into account as well as uncertainties in PMT resolution, neutron cross section data, and neutron source normalization.

5.4.2 Determining $\mathcal{L}_{eff}$

The slight mismatch in the S1 spectrum in figure 5.8 at low energies can be remedied by applying the same minimization procedure to the relative scintillation yield while holding the ionization yield to its most likely parameterization determined in the previous section. The $\mathcal{L}_{eff}$ is parameterized by a set of eight spline points at $E_{nr}=$ {1, 3, 8, 15, 25, 40, 70, 140} keV$_r$ with initial values $x_s =$ {0.0, 0.1, 0.2, 0.2, 0.2, 0.2, 0.2, 0.2}. The fit is performed using the upper 35 bins from above 1.4 PE S1 due to poor understanding of the detector below 1 PE.

The fitting procedure results in figures 5.10 and 5.11, which show the fitted S1 spectra and corresponding S2 spectra and the best-fit relative scintillation yield. The initial fit (χ^2=2564.5/27) is improved to χ^2= 642.351/27 indicating only a slight improvement and suggesting a separate underlying issue possibly due to the efficiency or other systematic effect not considered. The spectra do not look visibly different from that of figure 5.8, but the improvement will be evident when considering the distribution of S1 and S2 in a two dimensional space.

5.4.3 Two Dimensional Comparison

In addition to the one dimensional spectra, it is worthwhile to understand the underlying correlation between the two observation channels by comparing two dimensional phase distributions. Figure 5.12 in S2 versus S1 shows the quantiles

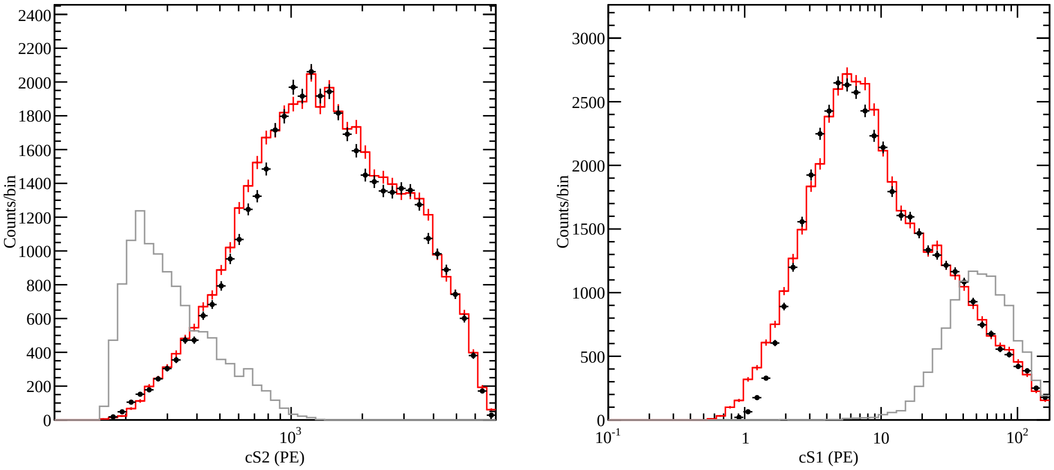

Figure 5.10: Spectral comparison of the fitted simulation (*red*) and observed data (*black*) after fitting the S1 spectrum for the relative scintillation yield. Shown in *gray* is the spectrum with spline values at their initial positions.

after each of the fitting routines for the ionization yield and then the relative scintillation yield. The slices of the distribution can be seen in figure 5.13 for various S1 ranges.

With the framework provided here, both the means and one sigma bands of the S1 and S2 signals have been reproduced effectively with the exception of very low signal values (S1 $<$ 2 PE). The lower quantiles of the S2 versus S1 phase space are affected by double scatter neutron events, which have only a single ionization signal. Despite this, the simultaneous modeling of both the S1 and S2 signals with statistical fluctuations constrains the energy conversion factors $\mathcal{L}_{eff}$ and $\mathcal{Q}_y$ very well and allows for not only a complete WIMP model simulation, but a better understanding of detector cuts and estimation of efficiencies from neutron calibration data.

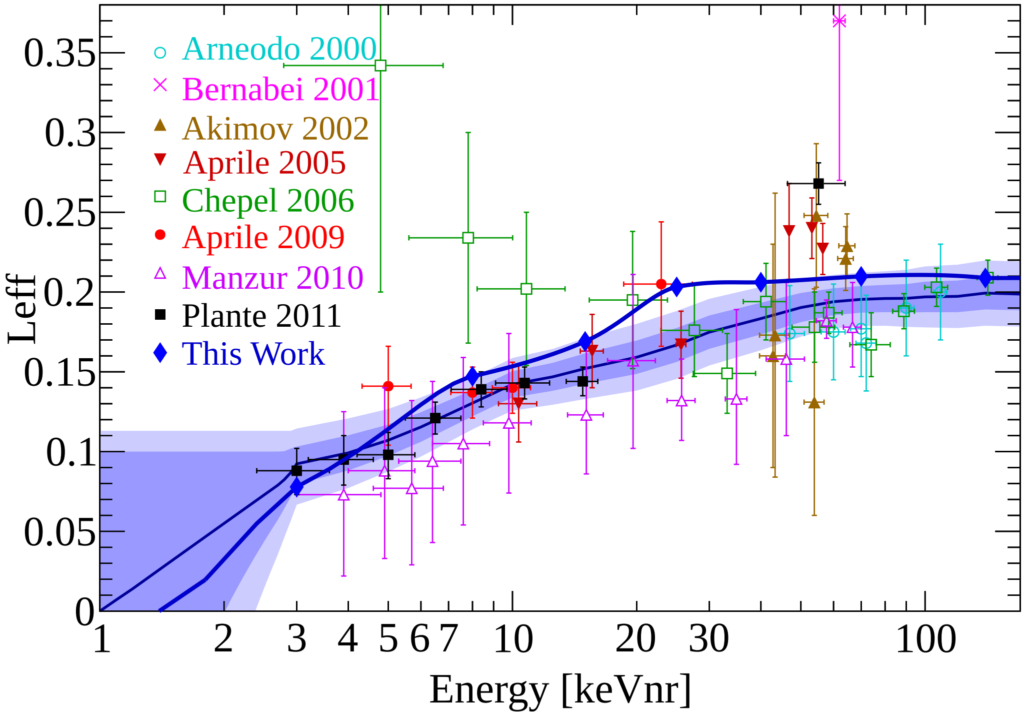

Figure 5.11: Relative scintillation yield, $\mathcal{L}_{eff}$, after minimization with the non-linear least squares method. The yield varies slightly from the parameterized function determined by the XENON100 collaboration (*black*) especially at higher energies.

5.5 WIMP Model Simulation

To determine the sensitivity of the XENON100 detector to a WIMP signal, a reliable WIMP model is necessary for the statistical treatment. Taking the energy spectra from Chapter 1 and the simulation developed here allows for the generation of WIMP models for any mass desired. The models follow immediately from the neutron simulation with the energy spectrum of the WIMP replacing the neutron energy scatters. For a given mass and cross section, a number of events (equation 5.7)

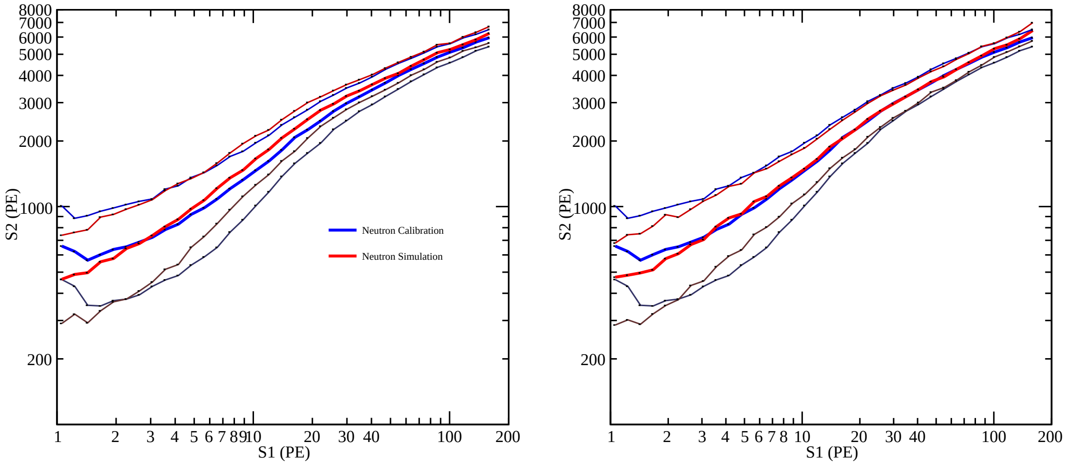

Figure 5.12: Median (*bold*) and $\pm 1\sigma$ quantiles after finding the best-fit $\mathcal{Q}_y$ (*left*) and $\mathcal{L}_{eff}$ (*right*). The improvement in agreement after minimization procedure for the relative scintillation is most evident in the median quantile. The first sigma quantiles and near threshold are dominated by statistical fluctuations and multiple scatter events with only a single ionization signal and do not agree nearly as well.

$$\mathrm{N} = \left(\int \frac{\mathrm{d}R}{\mathrm{d}Q}\mathrm{d}Q\right) \times \mathrm{Exposure} \tag{5.7}$$

where their energy and position are randomly sampled from the distribution of the differential rate, $\mathrm{d}R/\mathrm{d}Q$ and the target fiducial volume (34 kg), and are passed to the simulation package.

The results of this simulation for various WIMP masses and cross sections in the standard phase space can be seen in figures 5.14. For high masses, the WIMP distribution follows the same trend as the neutron simulation or calibration data. At low masses however, the WIMP model begins to shift due to the S2 dependence in the discrimination parameter (downwards in the standard phase space).

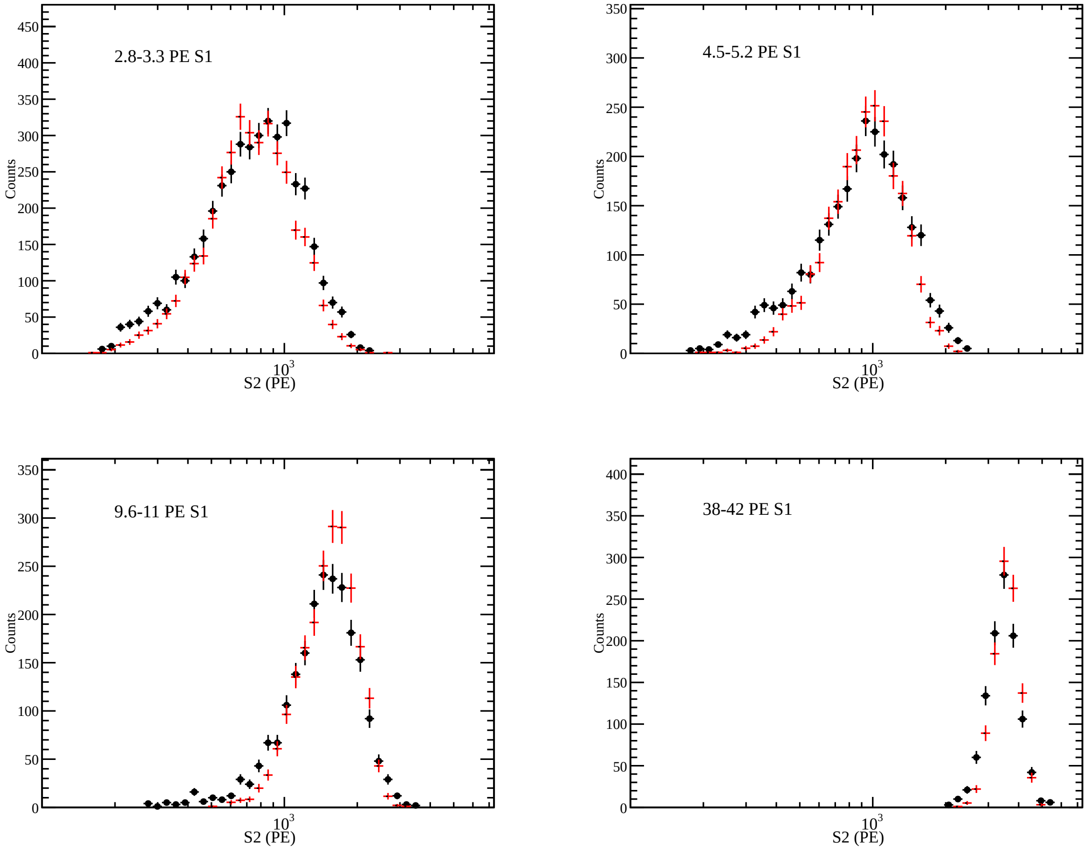

Figure 5.13: Slices of the two dimensional distribution projected along the S2 axis for several ranges of S1. The Monte Carlo is shown in *red* and data is shown in *black*. Error bars are given by the Poisson statistics of each bin.

The standard analysis on the other hand, employs the projected distribution of the neutron calibration data along the discrimination parameter axis and with the WIMP energy spectrum converted to the S1 axis with underlying Poisson fluctuations.

The population of events at low values of $\text{Log}_{10}(S2/S1)$ in data are attributable to neutron double scatters from the dead region below the cathode which have only a portion of their S2 light and are shifted down in the phase

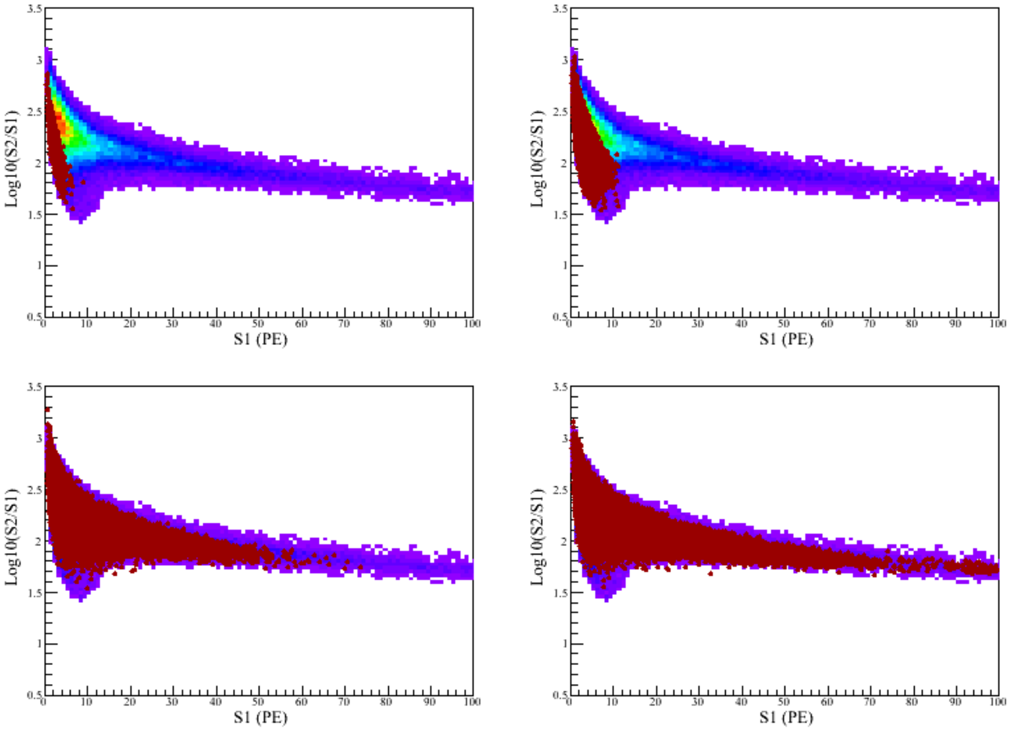

Figure 5.14: WIMP simulated distributions (*red*) using the simulation and energy scales developed in this chapter for the standard phase space. The underlying distribution is neutron calibration data. The panels are for 6, 10, 50, and 500 GeV.

space.

The same WIMP models for the new phase space, $\text{Log}_{10}(\text{S1}/\text{S2})$ versus S2, can be seen in figure 5.15. These distributions demonstrate the advantages of using the S2 as the energy estimator especially for the low mass cases, where the resolution and estimation of the energy of an event improve (Chapter 4).

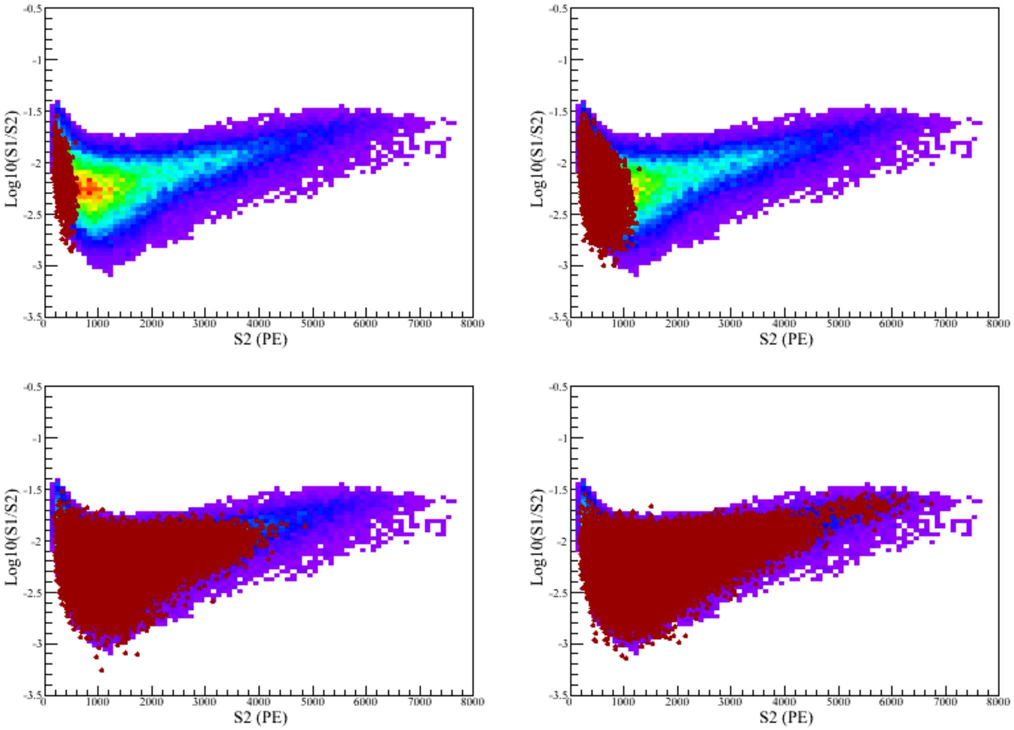

Figure 5.15: WIMP simulated distributions (*red*) using the simulation and energy scales developed in this chapter for the new phase space. The underlying distribution is neutron calibration data. The panels are for 6, 10, 50, and 500 GeV.

5.5.1 Acceptance Considerations

The traditional approach of modeling the WIMP using the S1 distribution and neutron discrimination profile effectively decreases the signal acceptance and reduces sensitivity in a conservative way. Recall figure 3.4 which shows the acceptance of signal below the rejection line, which is less than 70% over the full region. Figure 5.16 shows the background distribution and a simulated 10 GeV/c^2 WIMP distribution with the traditional signal region. If we use this WIMP distribution instead of the AmBe neutron data, the true acceptance is found to be greater

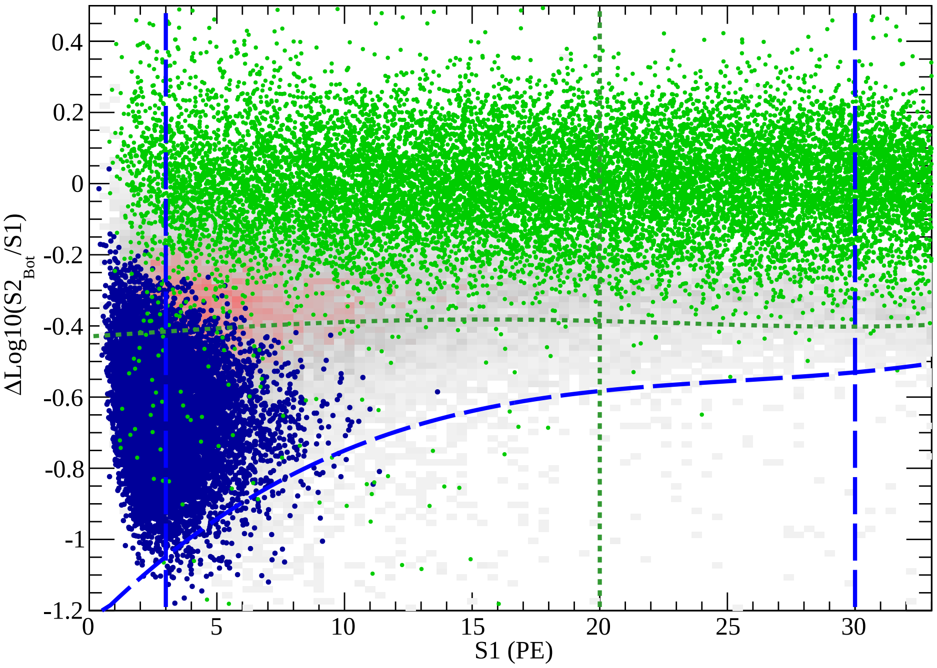

Figure 5.16: Gamma calibration data (*green*) and WIMP 10 GeV simulated distribution (*blue*) in the flattened phase space with signal region denoted below the (*green-dotted*) line between 3 and 20/30 PE S1.

than 90% for the full region because the distribution is shifted downwards in the phase space due to the S2 dependence along the Y-axis.

Using the WIMP simulation also allows for the intrinsic determination of the S2 acceptance versus S1, which can be framed in reference to the XENON100 acceptance used for publication. The S2 threshold cut is applied to the simulation through the "uncorrected" S2 signal, which has an inherent energy dependence due to the need to correct from the Z position of the interaction. This leads to a WIMP mass dependent acceptance from the varying spectral shape as shown in figure 5.17 and explained briefly in [69].

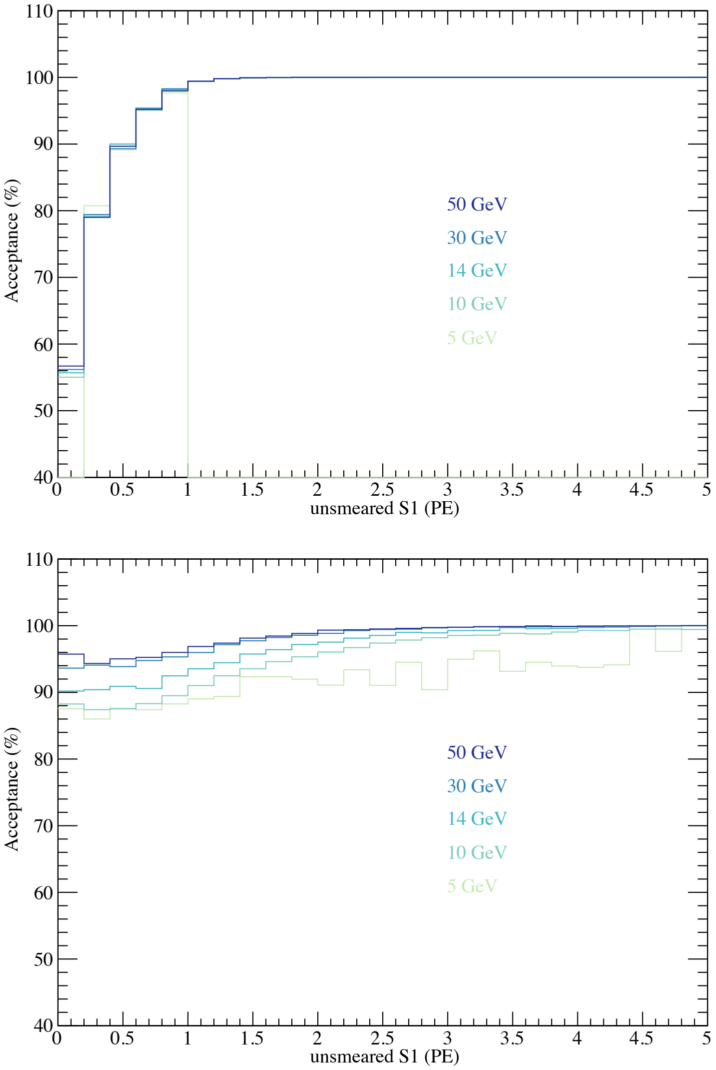

Figure 5.17: Extracted acceptance of the S2 threshold cut using the WIMP simulation and energy conversions defined here. *Top:* Acceptance versus unsmeared S1 (before Poisson smearing the signal and applying PMT resolution). All masses follow similar trends. *Bottom:* After smearing, the mass dependence of the acceptance becomes evident, but has only a very small effect above the standard analysis threshold of 3 PE.

At low WIMP masses and smeared S1 signal values, the acceptance varies by 7% at lowest energies, but for the traditional region of interest above 3 PE, the difference between most of the masses except below 10 GeV/c^2 are negligible. The advantage of this simulation is the inherent application of this acceptance without having to apply an external correction as is done in the standard XENON100 analysis.

By modeling geometry using Geant4 and the underlying statistical processes inherent in observing energy depositions of the XENON100 detector, it is possible to extract the detector response to ionization signals ($\mathcal{Q}_y$, the ionization yield) and subsequently model WIMP recoils from both primary and secondary scintillation. This measurement, in lieu of more robust external measurements of the ionization yield, gives the possibility of applying the two dimensional analysis method presented in the previous chapter with the proper WIMP simulation for a more robust statistical analysis. In the future, having further understanding of the $\mathcal{Q}_y$ from other measurements will allow this Monte Carlo to then extract detector behavior and efficiencies with much less uncertainty.

CHAPTER 6

XENON100 Statistical Analysis

To assess the significance of a signal excess or place limits on the WIMP-nucleon cross section, new statistical analyses on the XENON100 dark matter data run from 2011-2012 are presented here in the Log_{10}(S1/S2) versus S2 phase space, which employ the WIMP Monte Carlo model developed in Chapter 5. Both the Feldman-Cousins likelihood ratio ordering and the profile likelihood statistical approaches are considered with respect to the traditional analysis method [119, 103]. Starting from this standard method, the improvement at each change to the analysis procedure is quantified until the final result of the expected sensitivity and upper limit of the XENON100 experiment from the profile likelihood analysis.

The two statistical techniques, Feldman-Cousins and profile likelihood, provide methodology to obtain confidence intervals on a WIMP signal. The Feldman-Cousins method is a frequentist statistical technique that assumes knowledge of the expected background in a predefined low-background region of phase space without including uncertainties giving a coarse understanding of the sensitivity of an experiment. The more powerful profile likelihood analysis incorporates systematic uncertainties of input parameters over the full phase space to improve the sensitivity available to an experiment while maintaining a majority frequentist framework.

6.1 Feldman-Cousins Statistics

The Feldman-Cousins (FC) method [120] is a likelihood ratio ordering process to characterize the interval construction for small signal analysis of a Poisson process with background. We are interested in determining a confidence interval for a desired confidence level (α) with the property that they contain the true value of the signal mean, μ_t, in a fraction α of experiments (frequentist statistics) as shown below

$$P(\mu \in [\mu_1, \mu_2]) = \alpha \tag{6.1}$$

where μ_1 and μ_2 are functions of observed data for a fixed μ for an ensemble of experiments. This is opposed to Bayesian construction where the confidence level indicates a degree of belief about μ_t.

For a traditional Poisson process with background, the probability density function is

$$P(n|\mu) = \frac{(\mu + b)^n e^{-(\mu+b)}}{n!} \tag{6.2}$$

where n is the observed number of events in some predefined signal region and b is the expected background in that region. Since the observed events is always an integer, construction of an interval to cover at the stated confidence level can only be approximated and are instead stated to overcover in a conservative manner. The interval construction is obtained by taking the Poisson likelihood ratio (R)

$$R = \frac{P(n|\mu)}{P(n|\mu_{best})} \tag{6.3}$$

where μ_{best} is the mean value of the signal which maximizes the likelihood, and constructing confidence belts for each value of μ and fixed b. The belt is defined by starting from the largest R and adding values until the desired confidence level is achieved for the specified μ. The confidence interval is given by spanning across the belts for the given number of observed events n, which gives the interval $[\mu_1, \mu_2]$. Typically, a computer database provides the resulting interval for a given number of observed events and expected background.

This approach is heavily dependent upon precisely understanding the expected background and does not consider systematic uncertainties attached to any of the input parameters. The simplicity and ease of the calculation do allow for quick systematic checks to be applied however.

6.1.1 Systematic Effects on the Upper Limit

The starting point of reference for the upper limit calculation originates from the traditional Log_{10}(S2/S1) versus S1 phase space with a signal range of 3 to 20 PE S1 and background expectation of 1.0±0.2 events from the XENON100 analysis. Smearing from below 1 PE of the S1 signal (which is effectively setting $\mathcal{L}_{eff}$ to zero below ~3 keV$_r$) is also ignored as part of the application of the S2 threshold acceptance (figure 3.4), which effectively makes the detector insensitive to 5-6 GeV/c^2 WIMPs (figure 5.17).

With an observed event count in the signal region of 2, this results in an upper limit of signal events of 4.915 (with a lower bound of 0 events) from FC statistics. Following the procedures documented in XENON100 analyses [121, 119], the spectra projected along the S1 axis are obtained with the neutron acceptance shown in figure 3.4, resulting in the upper limit as shown in figure 6.1. The difference between this limit and the published limit (particularly at higher WIMP masses) can be attributed exclusively to the statistical analysis applied, Feldman-Cousins

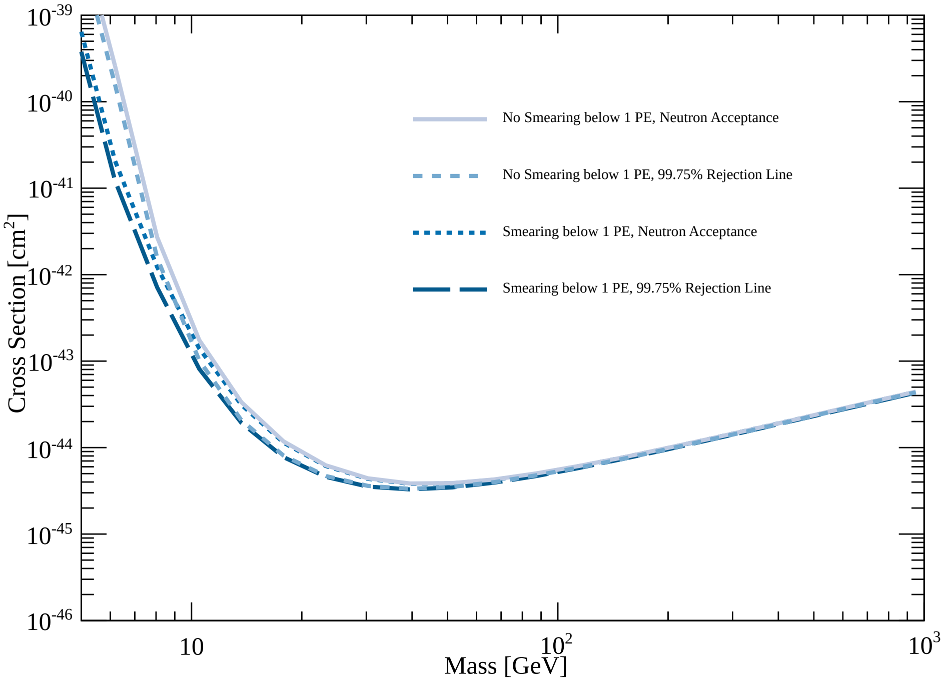

Figure 6.1: 90% confidence level (CL) upper limits on WIMP elastic dark matter cross sections calculated from the traditional phase space under different conditions. The smearing of the S1 signal from below 1 PE and the acceptance for the WIMP signal are considered.Neutron acceptance in the legend designates using the AmBe calibration data for the acceptance, while 99.75% indicates using the WIMP model for the acceptance.

in this work versus a profile likelihood method in the publication. Improvements to this upper limit will be quantified only with respect to the analysis performed here.

The other limits shown in figure 6.1 are derived from changes in the signal region acceptance and in the underlying physics model. Allowing smearing from below 1 PE provides the greatest improvement at low energies as shown in fig-

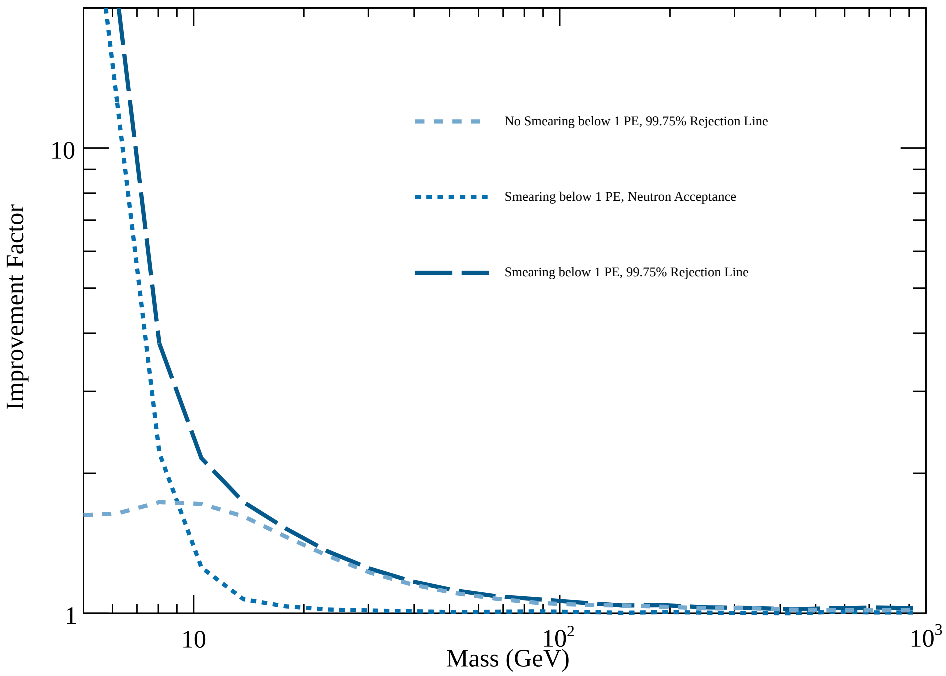

Figure 6.2: Improvement in the exclusion limit due to changing input conditions. Below about 10 GeV, the improvement factors from both smearing and acceptance changes are significant: about a factor of 2 for the acceptance and between 2 and greater than 10 for including smearing below 1 PE.

ure 6.2 from greater than a factor of 20 at less than 6 GeV to about a factor of 2 at 8 GeV. The change in physics model from the neutron calibration data to the WIMP model improves the acceptance at low energies resulting in improvement of about a factor of 2 up to about 40 GeV.

In moving to the $\text{Log}_{10}(\text{S1}/\text{S2})$ versus S2 phase space, it is important to first decide the choice of signal region and calculate the expected background for the Feldman-Cousins analysis. Figure 6.3 shows an a priori selected (before unblinding) signal region for the full WIMP mass range. Taking the gamma

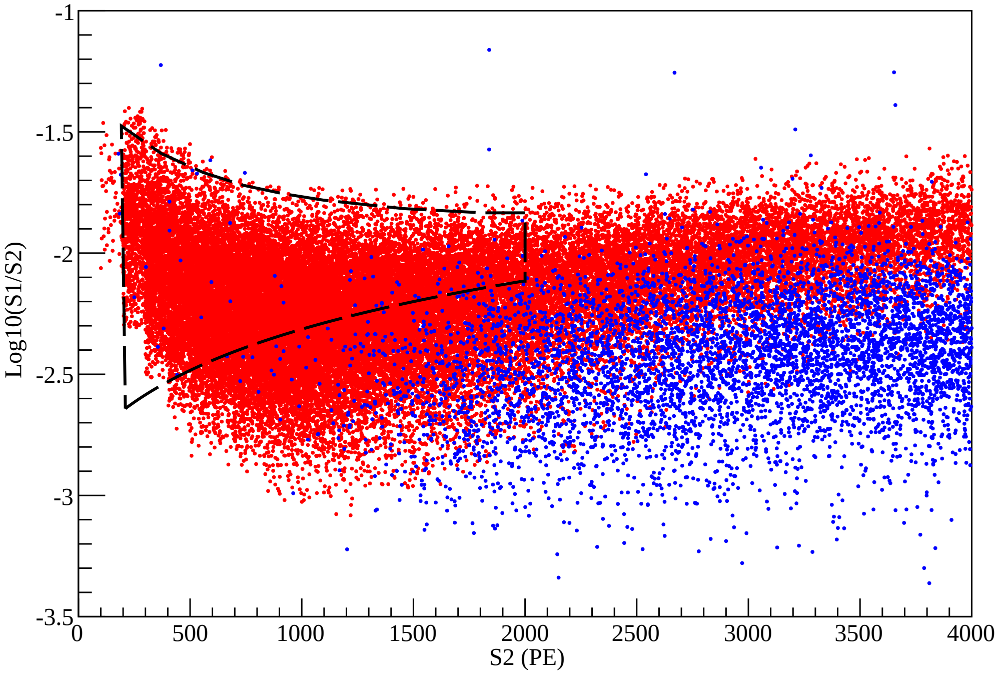

Figure 6.3: Neutron and gamma calibration data in the Log_{10}(S1/S2) versus S2 phase space with a generic signal region to show the vast improvement available to this analysis.

(background) distribution and scaling by the quantity of background events in dark matter data to obtain the proper exposure

$$N_{exp} = \frac{N_{bg}^{sig}}{N_{bg}^{tot}} N_{dm} \tag{6.4}$$

gives the expected background (N_{exp}) for a total number of gamma (N_{bg}^{tot}), background DM (N_{dm}), and signal region gamma events (N_{bg}^{sig}). For the selected signal region from 200 to 2000 PE S2, this gives an expected background of 1.9±0.6 events, where we observe 2 events giving a FC upper limit of 3.915 signal events. The largest difference between using this phase space versus the traditional one is the relaxed condition on S1; previously, we had taken a threshold of 3 PE for the S1 signal, while now we allow any S1 signal with at least a two-fold PMT coincidence. This is allowed because we have quantified the detector efficiency for such signals down to about 1 PE S1 (figure 5.4).

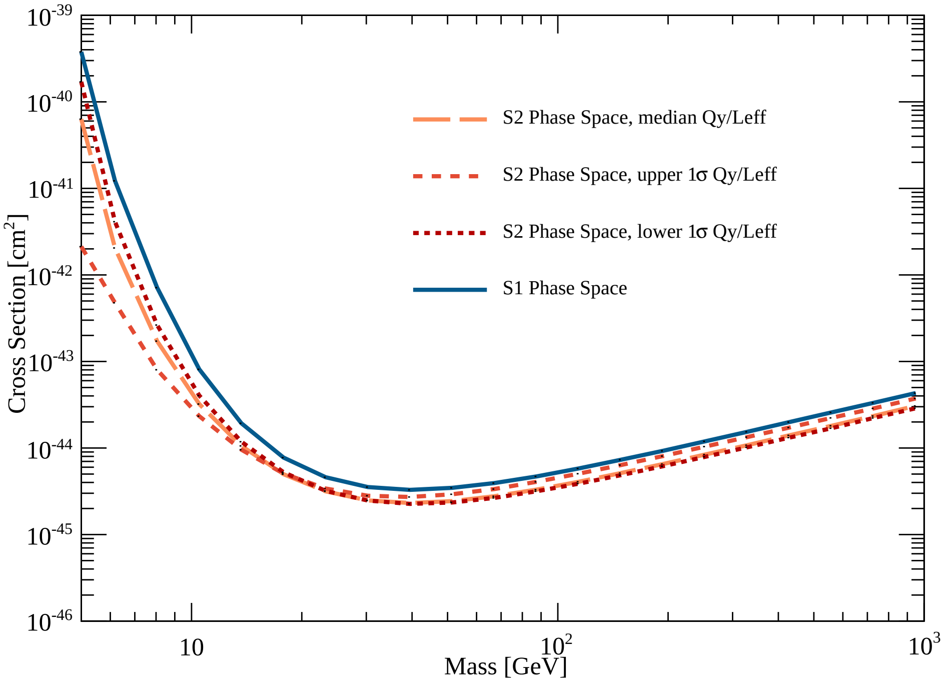

Figure 6.4: 90% CL upper limit on WIMP elastic dark matter cross sections from an analysis using the S2-based phase space with variations in energy scale as parameterized in Chapter 5.

The resulting 90% CL upper limit for this phase space and signal region can be seen in figure 6.4 along with variations of the underlying energy scales for both $\mathcal{L}_{eff}$ and $\mathcal{Q}_y$ simultaneously. As expected, changing the relative scintillation and ionization yields has a large effect on the resulting limit at low energies. Figure 6.5 shows the improvement in the upper limit when changing to the new phase space for three different energy scale conditions of the yields. For lower masses, there is a factor of improvement between 3-8 for below 10 GeV/c^2 and median $\mathcal{L}_{eff}$ and $\mathcal{Q}_y$. Improvement between the phase spaces at higher masses is negligible especially when considering the corresponding FC upper limit on number of signal events (3.915 and 4.915 events, which gives a factor of ~1.25).

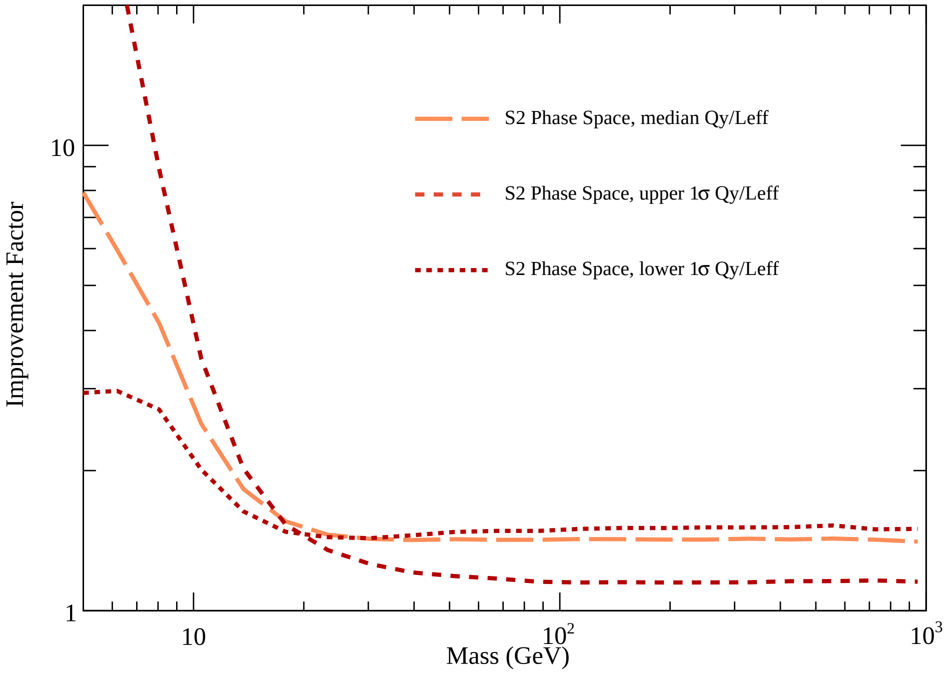

Figure 6.5: Improvement in moving from the traditional S1-based phase space to the S2-based phase space. The gain at low energies is attributed to the acceptance of signals from below the traditional threshold of 3 PE while the variation between the differing input scales has quite a large effect ranging from a factor of 3 to greater than 100 at the lowest WIMP masses considered.

In addition, various other signal regions with similar shapes have been studied, but it was found that the improvement over the current selected one is negligible. Since this region includes the majority of the low mass WIMP distribution as well, changing the region to select a larger portion of the low S2 space only provides a small degree of improvement when considering the 90% CL upper limit. In the profile likelihood analysis, selecting such a signal region (aside from upper and lower thresholds) is unnecessary as the full dataset along the discrimination parameter axis will be included.

6.2 Profile Likelihood

The profile likelihood method is one class of likelihood ratio hypothesis tests where the likelihood is a product of probability density functions defined by

$$\mathcal{L}(\boldsymbol{\theta}|x) = f(x|\boldsymbol{\theta}). \tag{6.5}$$

which gives the likelihood of a set of parameters defining a model, $\boldsymbol{\theta}$, given a fixed outcome or observed data, x. Neyman-Pearson's lemma [122] states that the most powerful test statistic when performing a test between two hypotheses H_0 (null) and H_1 (alternate), which rejects H_1 results from the ratio

$$\lambda = \frac{\mathcal{L}(H_1|x)}{\mathcal{L}(H_0|x)}. \tag{6.6}$$

The power of the test is indicated by calculating a p-value, a probability of observing data with equal or greater incompatibility with H_1, such that H_1 is excluded if the p-value is below a specified threshold (determined by choice of confidence interval). Typically, we can try to reject the background-only hypothesis tested against the background plus signal model in a discovery search or try to reject a hypothesis with background plus signal tested against the background-only hypothesis to set upper limits of signal sensitivity. In these cases, both the denominator and numerator $\mathcal{L}(H_1|x)$ and $\mathcal{L}(H_0|x)$ are highly sensitive to how H_1 and H_0 are specified [123].

A different frequentist significance test uses the profile likelihood test statistic, which modifies this likelihood ratio by taking the denominator (the hypothesis to be tested against) to be the hypothesis using the best-fit model to the data, with numerator maximization against the space of so-called nuisance parameters with fixed parameters of interest for the given hypothesis. These nuisance parameters present in the background and signal models are not known a priori but are instead fitted from data, which results in a loss of sensitivity due to the introduced flexibility of parameterization of systematic effects [124].

The XENON100 profile likelihood technique was first described in [121]. Extensions to the method are presented here, which include the WIMP simulation, the uncertainty for the ionization energy scale, and the change to emphasis on the S2 observable.

6.2.1 The Technique

Suppose there exists a model for the data, which includes both parameters of interest, $\boldsymbol{\mu}$=$(\mu_1, \mu_2, ...\mu_k)$, and additional nuisance parameters, $\boldsymbol{\theta}$=$(\theta_1, ..., \theta_m)$. The likelihood function, $\mathcal{L}$, can then be written in terms of the probability density function $f(x|\boldsymbol{\mu}, \boldsymbol{\theta})$, where x is an independent observation or data set,

$$\mathcal{L}(\boldsymbol{\mu}, \boldsymbol{\theta}|x) = f(x|\boldsymbol{\mu}, \boldsymbol{\theta}). \tag{6.7}$$

In order to construct confidence intervals for the parameters of interest, it is necessary to eliminate, or profile the nuisance parameters away. The profile likelihood method discussed here takes a given hypothesis and attempts to reject it. Statistical power of this method is given by either a sensitivity limit in rejection of a signal hypothesis or a significance for discovery in rejection of a background-only hypothesis.

The likelihood ratio (or profile likelihood) to be employed is defined as

$$\lambda(\boldsymbol{\mu}) = \frac{\mathcal{L}(\boldsymbol{\mu}, \hat{\hat{\boldsymbol{\theta}}})}{\mathcal{L}(\hat{\boldsymbol{\mu}}, \hat{\boldsymbol{\theta}})} \tag{6.8}$$

where the denominator is the likelihood function maximized over the full parameter space and the numerator is maximized only over the space of nuisance parameters for the given hypothesis. The ratio ranges from 0 to 1 ($0 \leq \lambda(\boldsymbol{\mu}) \leq 1$) such that values closer to 1 represent a data set is in good agreement with the model, μ. In comparison to the traditional likelihood ratio, the profile likelihood with the presence of nuisance parameters is broadened over the parameters of interest, expected due to the loss in accuracy from systematic uncertainties [124].

6.2.2 Test Statistic

The test statistic for this method is given by the log of the profile likelihood ratio

$$\tilde{q}_{\mu} = -2\ln\lambda(\boldsymbol{\mu}) \tag{6.9}$$

such that larger values of $\tilde{q}$ signify a larger discrepancy between the data and μ. This test statistic can be used to claim a discovery by rejecting a background-only hypothesis, or to set an upper limit by rejecting a signal hypothesis. Its significance can be quantified through the p-value,

$$p_{\mu} = \int_{\tilde{q}_{\mu,obs}}^{\infty} f(\tilde{q}_{\mu}|H_{\mu})d\tilde{q}_{\mu} \tag{6.10}$$

where f is the the probability distribution function for the given μ hypothesis. The determination of this pdf will be discussed in detail in the next sections and the appendix. One can set a confidence interval at a desired level, α, by solving numerically for interval endpoints (μ_{low} and μ_{high}) above and below $\hat{\mu}$ such that $p_\mu = \alpha$. It is also possible to set one sided confidence upper limits given by μ_{up} for $p_\mu = \alpha$ for an upper tail probability, α.

It is important here to note both μ and $\hat{\mu}$ and how they are interpreted physically. Under these definitions, there is no restriction on the relation between the maximum likelihood estimator (MLE), $\hat{\mu}$, and μ such that values for $\hat{\mu}\geq\mu$ and $\hat{\mu}<\mu$ (both upwards and downwards fluctuations of data) can give similarly low p-values. For both discovery and upper limit sensitivity it will be necessary to modify this definition of $\tilde{q}$.

6.2.2.1 Discovery

Under the background only hypothesis, $\mu = 0$, such that the test statistic is $\tilde{q_0} = -2\ln\lambda(0)$. Then both upwards and downwards fluctuations in the data may be used to reject such a hypothesis. To prevent against systematic errors causing a downwards fluctuation, it is necessary to require that $\hat{\mu} > 0$, such that only observation of signal-like events can reject the background-only hypothesis. The test statistic can then be written as

$$q_0 = \begin{cases} -2\ln\lambda(0) & \hat{\mu} \geq 0 \\ 0 & \hat{\mu} < 0 \end{cases} \tag{6.11}$$

where λ is the profile likelihood ratio defined in equation 6.8. The significance of a discovery is obtained from the probability distribution function, $f(q_0|H_0)$ and quantified using the p-value,

$$p_0 = \int_{q_0,obs}^{\infty} f(q_0|H_0)dq_0 \tag{6.12}$$

such that the integration is carried out from the test statistic obtained from the data set to infinity. The pdf f is under the assumption of a background-only hypothesis and may be obtained approximately using empirical or mathematical methods as in Sections 6.2.2.3 or 6.4.1. The significance of the discovery is given by Z, the number of standard deviations above a Gaussian distributed variable mean with upper tail probability given by the p value as follows

$$Z = \Phi^{-1}(1-p_0) = \sqrt{q_0} \tag{6.13}$$

where Φ^{-1} is the quantile or inverse cumulative distribution for the standard Gaussian. Typically the background-only hypothesis is rejected for significance levels of $Z = 5$ or $p = 2.87 \times 10^{-7}$, but even slightly lesser significances may be interesting and point to hints of a signal. With a sufficient significance, a confidence interval on the parameter of interest may be constructed with the desired coverage as shown in 6.1.

6.2.2.2 Upper Limits

In general, we are interested in the expected significance of an experiment which reflects the effects from the underlying uncertainties present, not just the significance from a single experiment. This is performed by generating pseudoexperiments with varying input nuisance parameters using the WIMP and background models of XENON100 to cover the majority of the available parameter space.

It is necessary to understand fluctuations of the background in the data, which could lead to $\hat{\mu}>\mu$. For such a situation where the background fluctuates upwards, the data we have would be more signal-like than the hypothesis (H_μ), which is the opposite of what is needed for an upper limit. The test statistic for setting upper limits is then

$$q_\mu = \begin{cases} -2\ln\lambda(\mu) & \hat{\mu} \leq \mu \\ 0 & \hat{\mu} > \mu \end{cases} \tag{6.14}$$

where we now take $q_\mu = 0$ for $\hat{\mu} > \mu$. It may seem that setting $\mu = 0$ would lead to the same conclusion as in the discovery section above, but in contrast to equation 6.11, that is not the case as downward fluctuations in data require that q_0=0 for $\hat{\mu} < 0$ and upward fluctuations require $q_\mu = 0$ for $\hat{\mu} > \mu$. The difference between the two lies in the physical meaning of the hypothesis that is trying to be rejected.

The significance of an upper limit can be characterized by a p-value

$$p_\mu = \int_{q_\mu,obs}^{\infty} f(q_\mu|H_\mu)dq_\mu \tag{6.15}$$

where the confidence level of the upper limit on the signal is given by $\alpha = 1 - p_\mu$ and the pdf is under the assumption of a signal plus background hypothesis. This fully frequentist formulation called CL_{s+b} sets sensitivity bounds on the signal plus background hypothesis ($p_\mu = p_{s+b}$). If we are instead interested sensitivity of the signal-only hypothesis, it is necessary to protect against background fluctuations, which may produce additional signal-like data. A modified p-value uses the background probability $1 - p_b$

$$1 - p_b = \int_{q_{\mu,obs}}^{\infty} f(q_\mu|H_0)dq_\mu \tag{6.16}$$

with the new significance described by $p_s = \frac{p_{s+b}}{1-p_b}$ to provide a confidence level on the signal-only hypothesis. This modification to using the so-called CL_s technique [125] results in a conservative sensitivity, which considers the problems evident in a truly frequentist analysis in which uncertainties in background or increased background expectation (such as overlapping signal and background distributions) may improve the apparent sensitivity (as in FC). However, this CL_s analysis gives only an approximate confidence interval of the signal-only hypothesis due to the presence of background in the experiment and thus does not correspond to a true physical ensemble such that is no longer fully frequentist. The choice is made here to use the CL_s technique to take a conservative approach.

6.2.2.3 Asymptotic Distributions for Discovery and Upper Limit Test Statistics

To obtain a p-value and the corresponding significance for a given hypothesis, it is necessary to understand the underlying distributions of the profile likelihood test statistics for the large sample approximation. Following the methodology of both Wilks [126] and Wald [127], asymptotic analytic formulae from the likelihood ratio are easily derived even for cases where the hypothesis being tested is slightly different from that in data. This latter approximation is a necessary conservative measure to protect against signal-like fluctuations of background, which may artificially increase the sensitivity of an experiment (see Appendix A).

6.3 XENON100 Likelihood Procedure

The XENON100 likelihood function is a product of probability density functions that characterize the parameters of interest, or in this case a single parameter, σ

the cross-section, and nuisance parameters, which are necessary to describe the uncertainties in the models for the hypotheses being tested. The full likelihood function for a given fixed mass, m_χ, can be written in terms of the cross section and nuisance parameters ($\boldsymbol{\theta}$=$(N_b, \boldsymbol{\epsilon_s}, \boldsymbol{\epsilon_b}, \mathcal{L}_{eff}, \mathcal{Q}_y, \eta_s, \eta_c, v_{esc})$)

$$\begin{aligned}\mathcal{L}(\sigma, \boldsymbol{\theta}) = &\mathcal{L}_1(\sigma, N_b, \boldsymbol{\epsilon_s}, \boldsymbol{\epsilon_b}, \mathcal{L}_{eff}, \mathcal{Q}_y, \eta_s, \eta_c, v_{esc}; m_\chi) \\ &\times \mathcal{L}_2(\boldsymbol{\epsilon_s}) \times \mathcal{L}_3(\boldsymbol{\epsilon_b}) \\ &\times \mathcal{L}_4(\mathcal{L}_{eff}) \times \mathcal{L}_5(\mathcal{Q}_y) \\ &\times \mathcal{L}_6(\eta_s) \times \mathcal{L}_7(\eta_c) \\ &\times \mathcal{L}_8(v_{esc})\end{aligned} \tag{6.17}$$

where the likelihood has been broken down into probability functions for the physical model ($\mathcal{L}_1$) and for the statistical and systematic uncertainties of the nuisance parameters used to constrain the model ($\mathcal{L}_2$-$\mathcal{L}_8$). The nuisance parameters included in this construction are the total number of background events N_b, the escape velocity (v_{esc}), probabilities for signal and background ($\boldsymbol{\epsilon_s}$ and $\boldsymbol{\epsilon_b}$), energy conversion from keVr to S1 and S2 ($\mathcal{L}_{eff}$ and $\mathcal{Q}_y$ determined in Chapter 5), and acceptances from single scatter selection and quality cuts (η_s and η_c).

6.3.1 The XENON100 Model

The first likelihood term in equation 6.17 describes the physical model for a given set of experimental data on which the statistical test is built. The model is described by the expected signal population generated using the WIMP Monte Carlo presented in Chapter 5 and the expected background distribution derived from gamma calibration data taken periodically over the period of the Run10 dark matter data set.

The WIMP model is generated by randomly sampling recoil energies from the given WIMP mass energy spectrum. Each recoil energy is converted into an S1 and S2 value through the $\mathcal{L}_{eff}$ and $\mathcal{Q}_y$ with a Poisson process for photostatistics and a gaussian smearing due to PMT resolution (Chapter 5). The single scatter selection and threshold criteria are applied to this energy deposit, both S1 coincidence and S2 threshold cuts, as well as the quality cut efficiency parameterized in two dimensions. The resulting event distribution is the signal model used in the likelihood method.

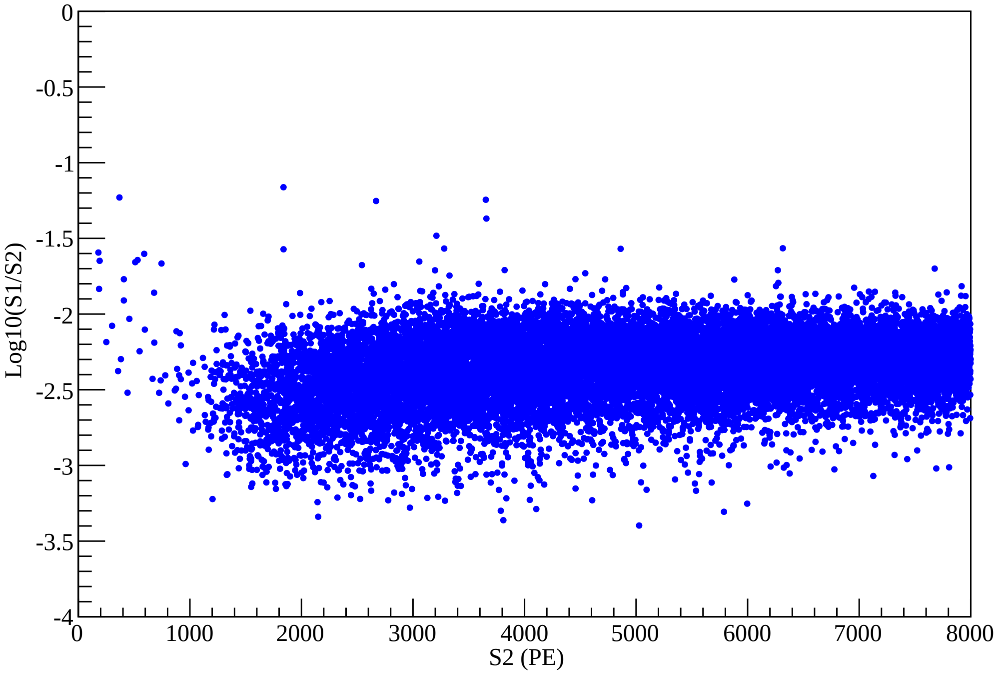

Figure 6.6: The background model in the Log_{10}(S1/S2) versus S2 phase space from the gamma calibration data.

The background model used for the likelihood analysis is generated exclusively from gamma (^{60}Co and ^{232}Th) calibration data taking runs. Due to the lack of

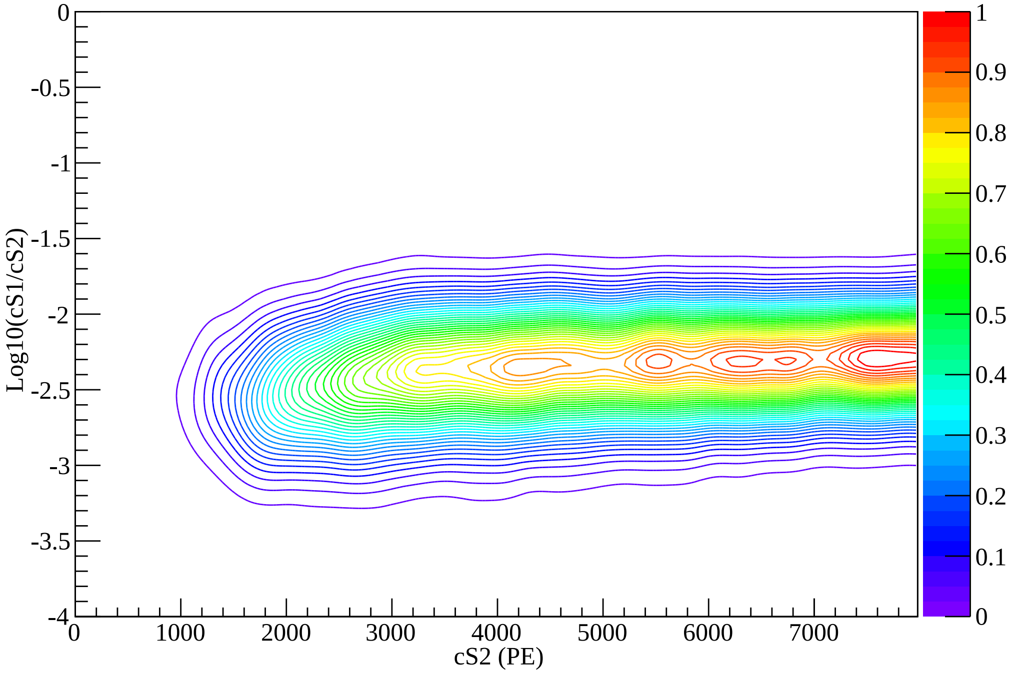

Figure 6.7: The background model in the $\mathrm{Log}_{10}(\mathrm{S1/S2})$ versus S2 phase space after being smoothed.

statistics in the gamma calibration data in regions of low S2, the background model is obtained from the distribution using the ROOT smoothing histogram function based on the k5a kernel algorithm similar to raster graphics smoothing. This allows the previously sparse distribution for very low S2 values (figure 6.6) to be smoothed over the bulk of the phase space. The resulting distribution shown in figure 6.7 is the background model for the profile likelihood. This smoothing process is performed instead of using a dedicated background Monte Carlo simulation due to lack of knowledge of the electronic recoil energy scale and conversion to observables at these low energies.

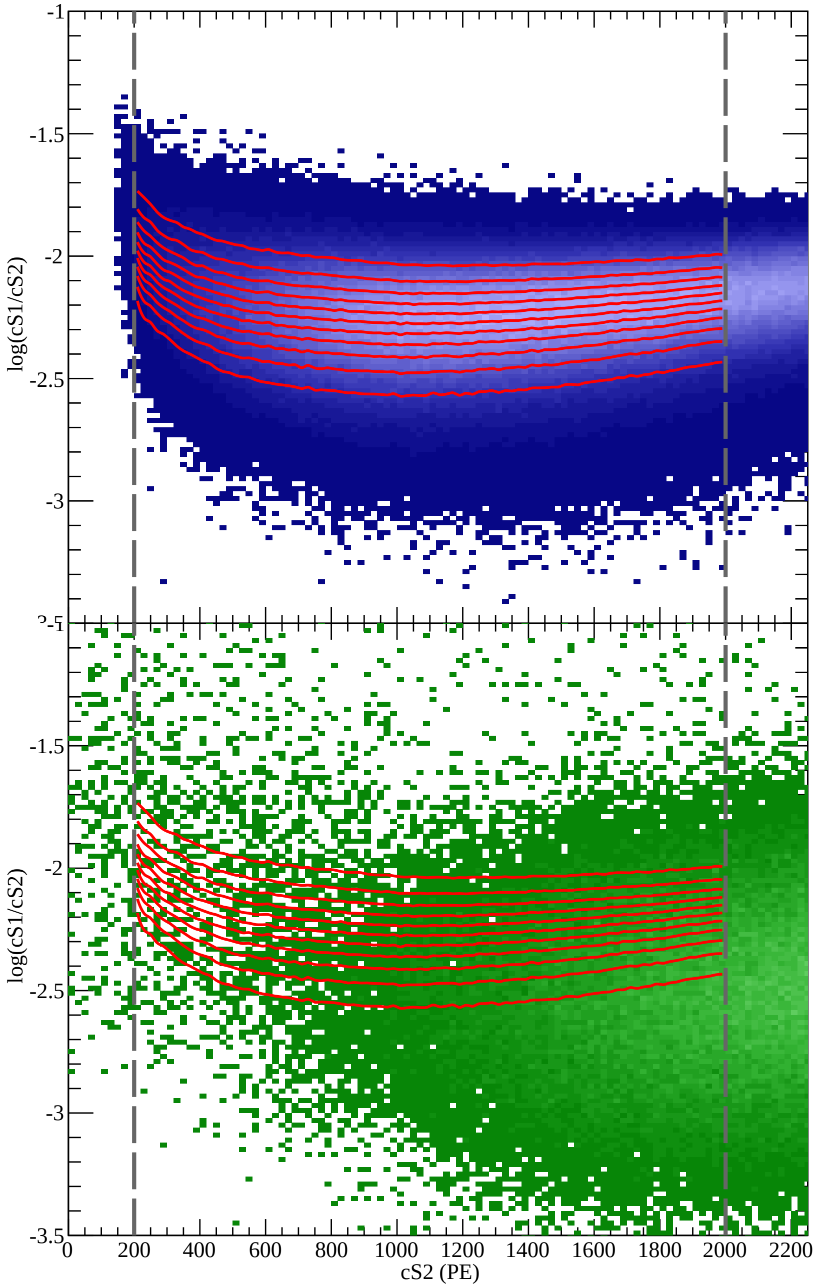

Figure 6.8: *Top Panel*: 50 GeV simulated WIMP signal split into bands of equal probability in S2 vs Log(S1/S2) phase space for given default nuisance parameters and $5{\times}10^6$ simulated events. *Bottom Panel*: Background distribution from gamma calibration data with the bands obtained from slicing the WIMP simulation data overplotted.

6.3.1.1 Band Construction

To construct a likelihood that takes advantage of the inherent discrimination provided by the Log(S1/S2) parameter and S2 itself, a set of bands in the S2 vs Log(S1/S2) phase space over the range 200-2000 PE (1.61 - 20.1 keV$_r$) in S2 is generated by binning and slicing the expected signal population due to a WIMP signal of a given mass. The lower threshold is determined by the trigger efficiency and high bound is determined by the rising background distribution. An example in figure 6.8 shows a 50 GeV WIMP simulation and background models, where the signal distribution has been sliced into in twelve equal sections.

In the following, $m^i_{s/b}$ are the number of signal or background events in the ith band and $M_{s/b}$ are the total number of events of each in the full model. For each band, the proportion of signal events, $\epsilon^i_{s0} = m^i_s/M_s$, and the proportion of background events, $\epsilon^i_{b0} = m^i_b/M_b$ contains information about the discrimination parameter along the Log$_{10}$(S1/S2) axis in each region, while expected signal and background spectra for each band are used on an event by event basis to discriminate along the S2 axis. The signal and background spectra are the projections along the X axis of the total events in each band. An example for the spectra can be seen in figure 6.9 for both signal and background. These have been normalized to have a total probability of unity over the energy range of interest. Typically, the bands have the same spectral shape with the exception of the top band in the Log$_{10}$(S1/S2) versus S2 phase space, which has a flatter contribution at lower values of S2. Another spectral example can be seen in figure 6.10 for a 8 GeV/c^2 WIMP model, where the background and signal models well separately along S2.

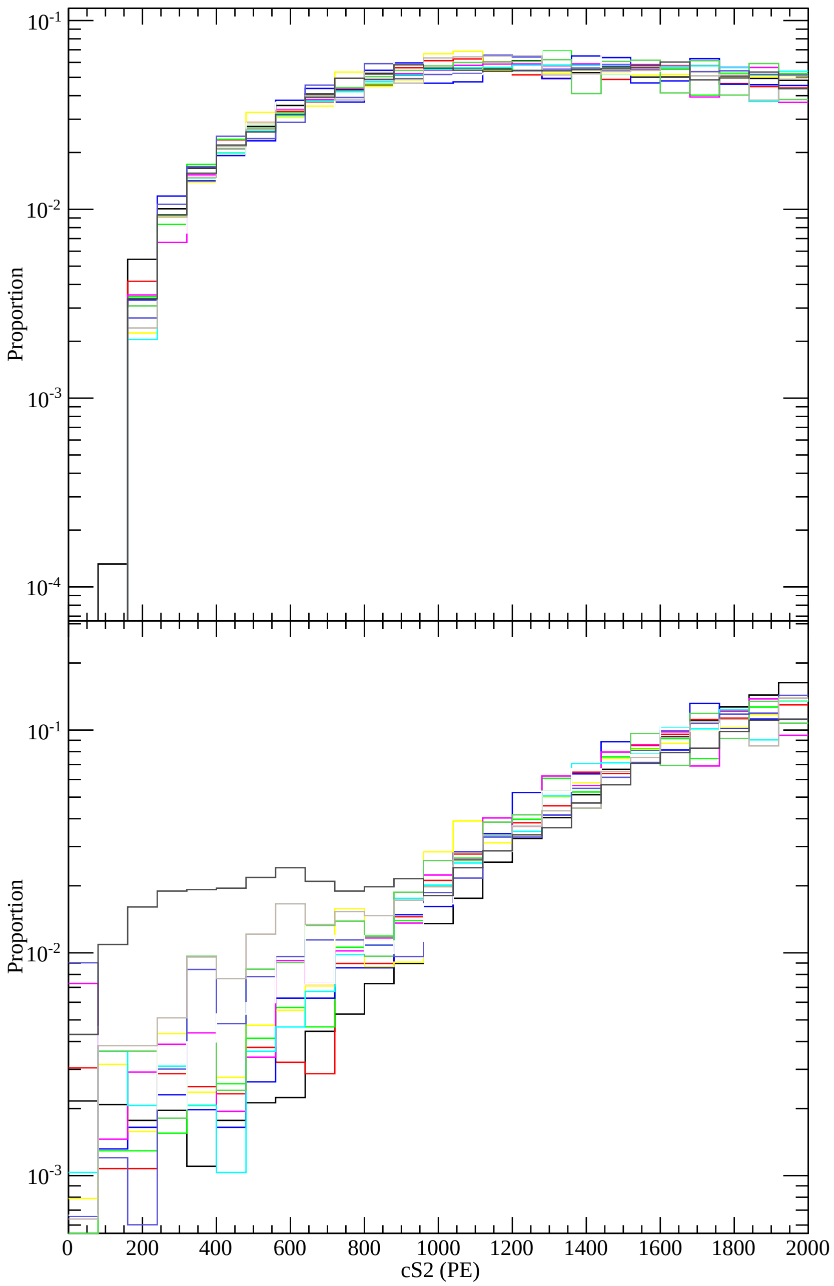

Figure 6.9: *Top Panel*: 50 GeV/c^2 simulated WIMP signal projected along S2 axis. *Bottom Panel*: Background distribution projected along S2 axis. The rising background for higher S2 values is the motivation for ending the signal region at 2000 PE.

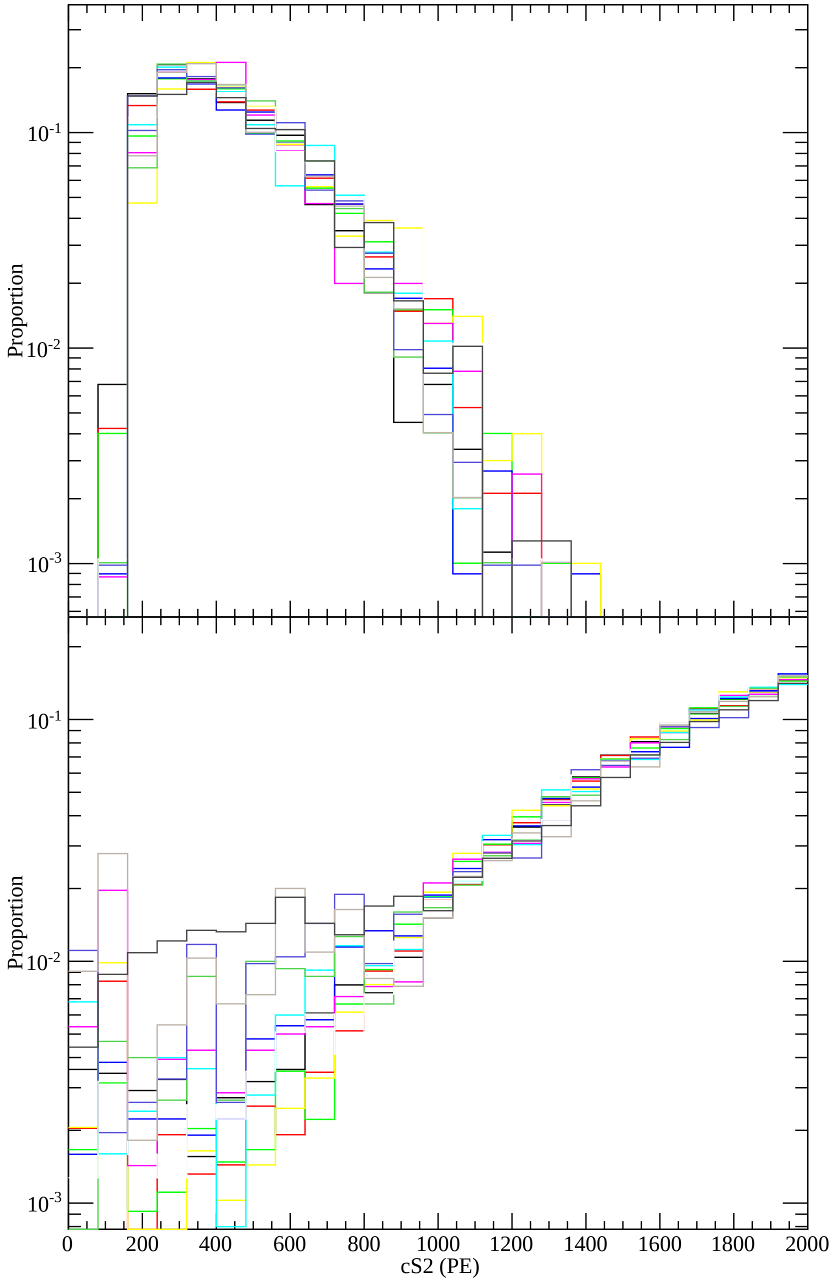

Figure 6.10: *Top Panel*: 8 GeV simulated WIMP signal projected along S2 axis. *Bottom Panel*: Background distribution projected along S2 axis.

6.3.1.2 Pseudoexperiment Generation

Given the signal and background models, pseudoexperiments may be generated to both test the performance of the likelihood function and determine the nominal distributions needed for the profile likelihood ($f(q_\mu|H_\mu)$ for example). The latter point is required for determining possibilities for signal-like fluctuations from background-only datasets. Additionally it is necessary to prove the statistical power of the method by using a sample of datasets generated under a hypothesis being tested against itself to show the resulting test statistic distribution approaches a chi-squared with one degree of freedom.

The pseudoexperimental datasets of interest are then background-only and signal plus background datasets. For the XENON100 Run 10 data, the real data set has a total of 27 events between the specified 200-2000 PE range in S2. The background-only datasets thus have 27 events in the same energy range sampled randomly from the background model. For signal plus background datasets, an arbitrary number of two signal events sampled from the designated WIMP mass simulated distribution were added to a background population of 25 events. The statistical and systematic variation of these datasets gives the range of expected sensitivity over the systematic uncertainties of the nuisance parameters.

Several examples of pseudoexperiments can be seen in figure 6.11. Due to the slight overlap between background and signal populations, especially for higher WIMP masses, there exists the probability of a background event to look like a signal event, which in effect would decrease sensitivity resulting in a more conservative limit. In the figure, the bottom row shows examples of having two 50 GeV/c^2 WIMP simulated signal events and the difficulty of distinguishing signal from background of the corresponding underlying distributions. For the middle row, for a 10 GeV/c^2 WIMP, the situation becomes slightly clearer as the distributions become further separated. However, it is important to note the large variation even within the background model, which characterizes the power of this method through the systematic variation of thousands of pseudoexperiments.

6.3.1.3 Likelihood Function

With the background and signal models characterized, the resulting likelihood function can be written as follows

$$\mathcal{L}_1 = \prod_{i=1}^{N} \mathrm{Poiss}(n_i | \epsilon_b^i N_b + \epsilon_s^i N_s) \times \left(\prod_{j=1}^{n_i} \frac{\epsilon_b^i N_b f_b^i(\mathrm{S2}_j) + \epsilon_s^i N_s f_s^i(\mathrm{S2}_j)}{\epsilon_b^i N_b + \epsilon_s^i N_s} \right) \tag{6.18}$$

where N is the total number of bands, n_i is the experimental or pseudoexperimental data in the ith band, $\mathrm{S2}_j$ is the S2 of an event in data, and f_s and f_b are the signal and background spectra determined from the band projections. The rest of the likelihood parameters are $N_s \propto \sigma_\chi f(\mathcal{L}_{eff}, \mathcal{Q}_y, v_{esc})$, which contains the parameter of interest, and the other nuisance parameters. N_s is primarily determined by simulating a large number of events at a known cross section for the given other parameters and then scaling to the cross section of interest. The Poisson distribution in the first product compares the total data in a band, n_i, to the expected amount from N_s and N_b, and is the typical likelihood term for a counting experiment. The second product then relates the S2 of an event to the spectral shape of both signal and background in the band.

6.3.2 Nuisance Parameters

The nuisance parameters of this likelihood construction can be separated into the statistical variation of the model datasets, $\boldsymbol{\epsilon_b}$, $\boldsymbol{\epsilon_s}$, and N_b, and the physical or detector-specific variables with parameterized systematic uncertainties, the

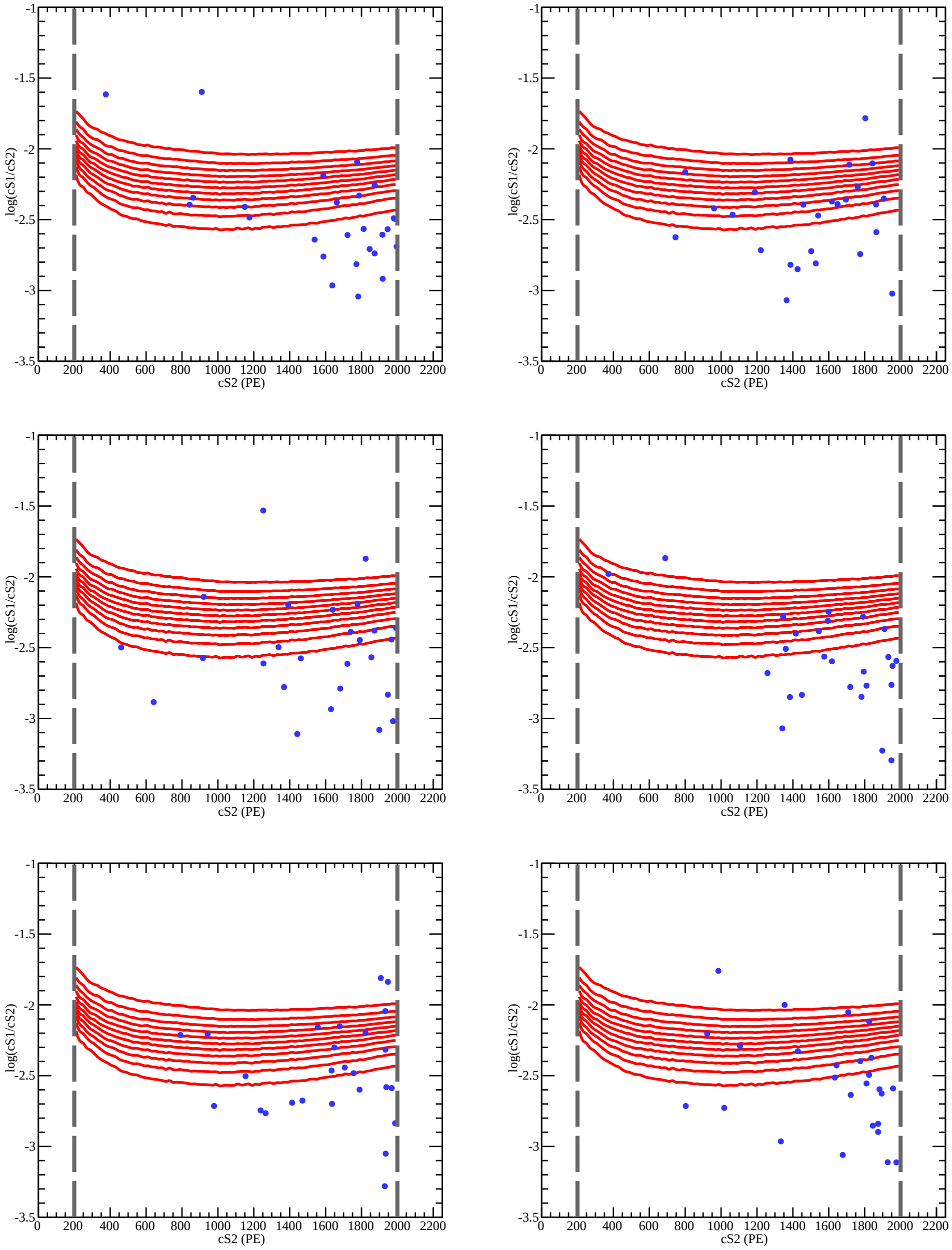

Figure 6.11: Various pseudoexperiment datasets for background and background plus signal. *Top Row:* Two different background-only datasets simulated from the smoothed background model of calibration data. *Middle Row:* 10 GeV/c^2 WIMP signal plus background generated randomly from the WIMP model and background model. *Bottom Row:* 50 GeV/c^2 WIMP signal plus background.

escape velocity, energy scales, and acceptances.

6.3.2.1 Model Variations

The true values of the probability of signal and background proportion in each band are parameters that define the underlying model distributions in the $\mathrm{Log}_{10}(\mathrm{S1/S2})$ versus S2 phase space. The likelihood terms due to these probabilities constrain the models to follow a poisson distribution (due to limited statistics) in each of the bands given by the product of $\epsilon^i M^i$. The background and signal models can be combined as follows

$$\mathcal{L}_{stats} = \mathcal{L}_2(\boldsymbol{\epsilon_s}) \times \mathcal{L}_3(\boldsymbol{\epsilon_b}) = \prod_{i=1}^{N} \mathrm{Poiss}(m_s^i|\epsilon_s^i M_s) \prod_{i=1}^{N} \mathrm{Poiss}(m_b^i|\epsilon_b^i M_b) \tag{6.19}$$

where the m^i's are the number of events of the model in a given band i.

6.3.2.2 Energy Scale Uncertainties

At low masses, the biggest systematic uncertainty in the experiment lies with the energy scales, namely the relative scintillation efficiency, $\mathcal{L}_{eff}$, and the ionization yield, $\mathcal{Q}_y$. Following the uncertainty parameterization shown in the previous chapter, the likelihood term for both $\mathcal{L}_{eff}$ and $\mathcal{Q}_y$ can be written as

$$\mathcal{L}_E = \mathcal{L}_4(\mathcal{L}_{eff}(t_{\mathcal{L}})) \times \mathcal{L}_5(\mathcal{Q}_y(t_{\mathcal{Q}})) = \exp(-\frac{t_{\mathcal{L}}^2}{2})\exp(-\frac{t_{\mathcal{Q}}^2}{2}). \tag{6.20}$$

The nuisance parameters that characterize the energy scales, $t_{\mathcal{L}}$ and $t_{\mathcal{Q}}$, are distributed as gaussians with zero mean and unit variance, where $t = 0$ is the median $\mathcal{L}_{eff}$ or $\mathcal{Q}_y$ and the one and two sigma bands are shown in figures 6.12 and 6.13.

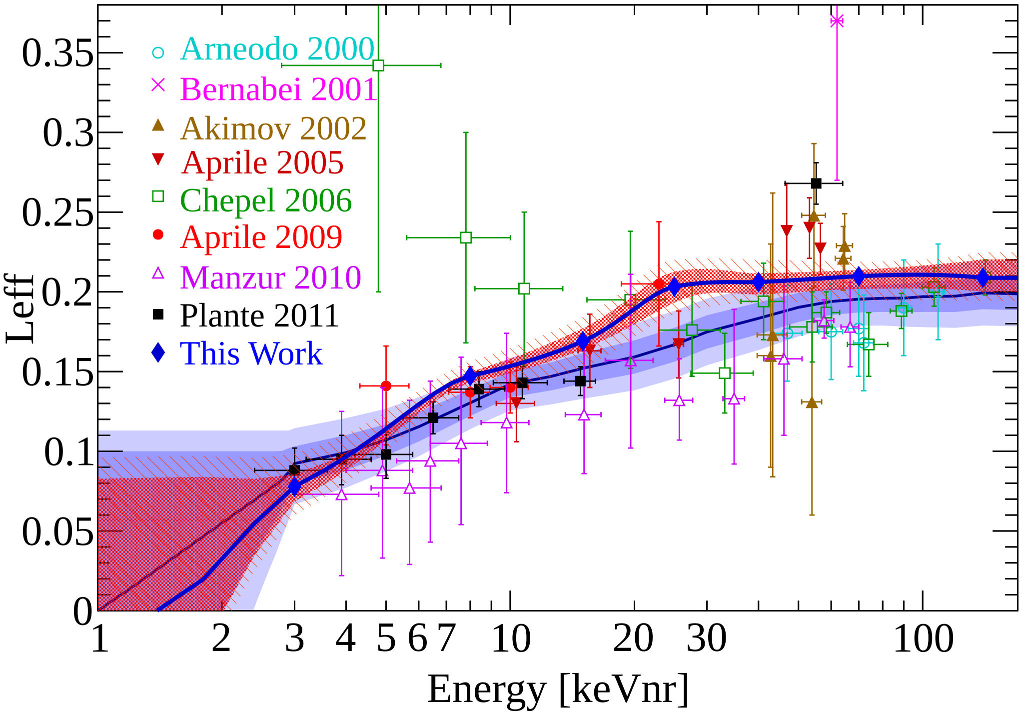

Figure 6.12: Relative scintillation yield, $\mathcal{L}_{eff}$, with parameterized uncertainties from the fitting procedure versus the nuclear recoil energy. The lowest spline point has increased uncertainty, similar to what was done for the XENON100 uncertainty parameterization. Direct measurements of the scintillation yield are plotted as well.

6.3.2.3 Acceptance Uncertainties

The acceptance uncertainties for both the selection criteria and quality cuts are both modeled as gaussians using an uncertainty of 5% from the nominal values as presented in the previous chapters. The value is specifically chosen to be a conservative estimate for the uncertainty at the cost of broadening peak of the final result. The resulting likelihood function term for each of the selection and quality acceptances are

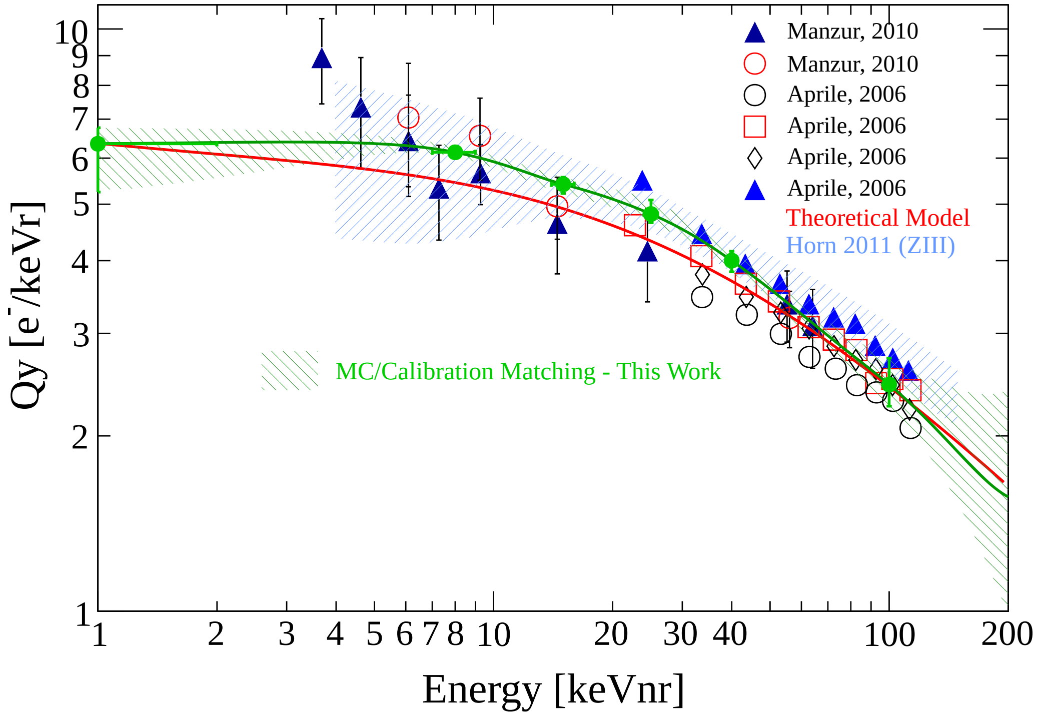

Figure 6.13: I

onization yield, $\mathcal{Q}_y$, with statistical and spline fitting uncertainties obtained from the nonlinear minimization] Ionization yield, $\mathcal{Q}_y$, with statistical and spline fitting uncertainties obtained from the nonlinear minimization. Efficiency and $\mathcal{L}_{eff}$ uncertainties are not included here because they are included separately in the likelihood construction.

$$\mathcal{L}_{acc} = \mathcal{L}_6(\eta_s(t_s)) \times \mathcal{L}_7(\eta_c(t_c)) = \exp(-\frac{t_s^2}{2})\exp(-\frac{t_c^2}{2}) \tag{6.21}$$

where the contributions to the likelihood are taken to be gaussians with zero mean and unit variance with variables t_s and t_b to describe the nuisance parameters for the acceptance. When these variables are zero, the corresponding acceptance is the measured acceptance. For $t = \pm 1$, the acceptance is then $\eta = \eta_0 \pm 5\%$ as expected.

In this profile likelihood analysis, the uncertainties due to acceptance and energy scale are taken to be independent even though it was previously shown in Chapter 5 that they are in fact correlated. To stay on the conservative side for this analysis, the correlation is ignored.

6.3.2.4 Astrophysical Uncertainty

The last nuisance parameter to be considered is the local escape velocity, which is constrained by a sample of high velocity stars [128] and results from a likelihood based analysis can be seen in the distribution in figure 6.14. The 90% confidence interval for this distribution has a median of 544 km/s and ranges from 498 km/s to 608 km/s.

6.3.3 Minimization Method

The likelihood minimization procedure employs the MIGRAD method of the MINUIT package [129] embedded in the ROOT framework. MIGRAD is a first-derivative based minimization technique that uses inexact line search, and a stable metric updating scheme. It begins by varying all the parameters individually followed by a nonlinear mixing of all variables based on the Jacobian and repeats the procedure until a certain tolerance is achieved or the number of maximum calls are performed.

The two types of minimizations performed are for the likelihood maximized over the full parameter space, which makes use of the maximum likelihood estimators, and for the conditional likelihood in which the parameter of interest, the cross section, is fixed at a designated value, while the likelihood function

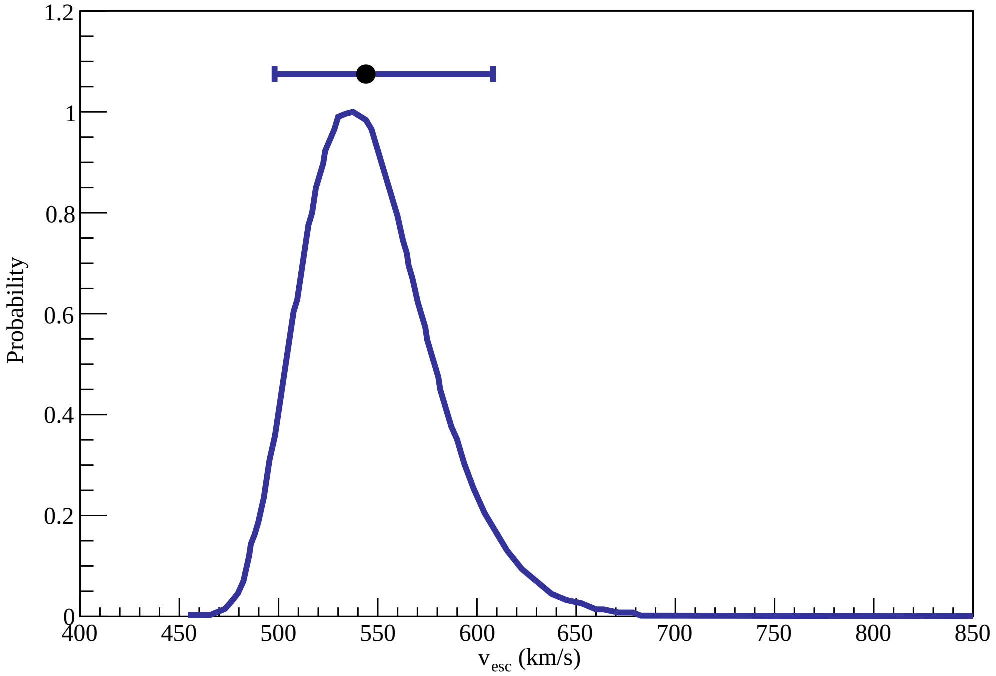

Figure 6.14: WIMP escape velocity as determined by a sample of high velocity stars from the Rave survey. The underlying assumptions include a cosmological disk galaxy simulation with a shape velocity parameter k, which determines the shape of the distribution near v_{esc}. The bar at the top shows the 90% confidence interval for the escape velocity. Plot modified from [128].

is maximized over the remaining nuisance parameter space. There are 31 total parameters in this formulation, some of which can be simplified in computation by replacing their values with the expressions for the maximum likelihood estimators. In the following, ignoring the factorials of the poisson, the log likelihood can be written as

$$\begin{aligned}\ln\mathcal{L} = {} & \sum_i (n_i \ln(x_i) - x_i) + \sum_i \sum_j \frac{\epsilon_b^i N_b f_b^i(S2_j) + \epsilon_b^i N_b f_b^i(S2_j)}{x_i} \\ & - \sum_i \sum_j \ln(x_i) + \sum_i m_b^i \ln(\epsilon_b^i M_b) + \sum_i m_s^i \ln(\epsilon_s^i M_s) \\ & - \sum_i \epsilon_b^i M_b - \sum_i \epsilon_s^i M_s\end{aligned} \tag{6.22}$$

where $x_i = \epsilon_b^i N_b + \epsilon_s^i N_s$. The maximum likelihood estimators are given by maximization of the likelihood as follows

$$\begin{aligned}\left.\frac{\partial \ln\mathcal{L}}{\partial N_s}\right|_{\hat{N}_s} & = 0 \\ & = -1 + \sum_i \sum_j \frac{\epsilon_s^i f_s^i(S2_j)}{\epsilon_b^i N_b f_b^i(S2_j) + \epsilon_s^i N_s f_s^i(S2_j)} && (6.23) \\ \left.\frac{\partial \ln\mathcal{L}}{\partial \epsilon_s^i}\right|_{\hat{\epsilon_s^i}} & = 0 \\ & = \sum_i \sum_j \frac{N_s f_s^i(S2_j)}{\epsilon_b^i N_b f_b^i(S2_j) + \epsilon_s^i N_s f_s^i(S2_j)} + \sum_i m_s^i \frac{1}{\epsilon_s^i} - N_s - M_s && (6.24)\end{aligned}$$

with similar equations for the background quantities N_b and ϵ_b^i. Adding together the equations for N_b and N_s results in the following relation between the estimators

$$\hat{N}_s + \hat{N}_b = \sum_i n_i = N_{total}. \tag{6.25}$$

Combining the other two equations for the background and signal probabilities gives

$$(\hat{N}_s + M_s)\hat{\epsilon_s^i} + (\hat{N}_b + M_s)\hat{\epsilon_b^i} = m_b^i + m_s^i + n_i. \tag{6.26}$$

These equations for the estimators help to reduce the computation necessary of the MINUIT likelihood minimization process in ROOT.

The minimization process proceeds as follows. Default initial parameters are obtained through the nominal values of the nuisance parameters in the full likelihood model as the asymptotic-limiting distributions are only weakly dependent upon these input parameters [124]. Then for each minimization step, a new model is generated according to the new nuisance parameters (as guided by the MIGRAD procedure) and the resulting likelihood value is computed. We first obtain the maximum likelihood estimators over for the full parameter space, which gives the unconditional likelihood value. Once this is known, the desired test statistics can be found by holding the parameter of interest at fixed values, and maximizing the likelihood over the nuisance parameter space. The following section contains the full details for the various test statistics required.

6.4 Two Dimensional Profile Likelihood Analysis

The first steps for this analysis are to establish the necessary distributions to correct for the proper coverage while staying slightly on the conservative side. This means both obtaining the expected half-χ^2 distribution for the datasets under their generated hypotheses ($f(q_\sigma|H_\sigma)$ and $f(q_0|H_0)$) and the unique distributions of the signal characteristics of background-only datasets ($f(q_\sigma|H_0)$).

After verifying and obtaining the needed distributions, the Monte Carlo generated pseudoexperiments are then used to find the expected sensitivity of the XENON100 experimental run as well as the upper limit for the true dataset by testing the signal hypothesis. The discovery potential for the experiment is tested through the background-only hypothesis. *A priori*, it is chosen to test both signal and background hypotheses, which avoids any bias evident in flip-flopping to gain aggressively in either direction.

6.4.1 Asymptotic Distributions from Monte Carlo

The set of distributions to consider for upper limits are for a non-zero parameter of interest for both the signal and background-only hypotheses. In section 6.2.2.3, it was shown that the probability distribution for a test statistic of a given true hypothesis, $f(q_\sigma|H_\sigma)$, will result in a half-χ^2 distribution with one degree of freedom for a large number of trials. Figure 6.15 shows one such example for 10 GeV/c^2 with 500 sampled test statistics for Monte Carlo generated experiments under the signal hypothesis with two signal and 25 background events.

It is also necessary to test the background-only hypothesis for the same fixed parameter of interest $f(q_\sigma|H_0)$. In general, this distribution can be described by the asymptotic weight parameter μ', but it has been decided here to use exclusively Monte Carlo generated background-only datasets. For each given WIMP mass, a separate distribution is produced, which depends on how signal-like a background-only dataset may be. At lower masses, the distributions are slightly separated as evident in figure 6.15, which shows the respective distributions for a 10 GeV/c^2 WIMP and the discriminatory power available for this mass region. However, for higher WIMP masses, the crossover may be significantly larger than at low masses as the signal and background distributions begin to increasingly overlap. Figure 6.16 shows an example representative of the majority of WIMP masses (recall figure 1.9 for different mass spectra).

Looking back on the example Monte Carlo datasets shown in section 6.3.1.2, the power of this method is readily evident, especially for low mass WIMPs due to the separation between data and background distributions.

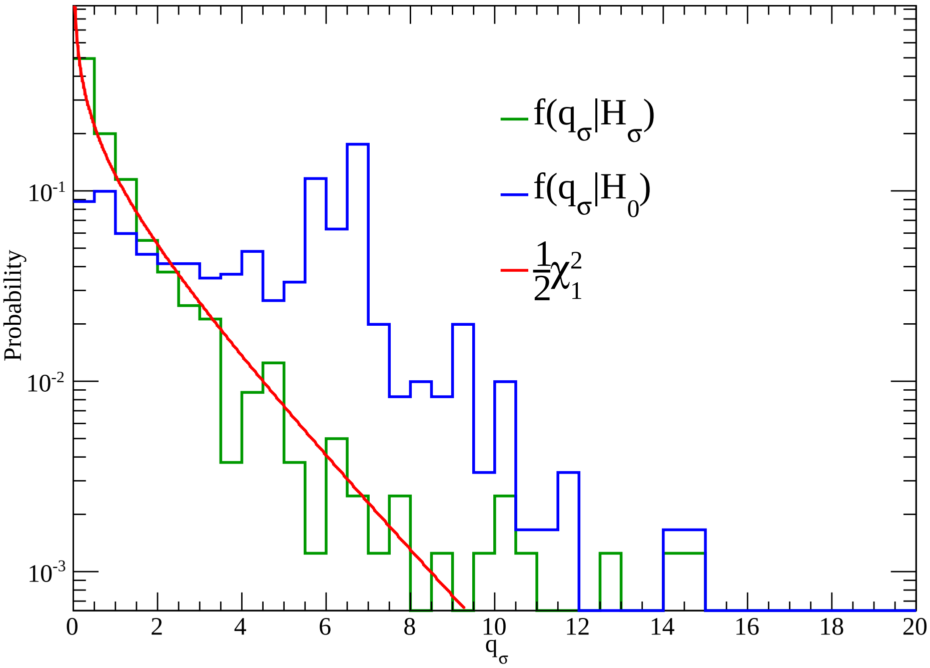

Figure 6.15: Test statistic (q_σ) distribution for 10 GeV/c^2 under both signal plus background (H_σ) and background-only (H_0) hypotheses with a $1/2\chi^2$ function with one degree of freedom. The overlap between the two test statistic distributions is split much more visibly than in the 50-500 GeV/c^2 case.

6.4.2 Expected Sensitivity

With the asymptotic probability distributions, upper limits with the proper coverage can be generated for a set of background-only datasets using the modified p-value, p'_s. For each experiment, we look for a 90% confidence level upper limit to a specified tolerance ($|p'_s - \alpha| < 0.005$) by using a binary search from the maximum likelihood estimator, $\hat{\sigma}$, to an upper threshold of two orders of magnitude larger. We restrict our search to physically-allowed values for the cross section ($\sigma > 0$). This process takes on the order of ten iterations to reach the given

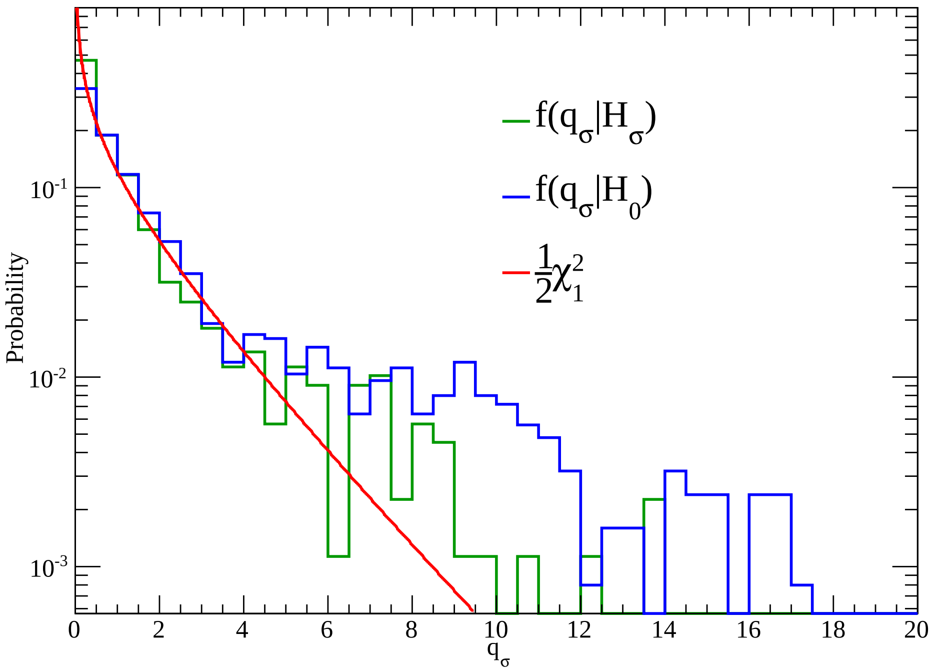

Figure 6.16: Test statistic (q_σ) distribution for 500 GeV/c^2 under both signal plus background (H_σ) and background-only (H_0) hypotheses with a $1/2\chi^2$ function with one degree of freedom. The overlap between the two test statistic distributions (similar down to 50 GeV/c^2) signifies a decreasing ability to discriminate between signal and background events.

tolerance.

An example for a given mass can be seen in figure 6.17, where the expected senstivity bands are given by the quantiles of the distribution for both one and two sigma for several hundred pseudo background-only experiments. This spread over the interaction cross section is a result of the various systematics present in the analysis, a majority of which stems from the Poisson statistics sampling from the background model as shown in figure 6.11.

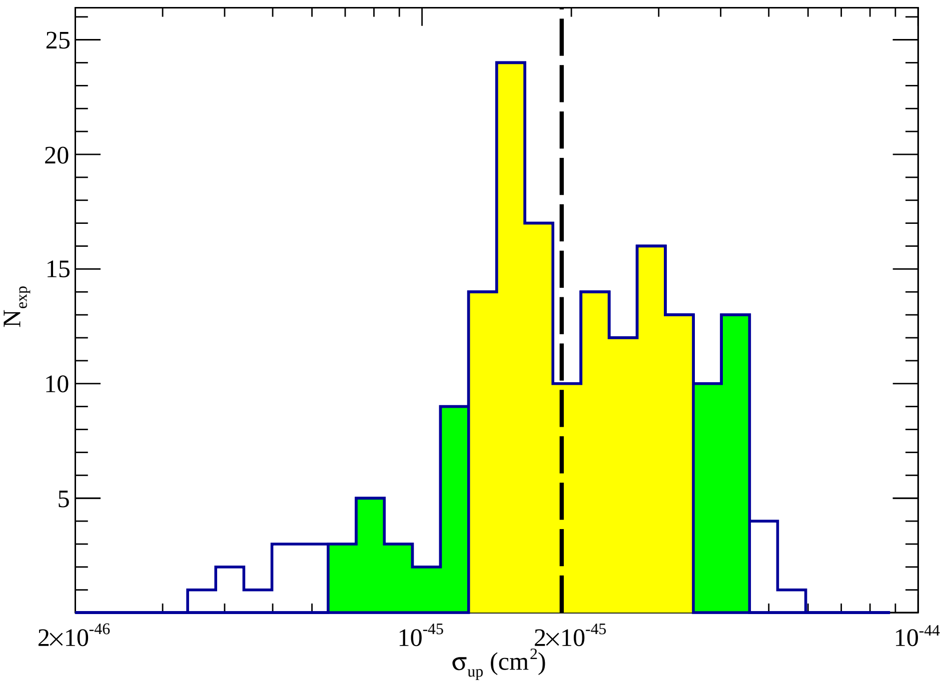

Figure 6.17: Upper limit distribution for 110 GeV/c^2 WIMP obtained from background-only pseudoexperiments. The 1σ and 2σ bands (68% and 95%) can be seen in *yellow* and *green* and the median significance is denoted by the *black-dotted* line.

For each of twenty masses along evenly spaced along the $\log M_\chi$ axis, the expected sensitivity is obtained and can be shown in the full phase space as in figure 6.18. The variation at low energies is due to the uncertainties present in the energy scales and acceptance curves, which broadens power of the analysis in this region as would be expected.

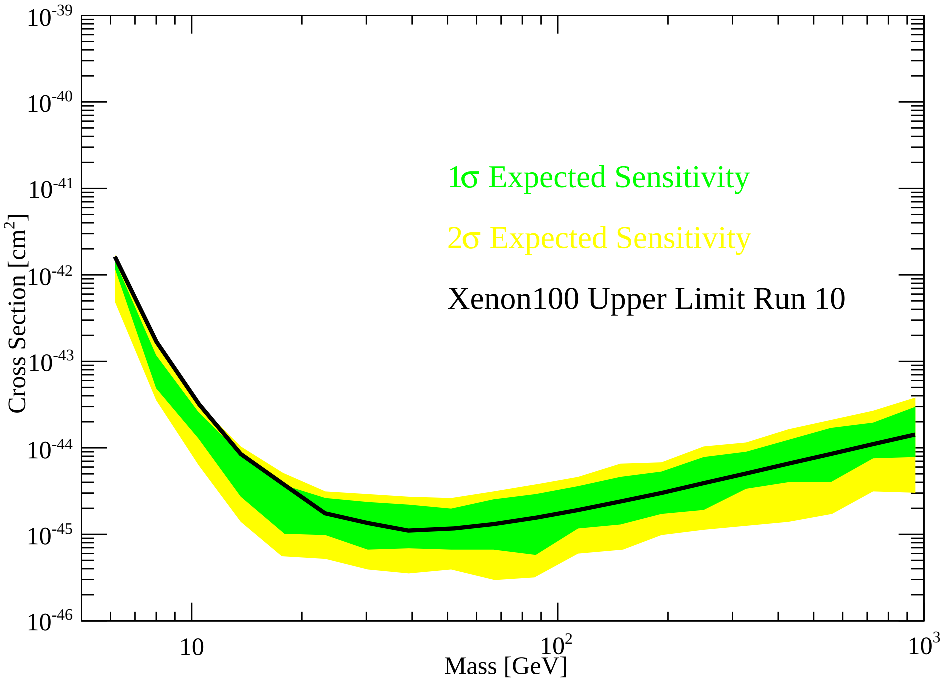

Figure 6.18: Expected sensitivity bands of the profile likelihood analysis on the spin-independent WIMP-nucleon cross section using the S2 as the energy estimator and parameter of interest. 2σ bands (68% and 95%) can be seen in *yellow* and *green*. The sensitivity of the XENON100 experiment is also shown in *black*.

6.4.3 Exclusion Limits

To calculate the exclusion limit for the real dataset, the same procedure is followed as for the expected sensitivity curves with the pseudoexperiment replaced by the dark matter data set from XENON100 run 10 (figure 6.19). The dataset consists of 27 events over the range 200-2000 S2 PE with none below the analysis threshold. There are two events near the lower bound of the region of interest which have been the subject of many efforts but have not resulted in a concrete conclusion about their origin.

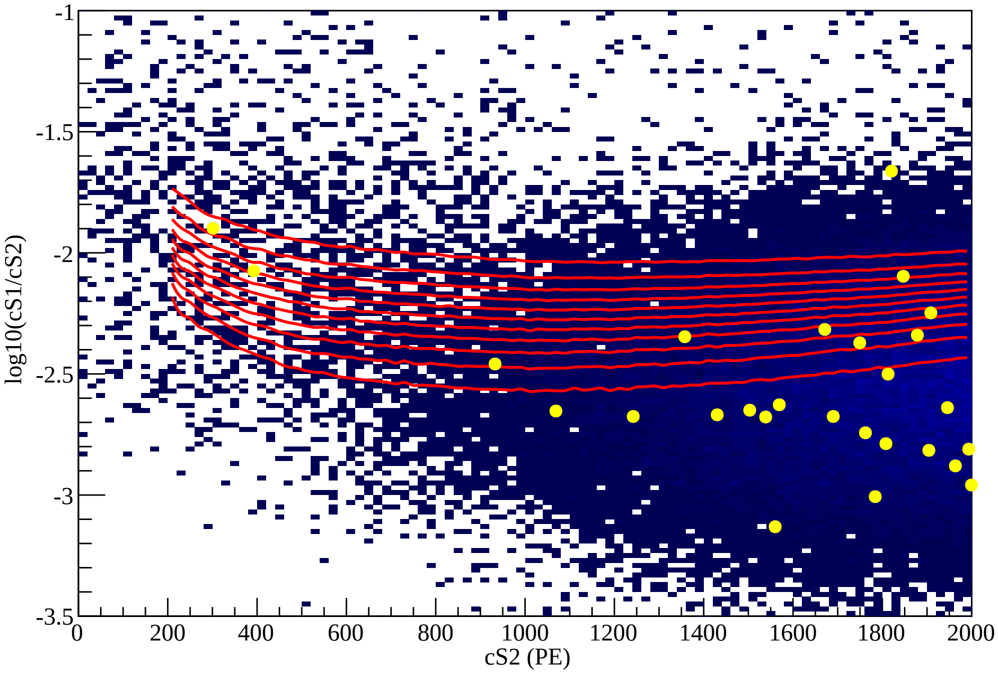

Figure 6.19: Distribution of the XENON100 dark matter data taking run from 2011-2012 in the region of interest from 200-2000 S2 PE in the Log_{10}(S1/S2) versus S2 phase space. The two events at low S2 are well separated from the bulk of the distribution, which around 600 PE. The background model distribution is shown in *blue* with the sharp increase in density above this point.

The 90% CL upper limit on the WIMP-nucleon spin-independent scattering cross section result for the XENON100 dataset is shown in figure 6.18 and appears near the median sensitivity at higher masses and moves towards the upper 2σ band at lower masses as a result of the two data events at low S2. The limit and expected sensitivity can also be seen in figure 6.20 in comparison to the published XENON100 limits. The improvement at low masses ranges from about 2 (at 30

GeV/c^2) to greater than 10 (at 6 GeV/c^2) due to a combination of the WIMP model, smearing from below 1 S1 PE, and use of the S2 energy estimator for the energy bounds. The upper limits presented here further constrain the low mass region and rule out the results of DAMA, CoGeNT, and CRESST-II as evidence for low mass WIMP particles.

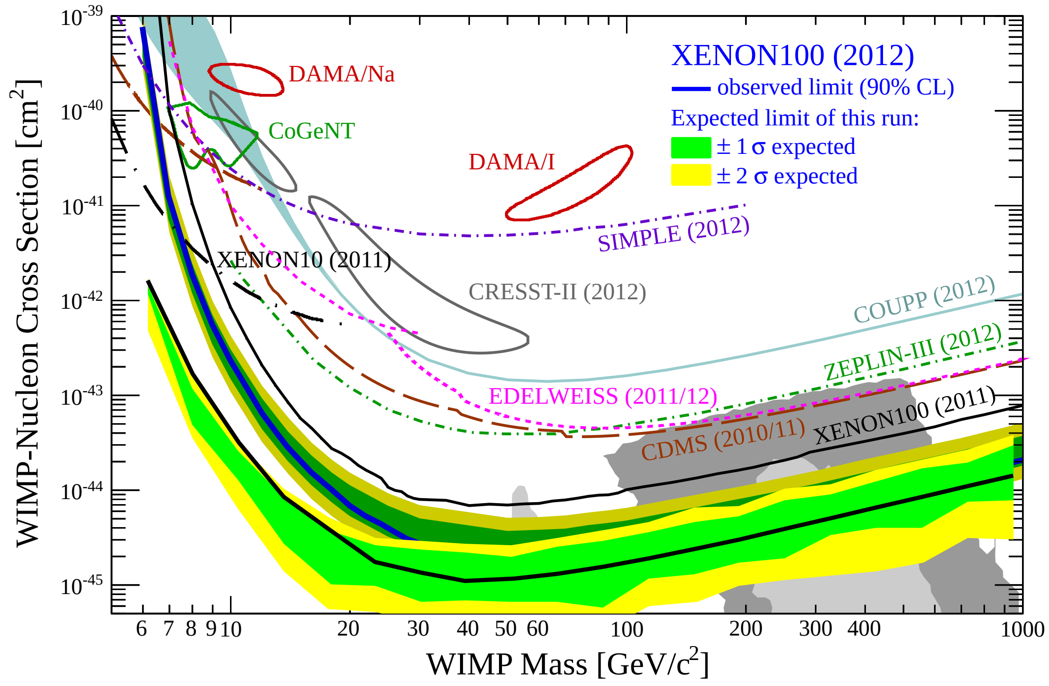

Figure 6.20: Expected sensitivity bands of the profile likelihood analysis on the spin-independent WIMP-nucleon cross section using the S2 as the energy estimator and parameter of interest (brighter colors and black line) with the Xenon100 [103] limits (shaded green and yellow and blue line) and theory regions from [66, 67, 68].

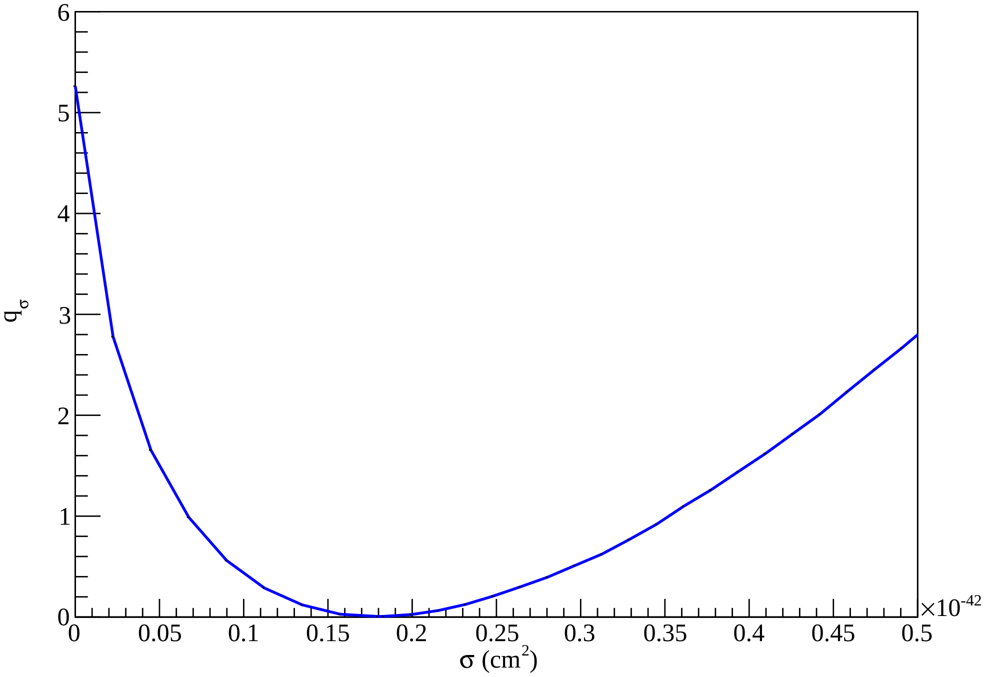

Figure 6.21: Likelihood curve of test statistic q_σ versus the cross section for a 7.5 GeV/c^2 WIMP mass. The discovery significance is given by the root of the test statistic for the background only ($\sigma_\chi = 0$) case. The maximum likelihood estimator for this mass is $\hat{\sigma_\chi} = 1.8 \times 10^{-43}$ cm^2 with a 95% confidence interval of $[1.74 \times 10^{-44}, 7.76 \times 10^{-43}]$ cm^2.

6.4.4 Discovery Potential

We can also consider the discovery potential for this dataset by following the guidelines of section 6.2.2.1. The test statistic necessary to find the significance is given by $\sqrt{q_0}$ where

$$q_0 = -2\ln\frac{\mathcal{L}(0, \hat{\hat{\boldsymbol{\theta}}})}{\mathcal{L}(\hat{\mu}, \hat{\boldsymbol{\theta}})} \tag{6.27}$$

which follows from equation 6.13. For each mass, the likelihood curve versus the cross section is obtained (example in figure 6.21) where q_0 is given by the intercept with $\sigma_\chi = 0$. The highest significance for the masses tested was at 7.5 GeV/c^2 of 2.3σ. An interval for this mass can be found for a confidence level of 95% to be $[1.74 \times 10^{-44}, 7.76 \times 10^{-43}]$ cm^2 with the maximum likelihood estimator $\hat{\sigma_\chi} = 1.8 \times 10^{-43}$ cm^2. The interval is not symmetric due to the low number of data events ($N = 27$) in the region of interest, but will become parabolic for large N due to the central limit theorem. We can also plot the 68% and 95% confidence regions in two dimensions, mass and cross section, using the χ^2 distribution with two degrees of freedom instead. A WIMP significance region can be seen in figure 6.22.

This result is not sufficient to constitute a discovery but shows possible hints of an excess unexplainable by the existing background model and supported by the WIMP Monte Carlo signal model.

In the future in conjunction with new measurements of the ionization yield, the advantages of this analysis using the new phase space with the S2 as the primary variable of interest will be evident once a non-negligible population of signal events is found due to its inherent spectral energy resolution and ability to discriminate between signal and background based on the S2 of an event. Instead of plotting the S2 in photoelectrons, we can instead look at the energy from the channel as shown in figure 6.23, which more effectively communicates the raw results to outside communities.

In this phase space, with the discrimination parameter changed to $\log_{10}(E1/E2)$, the mean of the signal distribution is inherently along $\log_{10}(E1/E2) = 0$ (section 4.3) while not quite evident for the 7.5 GeV/c^2 case due to acceptance cuts, can be demonstrated for a 50 GeV/c^2 WIMP signal demonstrated in figure 6.24.

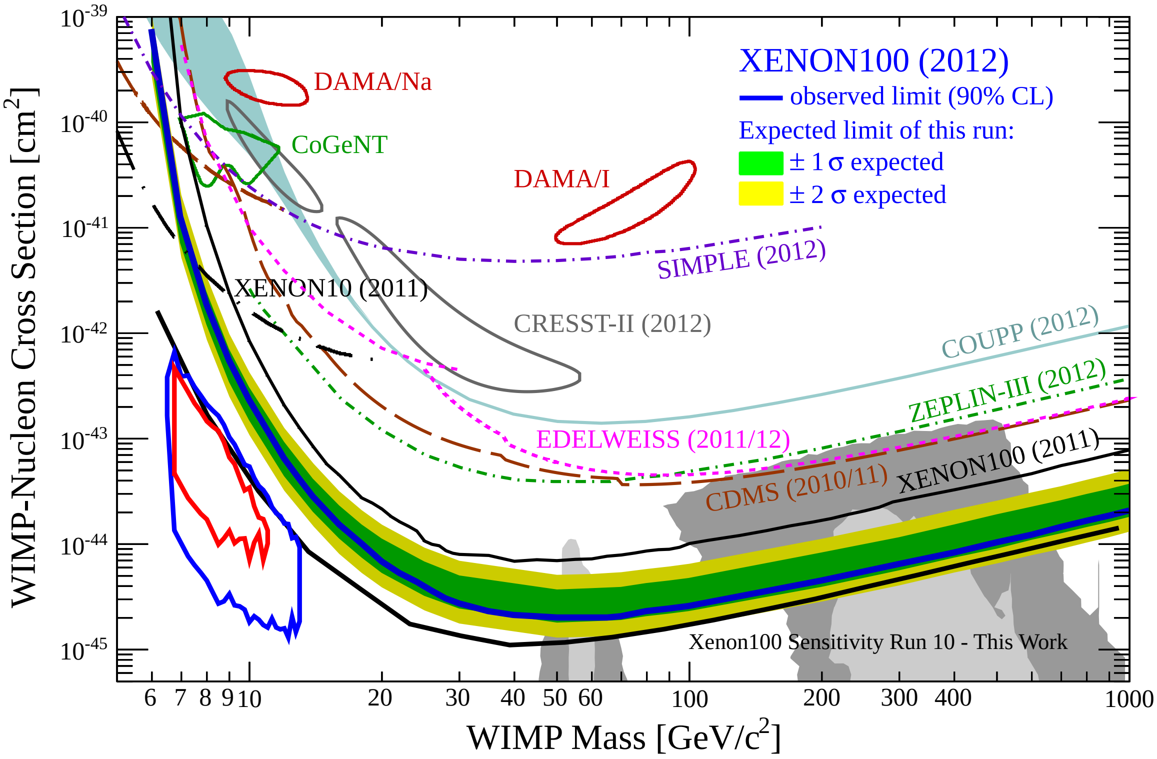

Figure 6.22: Spin independent WIMP-nucleon cross section versus WIMP mass phase space with 68% and 95% confidence regions as determined from the likelihood test statistic for a χ^2 distribution with two degrees of freedom.

This allows the signal band to be flattened without the aid of artificially transforming the data as is typically done in the Xenon100 analysis.

The analysis presented here shows the advantages of using the S2 signal, which gives better energy determination and resolution, and the corresponding increase in sensitivity. We have seen the possibilities for discovery using this method and its importance for the next generation of detectors which will hopefully have more impressive hints of weakly interacting particles.

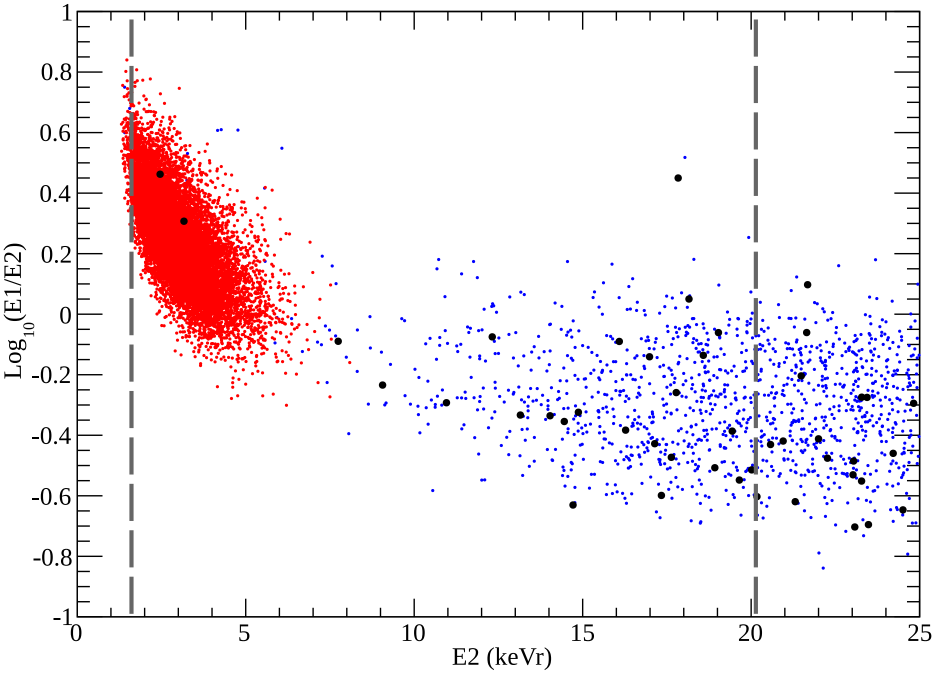

Figure 6.23: Distributions of the background (*blue*), dark matter data (*black*) and a simulated 7.5 GeV/c^2 WIMP (*red*) in the $\log_{10}(E1/E2)$ versus E2 phase space. The two events from dark matter data at low energies fall within the expected distribution of the Monte Carlo WIMP generated distribution.

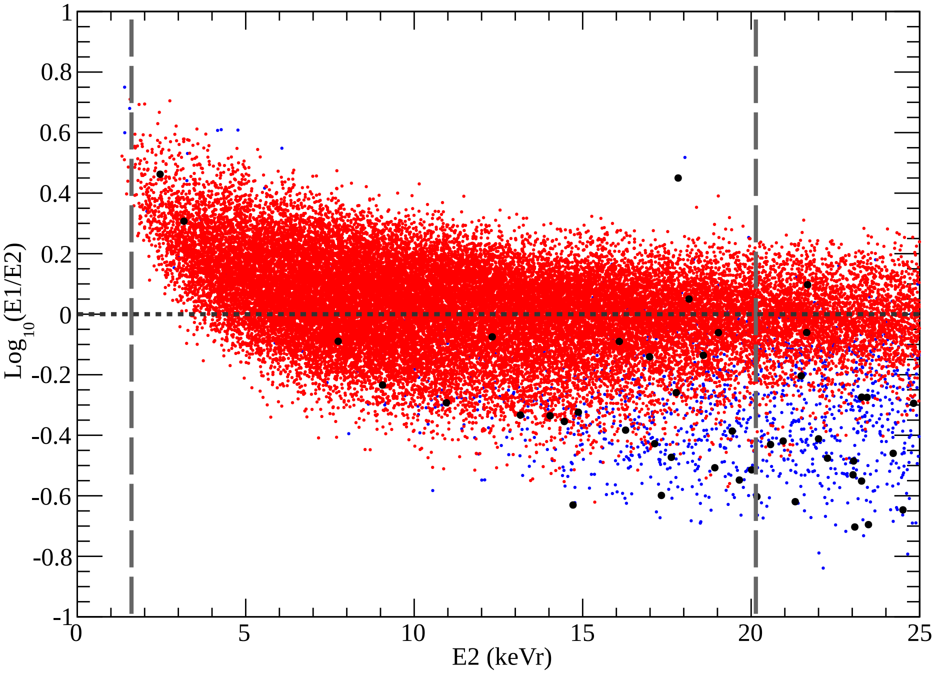

Figure 6.24: Distributions of the background (*blue*), dark matter data (*black*) and a simulated 50 GeV/c^2 WIMP (*red*). The $\log_{10}(E1/E2) = 0$ line follows the WIMP distribution except at low energies where threshold effects begin to cut events.

CHAPTER 7

Conclusion

The exact nature of the dark matter of the universe is still unknown. The most recent results from the XENON100 detector from 2012 show no hints of a WIMP detection and are beginning to rule out some of the favored supersymmetric phase space. Other detectors (CoGeNT, DAMA, and CRESSTII) demonstrate signal excesses at low WIMP masses with relatively large cross sections around 10^{-41} cm^2 motivating the necessity for an improved low energy analysis for liquid xenon detectors.

An analysis method, which takes advantage of the improved energy resolution and energy detemination near threshold of the ionization channel, is developed and shown here using the XENON100 data as an example. Indirect extraction of the ionization yield and relative scintillation efficiency using a comparison between Monte Carlo and calibration nuclear recoils give a better WIMP model for low masses while a profile likelihood statistical analysis improves the existing XENON100 limits by over a factor of 10 for WIMP masses below 10 GeV/c^2 and provides a 2.3σ significance for a WIMP discovery at 7.5 GeV/c^2. This significance can be better understood in the future through more detector exposure, improved measurements of the energy scales and a simulation to model the non-gaussianities of the background.

As part of the XENON100 collaboration, I have taken several shifts at the Gran Sasso laboratory in Italy to maintain proper operation of the detector and was involved with the core analysis team. My main contributions to the final XENON100 analysis was in the expected background for the signal region as well as for the entire energy range.

The improvements to this analysis as shown in Chapter 4 were developed within the UCLA group. I extended this analysis to XENON100 data using the simulation and energy scales from Chapter 5 and finally in a profile likelihood analysis in Chapter 6. For future liquid xenon detectors, this analysis provides the ability to more effectively measure the spectrum of candidate events in the event of signal with the inclusion of underlying systematic errors.

APPENDIX A

Wilk's Theorem

Following [130], suppose we have a likelihood function $\mathcal{L}(\boldsymbol{x}|\boldsymbol{\Theta})$ which consists of a product of probability density functions $f(\boldsymbol{\Theta}|\boldsymbol{x})$ of observable data, $\boldsymbol{x} = \{x^1, x^2, ...x^r\}$, and unknown parameters $\boldsymbol{\Theta} = \{\theta_1, ..\theta k\}$. The set of all possible parameter points of $\boldsymbol{\Theta}$ is denoted by Ω of the k-dimensional space. It is also possible to define subsets of Ω for only a given set (r-dimensional) of the $\boldsymbol{\Theta}$ parameters as Ω_r.

Let us first consider the case of a single dimension. The likelihood ($\mathcal{L}(\boldsymbol{x}|\theta)$) can be Taylor expanded

$$\frac{\partial \mathrm{ln}\mathcal{L}(\boldsymbol{x}|\theta)}{\partial \theta} = -E\left[\frac{\partial^2 \mathrm{ln}\mathcal{L}(\boldsymbol{x}|\theta)}{\partial \theta^2}\right](\hat{\theta} - \theta) + \mathcal{O}\left(\frac{1}{\sqrt{N}}\right) \tag{A.1}$$

resulting in Wald's approximation after ignoring terms of $\mathcal{O}(1/\sqrt{N})$, where N is the data sample size, $E[X]$ denotes the expectation value over the likelihood function and $\hat{\theta}$ is the maximum likelihood estimator of θ. Then the likelihood function can be written as

$$\mathcal{L}(\boldsymbol{x}|\theta) \propto \exp\left(-\frac{1}{2}E\left[\frac{\partial^2 \mathrm{ln}\mathcal{L}(\boldsymbol{x}|\theta)}{\partial \theta^2}\right](\hat{\theta} - \theta)^2\right) \tag{A.2}$$

Here, we take $\hat{\theta}$ to be normally distributed with mean given by a strength parameter θ' (not necessarily equal to θ) and variance $E\left[\frac{\partial^2 \mathrm{ln}\mathcal{L}(\boldsymbol{x}|\theta)}{\partial \theta^2}\right]$.

In multiple dimensions, this can easily be extended such that $\mathcal{L}(\boldsymbol{x}|\boldsymbol{\theta}) = \mathcal{L}(\boldsymbol{x}|\boldsymbol{\theta_r}, \boldsymbol{\theta_s})$, where we can think of θ_r as the parameters of interest and θ_s as the nuisance parameters. The likelihood can be written as

$$\mathcal{L}(\boldsymbol{x}|\boldsymbol{\theta}) \propto \exp\left[-\frac{1}{2}\left(\hat{\boldsymbol{\theta}} - \boldsymbol{\theta}\right)^{\mathrm{T}} \boldsymbol{I} \left(\hat{\boldsymbol{\theta}} - \boldsymbol{\theta}\right)\right] \tag{A.3}$$

where $\boldsymbol{I}$ is the inverse of the covariance matrix or the information matrix from information theory, which can also be written as

$$\boldsymbol{I} = \begin{bmatrix} \boldsymbol{I}_r & \boldsymbol{I}_{rs} \\ \boldsymbol{I}_{rs}^{\mathrm{T}} & \boldsymbol{I}_s \end{bmatrix} \tag{A.4}$$

for two subspaces of parameters denoted by r and s. The likelihood function follows as

$$\begin{aligned} \mathcal{L}(\boldsymbol{x}|\boldsymbol{\theta}_r, \boldsymbol{\theta}_s) \propto \exp\Bigg[&-\frac{1}{2}\left(\hat{\boldsymbol{\theta}}_r - \boldsymbol{\theta}_r\right)^{\mathrm{T}} \boldsymbol{I}_r \left(\hat{\boldsymbol{\theta}}_r - \boldsymbol{\theta}_r\right) \\ &- \frac{1}{2}\left(\hat{\boldsymbol{\theta}}_r - \boldsymbol{\theta}_r\right)^{\mathrm{T}} \boldsymbol{I}_{rs} \left(\hat{\boldsymbol{\theta}}_s - \boldsymbol{\theta}_s\right) \\ &- \frac{1}{2}\left(\hat{\boldsymbol{\theta}}_s - \boldsymbol{\theta}_s\right)^{\mathrm{T}} \boldsymbol{I}_s \left(\hat{\boldsymbol{\theta}}_s - \boldsymbol{\theta}_s\right)\Bigg] \end{aligned} \tag{A.5}$$

From the literature, the asymptotic distribution of $\hat{\boldsymbol{\theta}} = (\hat{\boldsymbol{\theta}}_r, \hat{\boldsymbol{\theta}}_s)$ is $r+s$ dimensionally normal with a covariance matrix given by $\boldsymbol{I}^{-1}$ such that the log-likelihood function tends asymptotically to the probability density function of $\hat{\boldsymbol{\theta}}$.

We now consider the likelihood ratio

$$\begin{aligned} \lambda &= \frac{\max_{\boldsymbol{\theta}_s} \mathcal{L}(\boldsymbol{x}|\boldsymbol{\theta}_{r0}, \boldsymbol{\theta}_s)}{\max_{\boldsymbol{\theta}_r, \boldsymbol{\theta}_s} \mathcal{L}(\boldsymbol{x}|\boldsymbol{\theta}_r, \boldsymbol{\theta}_s)} \\ &= \frac{\mathcal{L}(\boldsymbol{x}|\boldsymbol{\theta}_{r0}, \boldsymbol{\theta}''_s)}{\mathcal{L}(\boldsymbol{x}|\boldsymbol{\theta}'_r, \boldsymbol{\theta}'_s)} \end{aligned} \tag{A.6}$$

where the denominator is maximized over the full parameter space and the numerator is maximized over the $\boldsymbol{\theta}_s$ subspace with $\boldsymbol{\theta}_{r0}$ the unknown true value of the model parameter held fixed. When the likelihood is maximized we have, $\boldsymbol{\theta}'_r = \hat{\boldsymbol{\theta}}_r$ and $\boldsymbol{\theta}'_s = \hat{\boldsymbol{\theta}}_s$ such that $\mathcal{L}(\boldsymbol{x}|\boldsymbol{\theta}'_r, \boldsymbol{\theta}'_s) \propto 1$ asymptotically.

For the numerator of equation A.6, we see that when $\mathcal{L}(\boldsymbol{x}|\boldsymbol{\theta}_r, \boldsymbol{\theta}_s)$ is maximized only over the subspace containing $\boldsymbol{\theta}_s$ with a fixed $\boldsymbol{\theta}_{r0}$, then $\boldsymbol{\theta}''_s = \boldsymbol{\theta}_s$ and the likelihood becomes

$$\mathcal{L}(\boldsymbol{x}|\boldsymbol{\theta}_{r0}, \boldsymbol{\theta}''_s) \propto \exp\left[-\frac{1}{2}\left(\hat{\boldsymbol{\theta}}_r - \boldsymbol{\theta}_{r0}\right)^{\mathrm{T}} \boldsymbol{I}_r \left(\hat{\boldsymbol{\theta}}_r - \boldsymbol{\theta}_{r0}\right)\right] \tag{A.7}$$

which effectively leads to a profile likelihood test statistic of

$$\lambda = \exp\left[-\frac{1}{2}\left(\hat{\boldsymbol{\theta}}_r - \boldsymbol{\theta}_{r0}\right)^{\mathrm{T}} \boldsymbol{I}_r \left(\hat{\boldsymbol{\theta}}_r - \boldsymbol{\theta}_{r0}\right)\right] \tag{A.8}$$

such that the distribution of

$$-2\ln\lambda = \left(\hat{\boldsymbol{\theta}}_r - \boldsymbol{\theta}_{r0}\right)^{\mathrm{T}} \boldsymbol{I}_r \left(\hat{\boldsymbol{\theta}}_r - \boldsymbol{\theta}_{r0}\right) \to \chi^2_r \tag{A.9}$$

asymptotes to a χ^2 distribution with r degrees of freedom by covariance forms in standard multivariate normal random vectors. The distribution is a central $\chi^2(r)$ if data follows the underlying hypothesis H_0 and is a non-central $\chi^2(r)$ with non-centrality parameter

$$k_1 = \left(\boldsymbol{\theta}_r - \boldsymbol{\theta}_{r0}\right)^{\mathrm{T}} \boldsymbol{I}_r \left(\boldsymbol{\theta}_r - \boldsymbol{\theta}_{r0}\right) \tag{A.10}$$

for a differing underlying model, as follows from the asymptotic properties of $\hat{\boldsymbol{\theta}}_r$.

REFERENCES

[1] P. Peebles and B. Ratra, “The Cosmological constant and dark energy,” *Rev.Mod.Phys.*, vol. 75, pp. 559–606, 2003.

[2] D. Spergel *et al.*, “Wilkinson Microwave Anisotropy Probe (WMAP) three year results: implications for cosmology,” *Astrophys.J.Suppl.*, vol. 170, p. 377, 2007.

[3] P. Ade *et al.*, “Planck 2013 results. XVI. Cosmological parameters,” 2013.

[4] D. Spergel *et al.*, “First year Wilkinson Microwave Anisotropy Probe (WMAP) observations: Determination of cosmological parameters,” *Astrophys.J.Suppl.*, vol. 148, pp. 175–194, 2003.

[5] A. Friedman, “Über die krümmung des raumes,” *Zeitschrift für Physik*, vol. 10, pp. 377–386, 1922.

[6] L. Bergstrom, “Nonbaryonic dark matter: Observational evidence and detection methods,” *Rept.Prog.Phys.*, vol. 63, p. 793, 2000.

[7] J. H. Oort, “The force exerted by the stellar system in the direction perpendicular to the galactic plane and some related problems,” *Bulletin of the Astronomical Institutes of the Netherlands*, vol. 6, p. 249, Aug. 1932.

[8] V. Rubin, N. Thonnard, and J. Ford, W.K., “Rotational properties of 21 SC galaxies with a large range of luminosities and radii, from NGC 4605 /R = 4kpc/ to UGC 2885 /R = 122 kpc/,” *Astrophys.J.*, vol. 238, p. 471, 1980.

[9] T. van Albada, J. N. Bahcall, K. Begeman, and R. Sancisi, “The Distribution of Dark Matter in the Spiral Galaxy NGC-3198,” *Astrophys.J.*, vol. 295, pp. 305–313, 1985.

[10] K. Begeman, A. Broeils, and R. Sanders, “Extended rotation curves of spiral galaxies: Dark haloes and modified dynamics,” *Mon.Not.Roy.Astron.Soc.*, vol. 249, p. 523, 1991.

[11] F. Zwicky, “Spectral displacement of extra galactic nebulae,” *Helv.Phys.Acta*, vol. 6, pp. 110–127, 1933.

[12] F. Zwicky, “On the Masses of Nebulae and of Clusters of Nebulae,” *Astrophys.J.*, vol. 86, pp. 217–246, 1937.

[13] J. F. Navarro, C. S. Frenk, and S. D. White, “A Universal density profile from hierarchical clustering,” *Astrophys.J.*, vol. 490, pp. 493–508, 1997.

[14] J. Tyson, R. Wenk, and F. Valdes, “Detection of systematic gravitational lens galaxy image alignments - Mapping dark matter in galaxy clusters,” *Astrophys.J.*, vol. 349, pp. L1–L4, 1990.

[15] P. Schneider, J. Ehlers, and E. Falco, *Gravitational Lenses.* Astronomy and Astrophysics Library, Springer, 1999.

[16] D. Clowe, M. Bradac, A. H. Gonzalez, M. Markevitch, S. W. Randall, *et al.*, “A direct empirical proof of the existence of dark matter,” *Astrophys.J.*, vol. 648, pp. L109–L113, 2006.

[17] D. Baade *et al.*, “The Wide Field Imager at the 2.2-m MPG/ESO telescope: first views with a 67-million-facette eye.,” *The Messenger*, vol. 95, pp. 15–16, Mar. 1999.

[18] A. Dressler, B. Bigelow, T. Hare, B. Sutin, I. Thompson, G. Burley, H. Epps, J. Oemler, Augustus, A. Bagish, C. Birk, K. Clardy, S. Gunnels, D. Kelson, S. Shectman, and D. Osip, “Imacs: The inamori-magellan areal camera and spectrograph on magellan-baade,” *Publications of the Astronomical Society of the Pacific*, vol. 123, no. 901, pp. pp. 288–332, 2011.

[19] A. Vikhlinin, A. Kravtsov, W. Forman, C. Jones, M. Markevitch, *et al.*, “Chandra sample of nearby relaxed galaxy clusters: Mass, gas fraction, and mass-temperature relation,” *Astrophys.J.*, vol. 640, pp. 691–709, 2006.

[20] R. A. Alpher, J. W. Follin, and R. C. Herman, “Physical Conditions in the Initial Stages of the Expanding Universe,” *Phys.Rev.*, vol. 92, pp. 1347–1361, 1953.

[21] A. A. Penzias and R. W. Wilson, “A Measurement of excess antenna temperature at 4080-Mc/s,” *Astrophys.J.*, vol. 142, pp. 419–421, 1965.

[22] G. F. Smoot, C. Bennett, A. Kogut, E. Wright, J. Aymon, *et al.*, “Structure in the COBE differential microwave radiometer first year maps,” *Astrophys.J.*, vol. 396, pp. L1–L5, 1992.

[23] Bertout, C. and Forveille, T., “Pre-launch status of the planck mission,” *A&A*, vol. 520, p. E1, 2010.

[24] A. Miller, R. Caldwell, M. Devlin, W. Dorwart, T. Herbig, *et al.*, “A measurement of the angular power spectrum of the cmb from l = 100 to 400,” *Astrophys.J.*, vol. 524, pp. L1–L4, 1999.

[25] P. de Bernardis *et al.*, “A flat universe from high resolution maps of the cosmic microwave background radiation,” *Nature*, vol. 404, pp. 955–959, 2000.

[26] C. Bennett *et al.*, “The Microwave Anisotropy Probe (MAP) mission,” *Astrophys.J.*, vol. 583, pp. 1–23, 2003.

[27] D. Eisenstein, “Dark energy and cosmic sound,” *New Astronomy Reviews*, vol. 49, no. 7-9, pp. 360 – 365, 2005.

[28] E. Komatsu *et al.*, “Seven-Year Wilkinson Microwave Anisotropy Probe (WMAP) Observations: Cosmological Interpretation,” *Astrophys.J.Suppl.*, vol. 192, p. 18, 2011.

[29] G. Hinshaw, D. Larson, E. Komatsu, D. Spergel, C. Bennett, *et al.*, “Nine-Year Wilkinson Microwave Anisotropy Probe (WMAP) Observations: Cosmological Parameter Results,” 2012.

[30] M. Milgrom, “Solutions for the modified Newtonian dynamics field equation,” *Astrophys.J.*, vol. 302, pp. 617–625, 1986.

[31] R. H. Sanders and S. S. McGaugh, “Modified Newtonian dynamics as an alternative to dark matter,” *Ann.Rev.Astron.Astrophys.*, vol. 40, pp. 263–317, 2002.

[32] G. W. Angus, H. Shan, H. Zhao, and B. Famaey, “On the Law of Gravity, the Mass of Neutrinos and the Proof of Dark Matter,” *Astrophys.J.*, vol. 654, pp. L13–L16, 2007.

[33] K. Griest, “Cross-Sections, Relic Abundance and Detection Rates for Neutralino Dark Matter,” *Phys.Rev.*, vol. D38, p. 2357, 1988.

[34] R. Peccei and H. R. Quinn, “CP Conservation in the Presence of Instantons,” *Phys.Rev.Lett.*, vol. 38, pp. 1440–1443, 1977.

[35] M. S. Turner, “Cosmic and Local Mass Density of Invisible Axions,” *Phys.Rev.*, vol. D33, pp. 889–896, 1986.

[36] S. Asztalos *et al.*, “A SQUID-based microwave cavity search for dark-matter axions,” *Phys.Rev.Lett.*, vol. 104, p. 041301, 2010.

[37] J.-L. Gervais and B. Sakita, “Field theory interpretation of supergauges in dual models,” *Nucl.Phys.*, vol. B34, pp. 632–639, 1971.

[38] Y. Golfand and E. Likhtman, "Extension of the Algebra of Poincare Group Generators and Violation of p Invariance," *JETP Lett.*, vol. 13, pp. 323–326, 1971.

[39] E. Kolb and M. Turner, *The Early Universe.* Frontiers in Physics Series, Perseus Books, 1990.

[40] M. Visser, "An Exotic Class of Kaluza-Klein Models," *Phys.Lett.*, vol. B159, p. 22, 1985.

[41] G. Servant and T. M. Tait, "Is the lightest Kaluza-Klein particle a viable dark matter candidate?," *Nucl.Phys.*, vol. B650, pp. 391–419, 2003.

[42] J. N. Bahcall, M. Schmidt, and R. M. Soneira, "The galactic spheroid," *Astrophys.J.*, vol. 265, pp. 730–747, 1983.

[43] J. Caldwell and J. Ostriker, "The Mass distribution within our Galaxy: A Three component model," *Astrophys.J.*, vol. 251, pp. 61–87, 1981.

[44] G. Jungman, M. Kamionkowski, and K. Griest, "Supersymmetric dark matter," *Phys.Rept.*, vol. 267, pp. 195–373, 1996.

[45] J. Lewin and P. Smith, "Review of mathematics, numerical factors, and corrections for dark matter experiments based on elastic nuclear recoil," *Astropart.Phys.*, vol. 6, pp. 87–112, 1996.

[46] R. Woods and D. Saxon, "Diffuse surface optical model for nucleon-nuclei scattering," *Physical Review*, vol. 95, pp. 577–578, 1954.

[47] E. Aprile, K. Giboni, P. Majewski, K. Ni, M. Yamashita, *et al.*, "Scintillation response of liquid xenon to low energy nuclear recoils," *Phys.Rev.*, vol. D72, p. 072006, 2005.

[48] A. Bolozdynya, V. Egorov, A. Kuchenkov, G. Safronov, G. Smirnov, *et al.*, "A high pressure xenon selftriggered scintillation drift chamber with 3-D sensitivity in the range of 20-keV - 140-keV deposited energy," *Nucl.Instrum.Meth.*, vol. A385, pp. 225–238, 1997.

[49] S. Kubota, M. Hishida, and J. Raun, "Evidence for a triplet state of the self-trapped exciton states in liquid argon, krypton and xenon," *Journal of Physics C: Solid State Physics*, vol. 11, no. 12, p. 2645, 1978.

[50] G. Gerbier, J. Mallet, L. Mosca, C. Tao, B. Chambon, *et al.*, "Pulse shape discrimination with NaI(Tl) and results from a WIMP search at the Laboratoire Souterrain de Modane," *Astropart.Phys.*, vol. 11, pp. 287–302, 1999.

[51] W. Lippincott, K. Coakley, D. Gastler, A. Hime, E. Kearns, *et al.*, "Scintillation time dependence and pulse shape discrimination in liquid argon," *Phys.Rev.*, vol. C78, p. 035801, 2008.

[52] E. Aprile *et al.*, "The XENON100 Dark Matter Experiment," *Astropart.Phys.*, vol. 35, pp. 573–590, 2012.

[53] G. Alner, H. Araujo, A. Bewick, C. Bungau, B. Camanzi, *et al.*, "First limits on WIMP nuclear recoil signals in ZEPLIN-II: A two phase xenon detector for dark matter detection," *Astropart.Phys.*, vol. 28, pp. 287–302, 2007.

[54] D. Y. Akimov, H. Araujo, E. Barnes, V. Belov, A. Bewick, *et al.*, "WIMP-nucleon cross-section results from the second science run of ZEPLIN-III," *Phys.Lett.*, vol. B709, pp. 14–20, 2012.

[55] D. McKinsey, D. Akerib, S. Bedikian, A. Bernstein, A. Bolozdynya, *et al.*, "The LUX dark matter search," *J.Phys.Conf.Ser.*, vol. 203, p. 012026, 2010.

[56] A. Wright, "The DarkSide Program at LNGS," 2011.

[57] K. Abe, "The XMASS experiment," *J.Phys.Conf.Ser.*, vol. 120, p. 042022, 2008.

[58] V. Mandic *et al.*, "Study of the dead layer in germanium for the CDMS detectors," *Nucl.Instrum.Meth.*, vol. A520, pp. 171–174, 2004.

[59] Z. Ahmed *et al.*, "Dark Matter Search Results from the CDMS II Experiment," *Science*, vol. 327, pp. 1619–1621, 2010.

[60] E. Armengaud *et al.*, "Final results of the EDELWEISS-II WIMP search using a 4-kg array of cryogenic germanium detectors with interleaved electrodes," *Phys.Lett.*, vol. B702, pp. 329–335, 2011.

[61] G. Angloher, M. Bauer, I. Bavykina, A. Bento, C. Bucci, *et al.*, "Results from 730 kg days of the CRESST-II Dark Matter Search," *Eur.Phys.J.*, vol. C72, p. 1971, 2012.

[62] R. Bernabei *et al.*, "New results from DAMA/LIBRA," *Eur.Phys.J.*, vol. C67, pp. 39–49, 2010.

[63] C. Aalseth *et al.*, "Results from a Search for Light-Mass Dark Matter with a P-type Point Contact Germanium Detector," *Phys.Rev.Lett.*, vol. 106, p. 131301, 2011.

[64] D. Hooper, J. Collar, J. Hall, D. McKinsey, and C. Kelso, "A Consistent Dark Matter Interpretation For CoGeNT and DAMA/LIBRA," *Phys.Rev.*, vol. D82, p. 123509, 2010.

[65] S. Chang, J. Liu, A. Pierce, N. Weiner, and I. Yavin, "CoGeNT Interpretations," *JCAP*, vol. 1008, p. 018, 2010.

[66] C. Strege, G. Bertone, D. Cerdeno, M. Fornasa, R. Ruiz de Austri, *et al.*, "Updated global fits of the cMSSM including the latest LHC SUSY and Higgs searches and XENON100 data," *JCAP*, vol. 1203, p. 030, 2012.

[67] O. Buchmueller, R. Cavanaugh, A. De Roeck, M. Dolan, J. Ellis, *et al.*, "Higgs and Supersymmetry," *Eur.Phys.J.*, vol. C72, p. 2020, 2012.

[68] A. Fowlie, M. Kazana, K. Kowalska, S. Munir, L. Roszkowski, *et al.*, "The CMSSM Favoring New Territories: The Impact of New LHC Limits and a 125 GeV Higgs," *Phys.Rev.*, vol. D86, p. 075010, 2012.

[69] E. Aprile *et al.*, "Dark Matter Results from 100 Live Days of XENON100 Data," *Phys.Rev.Lett.*, vol. 107, p. 131302, 2011.

[70] R. Hartman *et al.*, "The Third EGRET catalog of high-energy gamma-ray sources," *Astrophys.J.Suppl.*, vol. 123, p. 79, 1999.

[71] W. Atwood *et al.*, "The Large Area Telescope on the Fermi Gamma-ray Space Telescope Mission," *Astrophys.J.*, vol. 697, pp. 1071–1102, 2009.

[72] F. Barao, "AMS: Alpha Magnetic Spectrometer on the International Space Station," *Nucl.Instrum.Meth.*, vol. A535, pp. 134–138, 2004.

[73] V. Bonvicini *et al.*, "The PAMELA experiment in space," *Nucl.Instrum.Meth.*, vol. A461, pp. 262–268, 2001.

[74] O. Adriani *et al.*, "An anomalous positron abundance in cosmic rays with energies 1.5-100 GeV," *Nature*, vol. 458, pp. 607–609, 2009.

[75] Y. Bai, P. J. Fox, and R. Harnik, "The Tevatron at the Frontier of Dark Matter Direct Detection," *JHEP*, vol. 1012, p. 048, 2010.

[76] M. Beltran, D. Hooper, E. W. Kolb, Z. A. Krusberg, and T. M. Tait, "Maverick dark matter at colliders," *JHEP*, vol. 1009, p. 037, 2010.

[77] J. Goodman, M. Ibe, A. Rajaraman, W. Shepherd, T. M. Tait, *et al.*, "Constraints on Dark Matter from Colliders," *Phys.Rev.*, vol. D82, p. 116010, 2010.

[78] R. Platzman, "Total ionization in gases by high-energy particles: An appraisal of our understanding," *The International Journal of Applied Radiation and Isotopes*, vol. 10, no. 2–3, pp. 116 – 127, 1961.

[79] T. Takahashi, S. Konno, T. Hamada, M. Miyajima, S. Kubota, A. Nakamoto, A. Hitachi, E. Shibamura, and T. Doke, "Average energy expended per ion pair in liquid xenon," *Phys. Rev. A*, vol. 12, pp. 1771–1775, Nov 1975.

[80] L. Onsager, "Initial Recombination of Ions," *Phys.Rev.*, vol. 54, pp. 554–557, 1938.

[81] J. Thomas and D. Imel, "Recombination of electron-ion pairs in liquid argon and liquid xenon," *Phys.Rev.*, vol. A36, pp. 614–616, 1987.

[82] A. Hitachi, T. Takahashi, N. Funayama, K. Masuda, J. Kikuchi, *et al.*, "Effect of ionization density on the time dependence of luminescence from liquid argon and xenon," *Phys.Rev.*, vol. B27, pp. 5279–5285, 1983.

[83] G. Seidel, R. Lanou, and W. Yao, "Rayleigh scattering in rare-gas liquids," *Nuclear Instruments and Methods in Physics Research Section A: Accelerators, Spectrometers, Detectors and Associated Equipment*, vol. 489, no. 1–3, pp. 189 – 194, 2002.

[84] A. Baldini, C. Bemporad, F. Cei, T. Doke, M. Grassi, *et al.*, "Absorption of scintillation light in a 100 l liquid xenon gamma ray detector and expected detector performance," *Nucl.Instrum.Meth.*, vol. A545, pp. 753–764, 2005.

[85] E. Aprile, R. Mukherjee, and M. Suzuki, "Performance of a liquid xenon ionization chamber irradiated with electrons and gamma-rays," *Nucl.Instrum.Meth.*, vol. A302, pp. 177–185, 1991.

[86] V. N. Lebedenko *et al.*, "Results from the first science run of the ZEPLIN-III Dark Matter Search Experiment," *Phys. Rev. D*, vol. 80, p. 050210, 2009.

[87] E. Aprile, C. Dahl, L. DeViveiros, R. Gaitskell, K. Giboni, *et al.*, "Simultaneous measurement of ionization and scintillation from nuclear recoils in liquid xenon as target for a dark matter experiment," *Phys.Rev.Lett.*, vol. 97, p. 081302, 2006.

[88] V. Chepel, V. Solovov, F. Neves, A. Pereira, P. Mendes, *et al.*, "Scintillation efficiency of liquid xenon for nuclear recoils with the energy down to 5-keV," *Astropart.Phys.*, vol. 26, pp. 58–63, 2006.

[89] E. Aprile, L. Baudis, B. Choi, K. Giboni, K. Lim, *et al.*, "New Measurement of the Relative Scintillation Efficiency of Xenon Nuclear Recoils Below 10 keV," *Phys.Rev.*, vol. C79, p. 045807, 2009.

[90] A. Manzur, A. Curioni, L. Kastens, D. McKinsey, K. Ni, *et al.*, "Scintillation efficiency and ionization yield of liquid xenon for mono-energetic nuclear recoils down to 4 keV," *Phys.Rev.*, vol. C81, p. 025808, 2010.

[91] G. Plante, E. Aprile, R. Budnik, B. Choi, K. Giboni, *et al.*, "New Measurement of the Scintillation Efficiency of Low-Energy Nuclear Recoils in Liquid Xenon," *Phys.Rev.*, vol. C84, p. 045805, 2011.

[92] M. Horn, V. Belov, D. Y. Akimov, H. Araujo, E. Barnes, *et al.*, "Nuclear recoil scintillation and ionisation yields in liquid xenon from ZEPLIN-III data," *Phys.Lett.*, vol. B705, pp. 471–476, 2011.

[93] J. Collar and D. McKinsey, "Comments on 'First Dark Matter Results from the XENON100 Experiment'," 2010.

[94] V. Solovov, V. Chepel, M. Lopes, and A. Hitachi, "Measurement of the refractive index and attenuation length of liquid xenon for its scintillation light," *Nucl.Instrum.Meth.*, vol. A516, pp. 462–474, 2004.

[95] L. Miller, S. Howe, and W. Spear, "Charge Transport in Solid and Liquid Ar, Kr, and Xe," *Phys.Rev.*, vol. 166, pp. 871–878, 1968.

[96] M. Yamashita, T. Doke, K. Kawasaki, J. Kikuchi, and S. Suzuki, "Scintillation response of liquid xe surrounded by ptfe reflector for gamma rays," *Nuclear Instruments and Methods in Physics Research Section A: Accelerators, Spectrometers, Detectors and Associated Equipment*, vol. 535, no. 3, pp. 692 – 698, 2004.

[97] M. Ambrosio *et al.*, "Vertical muon intensity measured with MACRO at the Gran Sasso Laboratory," *Phys.Rev.*, vol. D52, pp. 3793–3802, 1995.

[98] E. Aprile, K. Arisaka, F. Arneodo, A. Askin, L. Baudis, *et al.*, "Study of the electromagnetic background in the XENON100 experiment," *Phys.Rev.*, vol. D83, p. 082001, 2011.

[99] E. Aprile, K. Arisaka, F. Arneodo, A. Askin, L. Baudis, *et al.*, "Material screening and selection for XENON100," *Astropart.Phys.*, vol. 35, pp. 43–49, 2011.

[100] L. Baudis, A. Ferella, A. Askin, J. Angle, E. Aprile, *et al.*, "Gator: a low-background counting facility at the Gran Sasso Underground Laboratory," *JINST*, vol. 6, p. P08010, 2011.

[101] W. B. Wilson *et al.*, *SOURCES 4A : a code for calculating ([alpha],n), spontaneous fission, and delayed neutron sources and spectra.* Los Alamos National Laboratory Report LA-13639-MS, September 2002.

[102] E. Aprile, M. Alfonsi, K. Arisaka, F. Arneodo, C. Balan, *et al.*, "The distributed Slow Control System of the XENON100 Experiment," *JINST*, vol. 7, p. T12001, 2012.

[103] E. Aprile *et al.*, "Dark Matter Results from 225 Live Days of XENON100 Data," *Phys.Rev.Lett.*, vol. 109, p. 181301, 2012.

[104] V. Vapnik, *Estimation of Dependences Based on Empirical Data: Springer Series in Statistics (Springer Series in Statistics).* Secaucus, NJ, USA: Springer-Verlag New York, Inc., 1982.

[105] A. Zell *et al.*, *SNNS (Stuttgart Neural Network Simulator) - user manual Version 4.0.* 70565 Stuttgart, Fed. Rep. of Germany. SNNS User Manual Version 4.0.

[106] K. Arisaka, P. Beltrame, C. Ghag, K. Lung, and P. R. Scovell, "A New Analysis Method for WIMP searches with Dual-Phase Liquid Xe TPCs," *Astropart.Phys.*, vol. 37, pp. 1–88, 2012.

[107] J. F. Ziegler, U. Littmark, and J. P. Biersack, *The stopping and range of ions in solids / J.F. Ziegler, J.P. Biersack, U. Littmark.* Pergamon, New York :, 1985.

[108] S. Agostinelli *et al.*, "Geant4 - a simulation toolkit," *Nuclear Instruments and Methods in Physics Research Section A: Accelerators, Spectrometers, Detectors and Associated Equipment*, vol. 506, no. 3, pp. 250 – 303, 2003.

[109] B. N. L. National Nuclear Data Center, "Nudat (nuclear structure and decay data)," March 18, 2008 2008.

[110] ISO 8529-1, 2001, "Reference neutron radiations part 1: characteristics and methods of production," *International Organization for Standardization, 56. CH-1211, Geneva, Switzerland.*, p. 32, 2001.

[111] M. Matsumoto and T. Nishimura, "Mersenne twister: a 623-dimensionally equidistributed uniform pseudo-random number generator," *ACM Trans. Model. Comput. Simul.*, vol. 8, pp. 3–30, Jan. 1998.

[112] B. Edwards, H. Araujo, V. Chepel, D. Cline, T. Durkin, *et al.*, "Measurement of single electron emission in two-phase xenon," *Astropart.Phys.*, vol. 30, pp. 54–57, 2008.

[113] K. Levenberg, "A method for the solution of certain problems in least squares," *Quart. Applied Math.*, vol. 2, pp. 164–168, 1944.

[114] D. W. Marquardt, "An algorithm for least-squares estimation of nonlinear parameters," *Journal of the Society for Industrial and Applied Mathematics*, vol. 11, no. 2, pp. pp. 431–441, 1963.

[115] K. Madsen, H. Bruun, and O. Tingleff, "Methods for non-linear least squares problems," 1999.

[116] R. L. Plackett, "Karl Pearson and the Chi-Squared Test," *International Statistical Review / Revue Internationale de Statistique*, vol. 51, no. 1, pp. 59–72, 1983.

[117] H. Akima, "A new method of interpolation and smooth curve fitting based on local procedures," *J. ACM*, vol. 17, no. 4, pp. 589–602, 1970.

[118] P. Sorensen, A. Manzur, C. Dahl, J. Angle, E. Aprile, *et al.*, "The scintillation and ionization yield of liquid xenon for nuclear recoils," *Nucl.Instrum.Meth.*, vol. A601, pp. 339–346, 2009.

[119] E. Aprile *et al.*, "Analysis of the XENON100 Dark Matter Search Data," 2012.

[120] G. J. Feldman and R. D. Cousins, "Unified approach to the classical statistical analysis of small signals," *Physical Review D*, vol. 57, pp. 3873–3889, Apr. 1998.

[121] E. Aprile *et al.*, "Likelihood Approach to the First Dark Matter Results from XENON100," *Phys.Rev.*, vol. D84, p. 052003, 2011.

[122] J. Neyman and E. S. Pearson, "On the problem of the most efficient tests of statistical hypotheses," *Philosophical Transactions of the Royal Society of London Series A Containing Papers of a Mathematical or Physical Character*, vol. 231, no. 694-706, pp. 289–337, 1933.

[123] T. Junk, "Confidence level computation for combining searches with small statistics," *Nucl.Instrum.Meth.*, vol. A434, pp. 435–443, 1999.

[124] G. Cowan, K. Cranmer, E. Gross, and O. Vitells, "Asymptotic formulae for likelihood-based tests of new physics," *Eur.Phys.J.*, vol. C71, p. 1554, 2011.

[125] A. L. Read, "Presentation of search results: the cl s technique," *Journal of Physics G: Nuclear and Particle Physics*, vol. 28, no. 10, p. 2693, 2002.

[126] S. S. Wilks, "The Large-Sample Distribution of the Likelihood Ratio for Testing Composite Hypotheses," *The Annals of Mathematical Statistics*, vol. 9, no. 1, pp. 60–62, 1938.

[127] A. Wald, "Tests of Statistical Hypotheses Concerning Several Parameters When the Number of Observations is Large," *Transactions of the American Mathematical Society*, vol. 54, no. 3, pp. 426–482, 1943.

[128] M. C. Smith, G. Ruchti, A. Helmi, R. Wyse, J. Fulbright, *et al.*, "The RAVE Survey: Constraining the Local Galactic Escape Speed," *Mon.Not.Roy.Astron.Soc.*, vol. 379, pp. 755–772, 2007.

[129] F. James and M. Roos, "Minuit: A System for Function Minimization and Analysis of the Parameter Errors and Correlations," *Comput.Phys.Commun.*, vol. 10, pp. 343–367, 1975.

[130] W. Eadie and F. James, *Statistical Methods in Experimental Physics (2nd Edition).* World Scientific, 2006.